2020-01-01

SynThesis of Nanotemplated, Glucose-derived Adsorbents for the Removal of Organic and Inorganic Pollutants from Water

Luis Alfonso Barrera
University of Texas at El Paso

Recommended Citation

Barrera, Luis Alfonso, "SynThesis of Nanotemplated, Glucose-derived Adsorbents for the Removal of Organic and Inorganic Pollutants from Water" (2020). *Open Access Theses & Dissertations*. 3082.
https://scholarworks.utep.edu/open_etd/3082

SYNTHESIS OF NANOTEMPLATED, GLUCOSE-DERIVED ADSORBENTS FOR THE REMOVAL OF ORGANIC AND INORGANIC POLLUTANTS FROM WATER

LUIS ALFONSO BARRERA

Doctoral Program in Chemistry

APPROVED:

Juan C. Noveron, Ph.D., Chair

Jose L. Bañuelos, Ph.D.

Wen-Yee Lee, Ph.D.

James Salvador, Ph.D.

Stephen L. Crites, Jr., Ph.D.
Dean of the Graduate School

Dedication

To my friends and family, who have supported me through moments which seemed impossible to surmount.

SYNTHESIS OF NANOTEMPLATED, GLUCOSE-DERIVED ADSORBENTS FOR THE REMOVAL OF ORGANIC AND INORGANIC POLLUTANTS FROM WATER

by

LUIS ALFONSO BARRERA, B.S., M.S.

DISSERTATION

Presented to the Faculty of the Graduate School of
The University of Texas at El Paso
in Partial Fulfillment
of the Requirements
for the Degree of

DOCTOR OF PHILOSOPHY

Department of Chemistry and Biochemistry
THE UNIVERSITY OF TEXAS AT EL PASO
August 2020

Acknowledgements

First and foremost, I would like to express my deepest gratitude to Dr. Juan C. Noveron. The many hours of scientific discourse which happened regularly in the lab have made me a fundamentally more well-rounded scientist. Thank you for all the opportunities awarded to me, from internship, conference and presentation opportunities to the experience of mentoring a variety of undergraduate students and high school teachers. All of these experiences have helped me develop stronger leadership skills, and have molded me into the researcher I am today.

I would like to thank the members of this committee, Dr. James Salvador, Dr. Wen-Yee Lee and Dr. Jose L. Bañuelos for their advice and support throughout my research endeavors. I consider you three to be primary examples of what a great mentor should be, and I will strive to become a scientist of your same caliber.

For their continued support and funding throughout my studies I would like to thank UTEP Department of Chemistry and Biochemistry. This degree would not have been possible without it.

To all the people I have had the pleasure of working alongside in the lab, my deepest gratitude. Dr. Andrew Pardo, Dr. Noemi Dominguez, Dr. Tariqul Islam and Ariful Ahsan, the long hours in the lab were greatly shortened by your company. All of our conversations, from scientific to mundane, were of great value to me. A special acknowledgement to the long list of undergraduate students whom I have had the pleasure of working alongside, whether you were there a week, a year or longer, know that it was a pleasure working with all of you. A special thanks to Carolina for her immeasurable help during the inception of this body of work, and to Aileen for her help during its conclusion.

To my friends outside the lab, thank you for your continued support through all of these years. Bruce De La Paz, Arturo Medina, John Jaramillo, Dr. Alfredo Ornelas, Emmanuel Utreras, Yoshira Ayala, Dr. Luis Solis, Dr. Karla Parra and Daisy Tepezano, thank you for lending me your ears and shoulders through my PhD. Our many talks and outings were the fuel I needed to recharge my batteries and continue full-steam on my work.

And lastly, but most importantly, I'd like to most sincerely thank my beautiful family. To my father, Jose Luis Barrera, for being my biggest inspiration in life; to my mother, Laura Pereda, for showing me that perseverance and compassion can conquer everything; to my brother, Marco A. Barrera, for the long hours spent pondering the universe, from large to small; and to my sister, Elizabeth Barrera, for being a prime example that hard work and dedication really do pay off; Thank you.

Abstract

With an ever-present rise in population, along with an increase in industrial and manufacturing plants, contamination of potable water has become a global concern. While water treatment facilities exist which can help with the purification of water from bacterial and organic contaminants, these facilities are expensive to set in place and maintain. Therefore, in impoverished areas, point of use (POU) purification systems are often preferred, such as filters made from activated carbon. These filters are inexpensive and relatively easy to install and use. However, while activated carbons generally display excellent adsorption capabilities towards organic contaminants, their adsorption towards inorganic pollutants is limited. Moreover, most research towards their production generally utilizes large polymers, such as lignocellulosic material, along with metal salts for their activation. The use of smaller monomeric carbon sources has seldom been explored.

We proposed the use of a smaller carbon source, glucose, as well as the utilization of zinc oxide nanoparticles for the synthesis of these carbon adsorbents. By utilizing this method we developed four adsorbent materials, including a high surface area adsorbent (1228 m^2/g) which showed great adsorption capacities towards organic contaminants, as well as a photoactive adsorbent which demonstrated catalytic degradation capabilities towards methylene blue, ofloxacin and tetracycline. In addition, we expanded upon the adsorptive properties of these carbon-based materials by incorporating further functionalization, developing an adsorbent with magnetic properties which showed promise towards the adsorption of Pb(II), As(III) and As(V) (Q_e: 5.57, 7.86 and 4.48 mg/g, respectively), as well as an adsorbent functionalized with sulfur for the adsorption of inorganic contaminants (Ba (Q_e 8.65 mg/g) and As(III) (Q_e 2.66 mg/g)).

Table of Contents

List of Tables

List of Figures

List of Schemes

Chapter 1: Introduction

1.1 WATER CONTAMINATION

Water contamination is a rather broad term, as the identity and source of 'contaminants' spans a wide berth of pollutants and origins. In a very broad sense, water contaminants can be classified as either biological, organic, or inorganic in nature. Organic contaminants can be largely classified into more specific subcategories, such as pharmaceuticals/personal care products, pesticides, veterinary products, industrial compounds and byproducts, food additives, and many more smaller, more individualized subcategories such as nanomaterials and plasticizers.[1] The emergence of these organic contaminants into the environment is also varied, but can be broadly classified as emerging from wastewater effluents, septic tanks, hospital effluents, subsurface storage of industrial waste, and potentially through groundwater-surface water exchange. [2-6] While many sources of pollution can be pinpointed (point-source pollution), such as industrial effluents, resource extraction (mining, fracking), and landfill sites, other sources (such as runoff water from stormwaters, catchments and field drains) can span a broad geographical area, resulting in diffuse pollution.[7-9]

Much like with organic pollutants, inorganic pollution can be largely varied in nature. Broadly speaking, most inorganic contaminants can be classified under heavy metals, oxyanions and cations, halides, and radioactive materials.[10] Inorganic contaminants are persistent to degradation, and most biological systems are not equipped for their removal, making these contaminants especially potent.[11] For example, large concentrations of nitrate in drinking waters can result in an increased risk for methemoglobinemia and the formation of carcinogenic nitrosamines.[12] While fluoride in small concentrations can have beneficial health effects, large concentrations of fluoride and fluorine-containing compounds could potentially result in teeth decay, crippling, and skeletal fluorosis.[13] Perhaps the more commonly discussed and potentially more harmful inorganic contaminants consist of heavy metals, with the more commonly studied metals being arsenic, copper, chromium, lead, mercury, nickel, and zinc.[14,15] While there are natural sources for inorganic contamination onto an ecosystem, such as volcanic eruptions, natural erosion of soil, and the natural disintegration of rocks, man-made pollution has drastically increased the quantity and variety of heavy metal pollution onto the environment. Wastewater from a large variety of industrial processes (mining, fracking, plastics, smelters, dyes, alloys, etc.) are a common source of toxic heavy metal pollution, including arsenic, cadmium, chromium, copper, mercury, lead and zinc.[11]

Large concentrations of these heavy metals can have wide-ranging adverse effects on entire ecosystems, as they can spread through food chains and expedite circulation.[16] Due to our inability to remove many of these heavy metals from our bodies, large and/or frequent exposure to these toxic metals can have long-lasting deleterious effects, ranging from skin disease, kidney disease, stomach/liver problems, high blood pressure, and cancer development, amongst many others.

1.2 REMEDIATION PROCESSES

There have been a plethora of methods utilized for the decontamination of water, spanning a wide variety of scientific approaches. Water remediation from organic pollutants has seen the employment of methods such as physical adsorption,[17,18] chemical reduction/oxidation,[19,20] electrochemical degradation,[21] photocatalytic degradation,[22,23] and even biological methods[24] having been employed for the removal and/or degradation of these contaminants. Degradation processes and reduction/oxidation catalysis, either chemical or electrochemical, can be particularly appealing as they often result in the complete mineralization of organic contaminants. However, they require the use of added reagents or energy in order to catalytically remove contaminants from water, making them less ideal for use in places with fewer resources to spare. From these methods, adsorption is often the preferred method for remediation of water from organic pollutants due to its low cost and ease of use, with activated carbons seeing the most success in real world applications.

Removal of heavy metals from water poses a different problem, as these contaminants cannot be degraded to their mineralization products by catalytic degradation, as is the case with many organic contaminants. The more commonly employed methods for water remediation in the case of heavy metals include membrane filtration,[25] electrocoagulation,[26,27] microbial remediation,[28] and a plethora of modified adsorbents[29,30] and activated carbons.[31,32] While membrane filtration, electrocoagulation, microbial remediation and other chemical methods for the removal of heavy metals can be highly effective, their preparation and applied use can often be expensive and require materials and resources which are often unavailable in more impoverished communities, which are at highest risk of consuming heavy metal contaminated water. An analysis of unit prices for bioderived activated carbon adsorbents found ranges from $0.3 to $22 per kilogram of adsorbent, making them relatively accessible to the general population.[33] However, adsorption of inorganic contaminants by these activated carbons is generally significantly lower than for organic contaminants, often necessitating further modifications of the adsorbent for efficient removal of heavy metals from water.[34]

1.3 ADSORBENTS

As we have discussed, the removal of contaminants from water, both organic and inorganic, is oftentimes best accomplished by adsorption processes as they tend to be more inexpensive to manufacture, have broader applications, and are generally easier to implement than their counterparts as they can be utilized in a point of use (POU) system, such as by attaching a filter containing the adsorbent material directly on the water source, such as a sink, faucet, hose, etc. A wide variety of adsorbents have been explored, ranging from organic to inorganic adsorbents. Some of the more common inorganic adsorbents studied include silica-based adsorbents,[35-40] layered double hydroxides,[41-44] inorganic polymer monoliths[45-47] and a wide variety of engineered nanoparticles, particularly iron oxide-based nanoparticles.[48-52] These inorganic adsorbents are generally used for the removal of inorganic contaminants from water, although their use for the removal and sometimes catalytic degradation of organic contaminants has also been explored.

Organic adsorbents, more specifically carbon-based adsorbents, are widespread and very commonly studied. Some of the more common carbon-based adsorbents include nanotubes (both multiwalled and single-walled),[53-57] a variety of activated carbons,[58-65] graphene/graphite and their derivatives such as oxidized graphene, reduced-graphene oxide, and derivatized reduced graphene-oxide.[66-71] These carbon-based adsorbents have been used for the removal of both organic and inorganic contaminants from water with generally mid-to-high adsorption capacities. The list of contaminants removed by these organic-based adsorbents is extensive, with the removal of organic contaminants such as phenolic compounds, dyes and dye precursors, pharmaceuticals and endocrine-disrupting compounds, and even landfill-leachate. Inorganic contaminants include a vast variety of heavy metals, commonly copper(II), lead(II), mercury(II), zinc(II), chromium(VI), and both arsenic(III) and arsenic(V).[72]

Of these carbon-based adsorbents, activated carbons are of particular interest as they can be synthesized from a vast variety of carbon precursors, given that proper carbonization time and temperature as well as activating agents are employed. Common methods of generating activated carbons include physical[73] and/or chemical processes,[74] most of which employ large polymeric carbon sources such as lignocellulosic materials and the use of metal salts or acids such as zinc chloride or phosphoric acid for their activation.[75] A type of activated carbon which utilizes natural carbon sources are called biochars, which have become a hot topic in the preparation of activated carbons due to the general availability of these carbon sources. Biochars tend to have some slight differences from the majority of activated carbons. First, due to many biochars being derived from biosources which are plant-based, biochars usually contain mineral constituents. Second, most biochars are produced by temperatures under 700 ºC without the use of an activating agent. Third, biochars in general tend to have a lower surface area than activated carbons. Finally, precursors for biochar tend to be wider than those for activated carbon and are often cheaper to procure. Biochar precursors span a wide variety of bio-sources; as a small sampling, biosourced precursors have included pinewood,[76,77] rice husk,[78,79] switch grass,[80,81] sugarcane bagasse,[82,83] peanut shell/hull,[84-86] corn stalk/straw/cobs,[87-89] wheat straw/residue,[90,91] soybean residue,[92,93] and a wide variety of sewage and animal waste.[94-96]

1.4 RESEARCH AIMS

As we have seen, most of these biochars employ large polymeric carbon sources such as lignocellulosic materials, plant residue or waste for their production. Few studies have been done on the carbonization of monomers such as monomeric glucose as the carbon source and nanoparticles such as zinc oxide as templating agents for the generation of porosities.[22,97,98] We therefore propose the use of glucose as a monomeric carbon source for pyrolysis, with the included use of zinc oxide nanoparticles as templating agents (Scheme 1.1). In more common approaches, lignocellulosic materials (wood, leaves, etc.) are left to soak in an activating solution, where the metal salts then slowly seep into the material. Depending on conditions, this may result in an uneven distribution of the activating agents, which after carbonization can results in areas which, due to the lack of activating agent, do not form porosities.[99-101] Owing to the solubility of glucose in water, we hypothesize that as we remove water from the solution containing ZnO nanoparticles and glucose begins to precipitate, glucose will arrange itself around the zinc oxide nanoparticles in a (near)homogeneous distribution. During pyrolysis, glucose will decompose to form a robust carbon matrix. After removal of the nanoparticles, a porous carbon-based adsorbent with relatively high surface area will be produced which can be used for the adsorption of organic contaminants from water. Moreover, this material can be further functionalized to work as a viable adsorbent for inorganic water contaminants, as well as infused with nanoparticles for the simultaneous adsorption and degradation of contaminants.

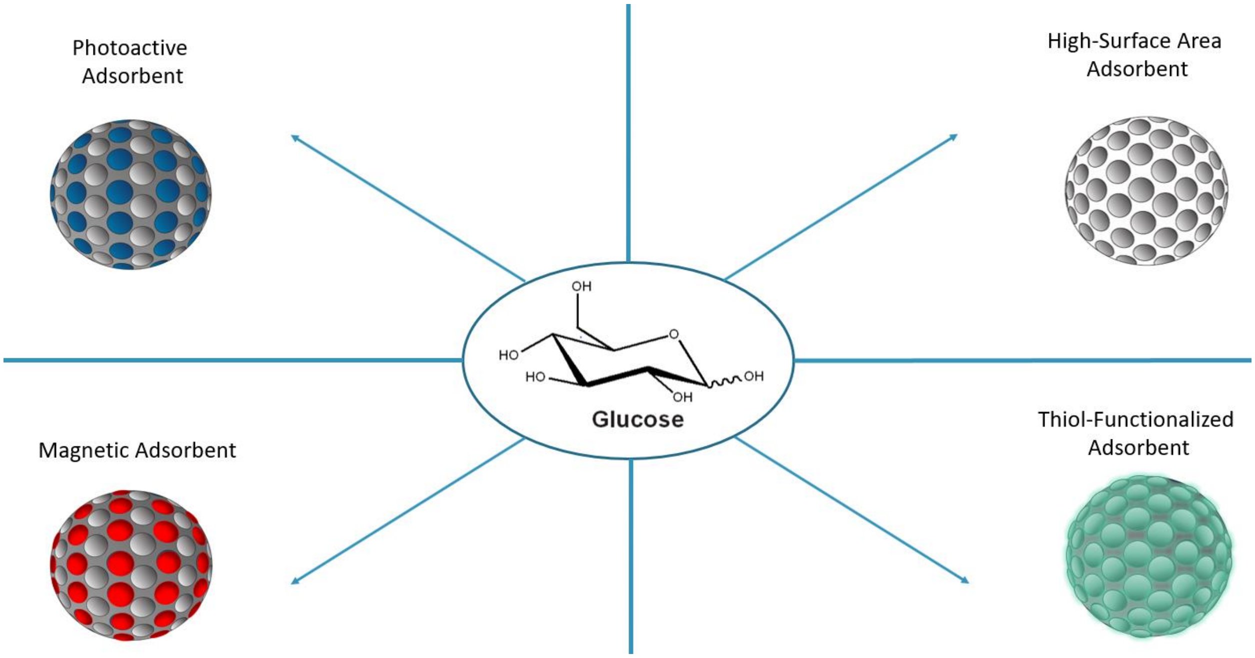

Scheme 1.1: Transformation of glucose to four separate adsorbents; a photoactive adsorbent (top, left), a high surface area adsorbent (top, right), a thiol-functionalized adsorbent (bottom, right) and a magnetic adsorbent (bottom, left).

The aims of this dissertation are multifaceted, with the goals of this project divided into four chapters:

- Aim 1: Develop an adsorbent containing TiO_2 nanoparticles for the simultaneous adsorption and photodegradation of organic pollutants (Chapter 2).
- Aim 2: Develop a high-surface area adsorbent utilizing our method for the efficient adsorption of organic pollutants (Chapter 3).
- Aim 3: Develop a one-step synthetic method for the production of a magnetic adsorbent aimed at the removal of inorganic contaminants (Chapter 4).
- Aim 4: Further functionalize the adsorbent found in Aim 2 with sulfur for the purpose of water remediation of inorganic pollutants (Chapter 5).

The remainder of this work focuses on the development of these materials and encompasses the results found for each, any outstanding outcomes and conclusions, as well as any possible future work needed to for their improvement.

Chapter 2: TiO_2-Carbon Nanoporous Composites Prepared via ZnO Nanoparticle-Templated Carbonization of Glucose for the Adsorption and Photodegradation of Organic Pollutants in Water

2.1 INTRODUCTION

Porous carbon materials are currently used for a variety of applications, from electrochemical applications such as chemical sensing,[102] energy storage and supercapacitance[103] to the adsorption of organics, both in the gas phase[104-107] and as aqueous contaminants.[97,98,108,109] For the latter, activated carbon has seen the most success in real world applications due to its high surface area, hydrophobic surface capable of further functionalization,[110] and great adsorption capacities for organic compounds. Activated carbon has been formed by physical[73] and/or chemical[74] processes; however, the use of nanoparticles to template the carbonization process to control its morphology has received less attention, with only a handful of examples reported.[97,98] The use of nanoparticles during pyrolysis and subsequent removal from the carbon material can produce unique porosities which are less likely to appear by other methods.

While carbon activation via physical and chemical means has been thoroughly explored, templating with nanoparticles has seen less attention. Having nanoparticles of a certain size present during pyrolysis and subsequently removing them from the carbon material can leave behind micro- and mesoporosities of a very uniform size. In our study we employ Zinc oxide (ZnO) nanoparticles for the templation of glucose. Zinc oxide is commercially available, relatively inexpensive, and acts orthogonally to TiO_2 (titanium oxide) in the presence of acid, allowing us to remove ZnO without damaging the TiO_2 nanoparticles. We also chose zinc oxide over magnetic nanoparticles such as magnetic iron oxide to avoid agglomeration during the mixing and carbonization processes. Zinc oxide templated carbon materials have been explored as biosensors,[102] and to the best of our knowledge nanotemplated adsorbent materials using ZnO nanoparticles as templates are scarce, and those that exist are either bimetallic zinc oxide or used a synthetic polymer as their carbon source for carbonization, not a bioavailable carbon source such as glucose.

Nanoparticles are oftentimes used to enhance the ability of carbon adsorbents to remove organic contaminants from water. The catalytic degradation of several organic pollutants has been previously explored, resulting in the elucidation of intermediates and final degradation products. Methylene blue[111] and ofloxacin,[112] for example, are found to oxidize to mineralization products such as CO_2 and heteroatoms of nitrogen and sulfur, while degradation products of tetracycline show a decrease in toxicity after photocatalysis.[113] Carbonized materials can provide an adequate anchor for catalytic nanoparticles, and as such the carbonization process has been employed to generate materials with semiconductor,[114] photocatalytic[115] and H_2 evolution[116,117] properties. Titanium oxide nanoparticles in particular have been explored for their ability to generate reactive oxygen species in water when their electrons are excited from the valence band to the conductive band, most commonly by activation using ultraviolet (UV) light.[118] Embedding TiO_2 nanoparticles to the surface of activated carbon has shown effective adsorption and degradation of organic pollutants such as phenol,[119,120] tetracycline,[121] methyl orange,[122] and humic acids,[123] amongst others. In most cases the nanoparticles are embedded to the surface of activated carbon, leaving them exposed to UV light irradiation but possibly resulting in leaching of the nanoparticles over time. We propose embedding the nanoparticles inside the activated carbon, providing a carbon matrix which will prevent, or at least minimize, possible leaching.

In this study, we explored the carbonization of glucose at 500 °C in the presence of zinc oxide and titanium oxide nanoparticles. The ZnO nanoparticles were then removed by acid treatment, leaving behind a nanotemplated activated carbon, forming our NTC (nanotemplated carbon) and NTC-TiO_2 (nanotemplated carbon with TiO_2 nanoparticles) materials. These materials were characterized by X-ray diffraction (XRD), Brunauer-Emmet-Teller (BET), scanning electron microscopy (SEM), and energy dispersive x-ray spectroscopy (EDX-S). Their adsorption and photodegradation properties were explored against methylene blue, ofloxacin, and tetracycline.

2.2 MATERIALS AND METHODS

2.2.1 Chemicals and Reagents

D-(+)-Glucose (ACS reagent), titanium (IV) oxide (nanopowder, 21 nm particle size, ≥ 99.5% trace metal basis), and zinc oxide dispersion (50% weight in water, < 35 nm particle size) were all purchased and used as-is from Sigma Aldrich.

2.2.2 Preparation of Glucose-Nanoparticle Mixtures

For the preparation of glucose-zinc oxide (Glc-ZnO) mixture (1:1 wt:wt), 2 g of glucose were dissolved in 5 mL of reverse osmosis (RO) water followed by the addition of 4 g of a 50% weight zinc oxide dispersion. The mixture was sonicated for 30 min and subsequently stirred for another 30 minutes. At this point the water was co-evaporated with reagent alcohol under reduced pressure until completely dry.

For the preparation of glucose-zinc oxide-titanium oxide (Glc-ZnO-TiO_2) mixture (2:1:1 wt:wt:wt respectively), 2 grams of glucose were dissolved in 5 mL RO water followed by the addition of 2 g of a 50% weight zinc oxide dispersion and 1 g of titanium oxide nanoparticles. Sonication, stirring and co-evaporation were performed following the protocol used for the Glc-ZnO mixture.

The abovementioned mixtures were carbonized under Argon flow for two hours at 500 °C with a ramp speed of 10 °C/min.

2.2.3 Removal of Zinc Oxide Nanoparticles

Glc-ZnO and Glc-ZnO-TiO_2 were subjected to aqua regia (AR) (7.5 mL AR / g of material) and left stirring overnight at room temperature. The samples were then centrifuged, decanted, washed with RO water and dried under reduced pressure. The materials generated after AR treatment from Glc-ZnO and Glc-ZnO-TiO_2 will hereafter be referred to as nanotemplated carbon (NTC) and nanotemplated carbon with titanium oxide (NTC-TiO_2), respectively.

2.2.4 Adsorption Capacity and Kinetic Studies

All adsorption capacity studies were performed using 10 mg of NTC, NTC-TiO_2 or commercially available activated carbon and 10 mL of the target contaminant solution (methylene blue, ofloxacin or tetracycline). Adsorption capacity solutions were done at concentrations of 10, 25, 50, 75 and 100 ppm in RO water and neutralized to a pH of 7.0 (+/- 0.2) using a 0.1 M NaOH solution. Adsorption capacity studies were done under stirring over 24 h at room temperature, at which point they were centrifuged and the supernatant analyzed by UV-VIS spectroscopy. Adsorption studies for NTC-TiO_2 were carried out separately in the dark and under UV light to compare adsorption only (dark) versus adsorption and photodegradation (UV). Experiments in the dark were covered with aluminum foil and experiments under UV light were carried out in a UV reactor under UV-B light with an intensity of 21,500 lux, as measured by a digital light meter (LX1330B).

Kinetic studies were performed using 10 mg of NTC, NTC-TiO_2 or commercially available activated carbon and 10 mL of the target contaminant. All contaminant solutions were done at a concentration of 50 ppm at pH 7. Aliquots were taken at 0 min, 7 min, 15 min, 30 min, 1h, 2h, 4h, and 24h.

2.2.5 Characterization

Carbonization was performed using a GSL-1100X from MTI Corporation. The crystal structure analysis of the carbon material and the embedded nanoparticles was performed on a Bruker Instruments D8 diffractometer (Kα radiation, λ = 0.154 nm) with a scan rate of 3 deg/min. A Hitachi H-7650 instrument was used for SEM as well as EDX-S images and a Hitachi H-7650 instrument was used for TEM images. Samples for SEM were placed as powders in 12 mm diameter carbon adhesive tabs. Samples for TEM were suspended in acetone before placement in a CF200-CU carbon support film. Image J software was used to calculate the pore size from these images. Adsorption measurements were taken through a 10.00 mm quarts cuvette using a NU-T6PC instrument purchased from Zhengzhou Nanbei Instrument Equipment corporation. The specific surface area and BJH adsorption measurements were taken using a Micrometrics surface area analyzer TriStar II 3020 instrument. Samples were heated at 85 °C and degassed overnight prior to analysis. Nitrogen adsorption-desorption isotherms were measured at 78 K in flowing nitrogen. SAXS measurements were carried out using a Xeuss 2.0 HR SAXS/WAXS system with a Cu source tuned to λ = 0.1542 nm at two sample-to-detector distances (1209 mm, and 156 mm) which yielded a Q-range of 0.008-2.5 $Å^{-1}$. All powder samples were loaded into 1 mm-pathlength polyimide tubes and sealed with epoxy. Prior to loading into SAXS capillary sample tubes, the samples were dried in a vacuum oven at 120 °C and 1 mbar for approximately 24 hr. Atmospheric water adsorbed in the materials were 0.06 g/g and 0.12 g/g of water per gram of porous material for NTC-TiO_2 and NTC, respectively.

2.3 RESULTS AND DISCUSSION

2.3.1 X-ray Diffraction

Carbonized glucose-nanoparticle mixtures, as well as NTC and NTC-TiO_2, were analyzed by X-ray diffraction (Figure 2.1). The Glc-ZnO mixture after carbonization shows well-defined peaks belonging to zincite [124] (JCPDS card number 36-1351), indicating the presence of ZnO nanoparticles within the carbon matrix. After acid treatment of NTC, trace amounts of ZnO nanoparticles can be seen, with small, broad peaks rising slightly above baseline. XRD of Glc-ZnO-TiO_2 shows the presence of both ZnO nanoparticles as well as characteristic peaks for micropowder TiO_2 in the anatase phase [125] (JCPDS card number 21-1272). Notably, NTC-TiO_2 shows the presence of TiO_2 and the absence of ZnO, demonstrating the ability of TiO_2 nanoparticles to survive acid treatment by aqua regia. The XRD profile of carbonized glucose is shown as a control, demonstrating a mostly amorphous structure.

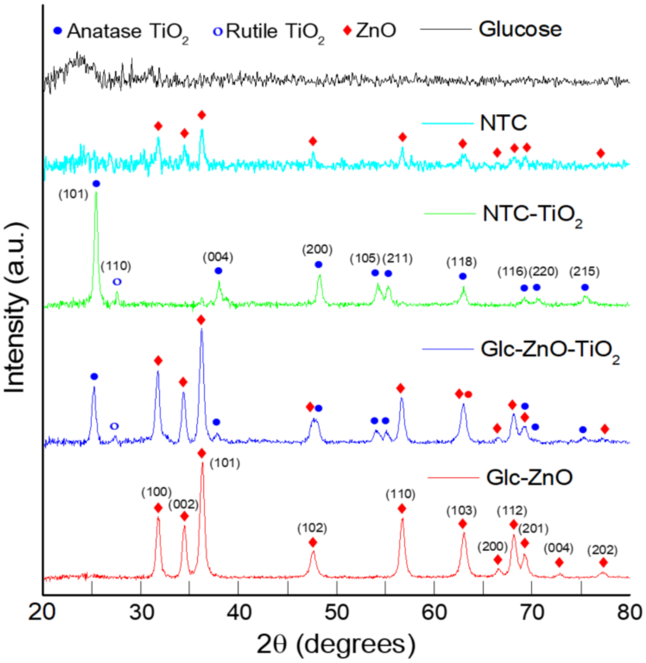

Figure 2.1: XRD diffractograms of carbonized glucose-zinc oxide (Glc-ZnO, red), carbonized glucose-zinc oxide-titanium oxide (Glc-ZnO-TiO2, blue), carbonized glucose-zinc oxide-titanium oxide after acid treatment (NTC-TiO2, green), carbonized glucose-zinc oxide after acid treatment (NTC, teal), and carbonized glucose control (Glucose, black).

2.3.2 Energy-dispersive X-ray Spectroscopy

Energy-dispersive X-ray spectroscopy measurements were taken in order to corroborate XRD data and to estimate the atomic composition of our samples (Table 2.1). Both Glc-ZnO and Glc-ZnO-TiO_2 show a high weight percentage belonging to the nanoparticles (~65% and ~77%, respectively), with carbon and oxygen percentages at relatively low levels. After acid treatment, NTC and NTC-TiO_2 both show the disappearance of Zn, with the carbon percent composition doubling for both. While the oxygen content doubled between Glc-ZnO-TiO_2 and NTC-TiO_2, it nearly quadrupled between Glc-ZnO and NTC. This suggests that much of the oxygen content of NTC-TiO_2 comes from titania nanoparticles present, which remains largely unaltered during acid treatment, while the removal of ZnO nanoparticles presents a clearer representation of the composition of our carbonaceous material alone. The carbon to oxygen weight ratio of NTC (C/O 3.71) is much higher than that of commercial glucose (1.33 C/O wt%), indicating the loss of large amounts of oxygen during the pyrolysis process, with water and small COx molecules as the most likely byproducts. The presence of chlorine in both NTC and NTC-TiO_2 is postulated to be the result of HCl addition to alkenes formed during the pyrolysis process, indicating the formation of sp^2 carbons during the elimination of oxygen under anaerobic carbonization.

Table 2.1: EDX analysis for carbonized glucose-zinc oxide (Glc-ZnO), carbonized glucose-zinc oxide after acid treatment (NTC), carbonized glucose-zinc oxide-titanium oxide (Glc-ZnO-TiO_2), and carbonized glucose-zinc oxide-titanium oxide after acid treatment (NTC-TiO_2).

	Carbon (%)	Oxygen (%)	Zinc (%)	Titanium (%)	Chlorine (%)
Glc-ZnO	30.52	4.8	64.68		
NTC	70.96	19.12			9.92
Glc-ZnO-TiO_2	13.31	9.39	57.42	19.89	
NTC-TiO_2	29.75	20.89		44.69	4.67

2.3.3 Scanning and Transmission Electron Microscopy

Scanning electron microscopy images (Figure 2.2) show rough, amorphous carbon particles containing crevices and macropores for both Glc-ZnO and Glc-ZnO-TiO_2 after carbonization. The porous nature of these materials is in stark contrast to the carbonized glucose control, which contains very smooth carbon particles with no evident crevices or porosity. Removal of ZnO nanoparticles results in a more homogeneous material of smaller carbon particle size (Figure 2.2 b,d). Transmission electron microscopy images of NTC and NTC-TiO_2 (Figure 2.3 a,b) show porosities with an average diameter of approximately 15 nm for both materials, which is in agreement with the <35 nm size of the ZnO nanoparticles used for nanotemplating.

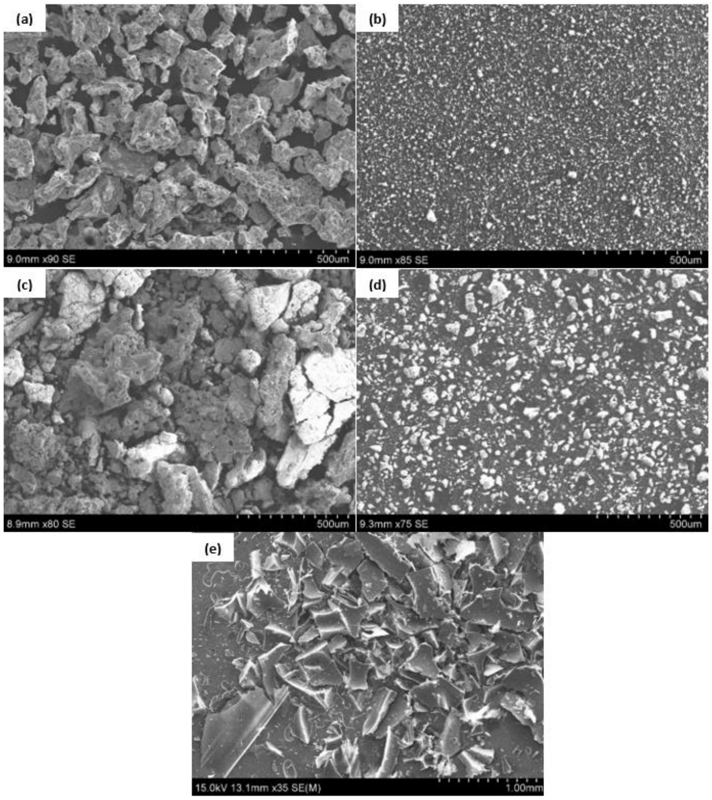

Figure 2.2: SEM images of carbonized glucose-zinc oxide (a, Glc-ZnO), carbonized glucose-zinc oxide after acid treatment (b, NTC), carbonized glucose-zinc oxide-titanium oxide (c, Glc-ZnO-TiO_2), carbonized glucose-zinc oxide-titanium oxide after acid treatment (d, NTC-TiO_2), and carbonized glucose (e, glucose).

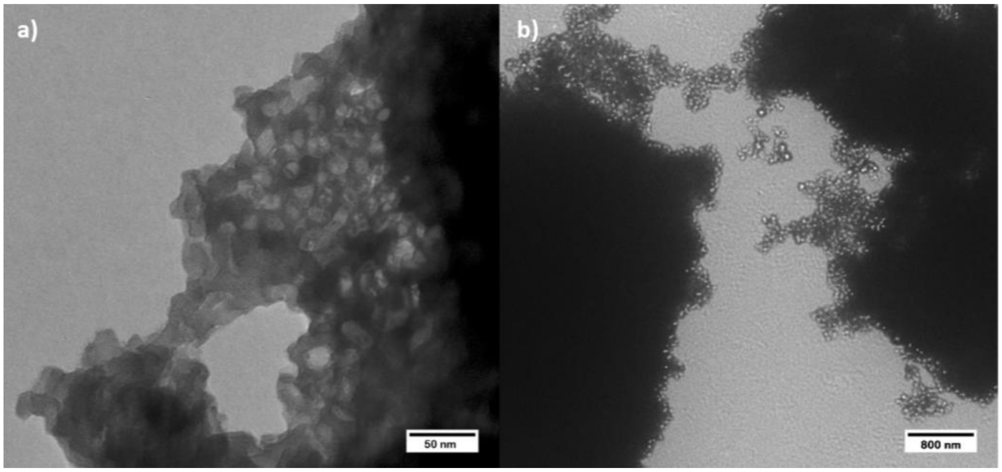

Figure 2.3: TEM images of (a) NTC and (b) NTC-TiO_2.

2.3.4 Small-angle X-ray Scattering

Small-angle X-ray scattering measurements for NTC, NTC-TiO_2 and carbonized glucose control can be seen in Figure 2.4. The control sample only shows surface scattering (Porod slope = 4) off the large powder grains which levels out at high Q to an amorphous carbon signal with no mesopores. Each porous material exhibits two gentle "bends", one at Q ~0.02 $Å^{-1}$ and the other at Q ~0.1 $Å^{-1}$, indicating the presence of two porosity length scales. Data from the wide-angle region in the I(2θ) representation can be seen in Figure 2.4B. The carbon structure is more disordered in the porous materials than the carbonized glucose, which has a sharper amorphous carbon peak at 2θ ~22.5°. The interplanar spacing is also shorter for glucose, noted by the shift to higher angle. ZnO peaks in NTC and the anatase TiO_2 peak in NTC-TiO_2 are similar to the XRD measurement. Comparison of the relative peak positions of anatase (101) and ZnO (100) in the Glc-ZnO-TiO_2 sample in the XRD data with the scattering intensities of the corresponding peaks in the SAXS measurement show a ~28-fold decrease in the ZnO intensity in the NTC sample. This shows most of the ZnO was removed with the acid treatment and the residual ZnO comprises 3-4% of the original ZnO amount before acid etching.

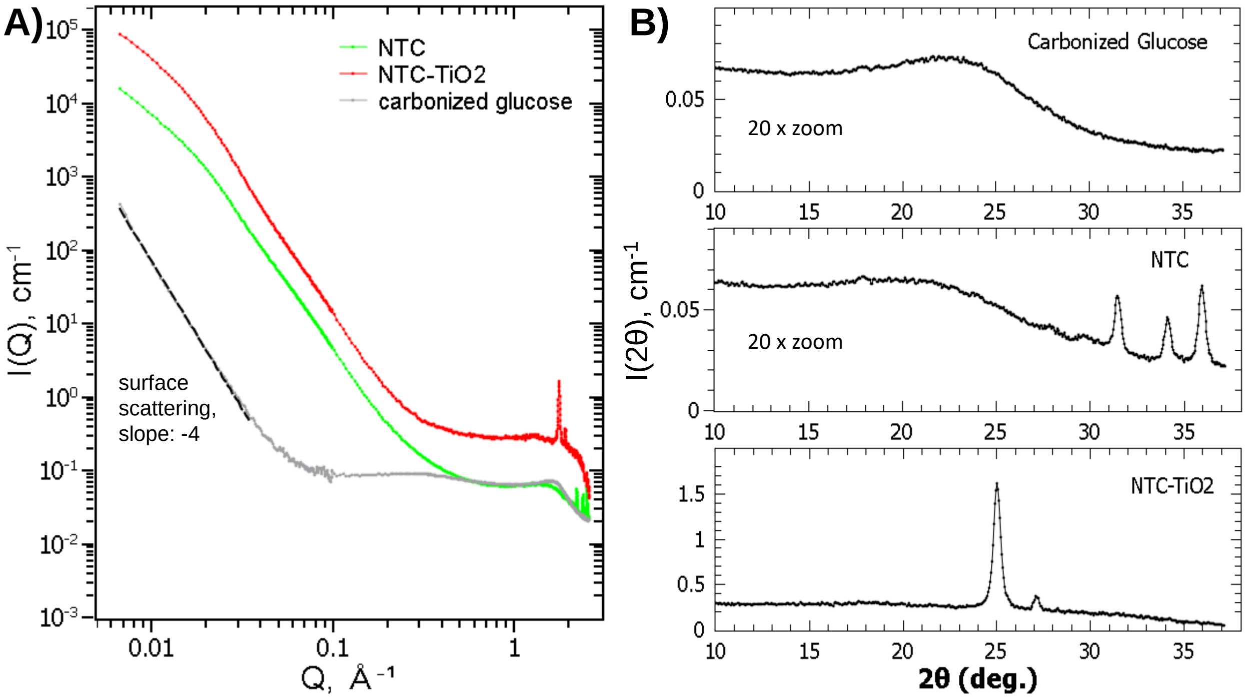

Figure 2.4: SAXS/WAXS results showing nanostructure, carbon amorphous structure and nanoparticle crystalline peaks. **A)** Comparison of NTC, NTC-TiO_2, and the carbonized glucose control sample. **B)** WAXS data in the I(2θ) representation.

From a single measurement, SAXS does not differentiate between pores that are accessible and non-accessible to the fluid. In order to check how each nanostructure fills with fluid, H_2O immersion measurements were carried out (Figure 2.5). These measurements show a uniform shift to lower SAXS intensity, I(Q), compared to the dry material reference curves. For NTC/water the intensity decrease is a factor of 4-5, consistent with complete filling of the porous carbon, whereas for NTC-TiO_2/water the decrease is approximately a factor of 3, consistent with a lower fraction of the porous matrix available for water adsorption compared to NTC. Polydisperse sphere (PS) distributions of the dry NTC and NTC-TiO_2 materials show both materials contain a narrow distribution of spheres with diameters ~5nm, and large sphere distribution with diameters of 20-30nm (Figure 2.5B, top). The NTC-TiO_2 is weighed toward larger sizes, presumably due to TiO_2 NPs that are slightly larger than the pores. PS model of dry and H_2O-immersed NTC (Figure 2.5B, middle) show similar distributions near r~12.5nm, but the H_2O immersed sample shows a slight increase at r~32nm, possibly due to the small fraction of ZnO particles that were not removed through the acid treatment.

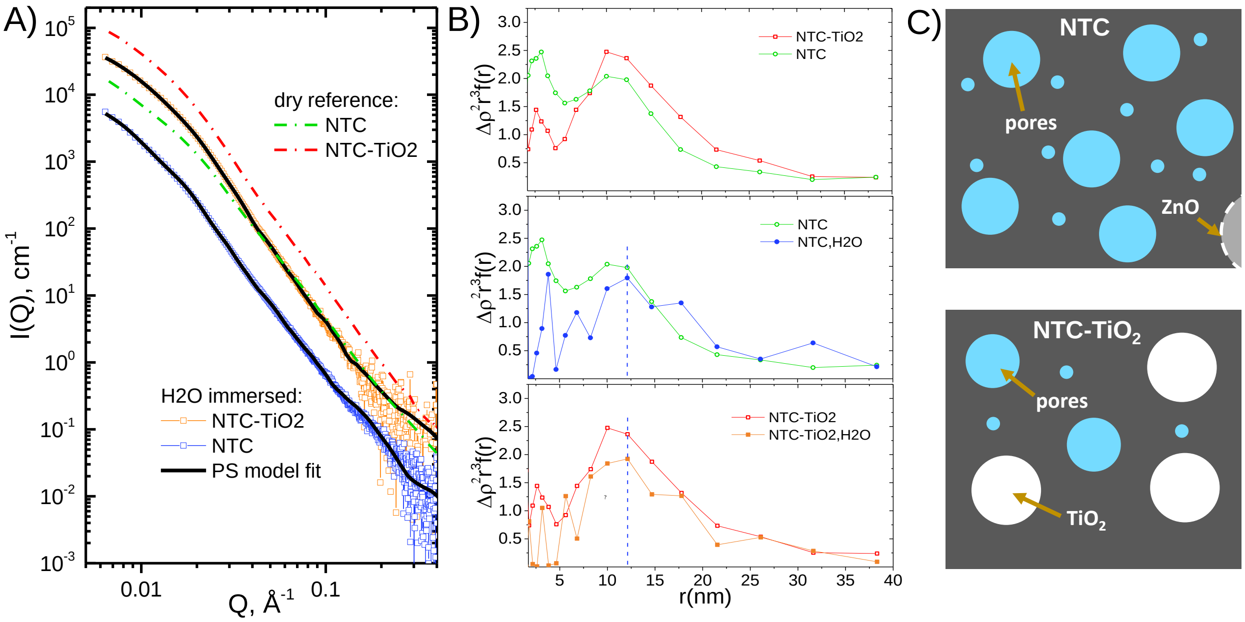

Figure 2.5: A) Polydisperse sphere distribution (PS) model fit to the SAXS data; B) Dry reference and PS model fit curves for NTC/NTC-TiO_2 (top), NTC/NTC-H_2O (middle) and NTC-TiO_2/NTC-TiO_2-H_2O (bottom); C) Diagram of the NTC and NTC-TiO_2 nanostructure based on the PS model results.

The volume-normalized pore size distribution for NTC shows there are pores with radius of 2.8 nm and 11.5 nm. The larger pore size is more polydisperse than the small pore radius. The PS model for NTC-TiO_2 similarly has a small sphere distribution centered at 2.8 nm, but the large sphere radius distribution, though its peak is at the same position as for NTC, is more heavily weighed at sphere radii greater than 12 nm. This is likely due to the presence of TiO_2 nanoparticles which are likely larger than the large pore spaces of NTC.

2.3.5 Brunauer-Emmett-Teller and Barrett-Joyner-Halenda Measurements

The BJH cumulative pore volume charts for NTC and NTC-TiO_2 can be seen in Figure 2.6, with a summary of Brunauer-Emmet-Teller surface area analysis depicted in Table 2. While the total surface area calculated for carbonized glucose was negligible, NTC and NTC-TiO_2 saw an increase to 302 and 230 m^2/g, respectively. Total pore volumes for NTC and NTC-TiO_2 were 0.486 and 0.269 cm^3/g, respectively, with 84% and 90% of the total pore volume belonging to pores in the range of 2 to 50 nm (mesoporous), as seen in Table 2.2. It should be noted that NTC-TiO_2 has lower BET surface area, average pore diameter and total pore volume than NTC, presumably due to the lower ratio of ZnO nanoparticles available for removal by acid, which is directly responsible for the generation of porosity. Microporosities (<2 nm) are not observed for these materials, indicating adsorption capabilities for gases at STP would not be ideal. However, the average pore diameter of NTC (17.08 nm) and NTC-TiO_2 (10.53 nm) is ideal for the adsorption of small organic molecules in solution, making them good candidates for water remediation of organics. This can be seen in the kinetic profiles of our materials (Figure 2.7).

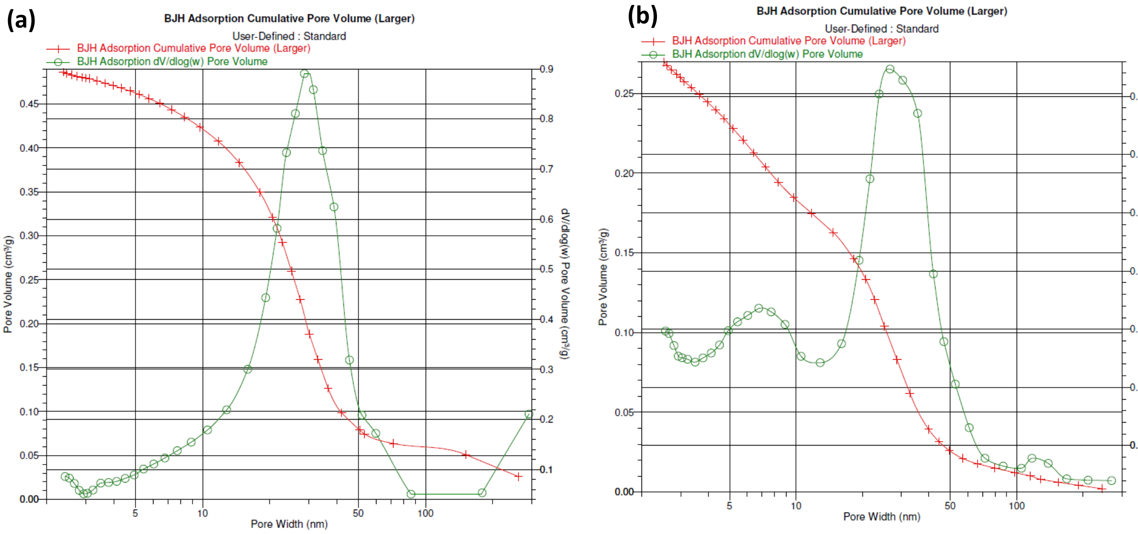

Figure 2.6: BJH Adsorption Cumulative Pore Volume charts for (a) NTC and (b) NTC-TiO_2. Peak values for both are at ~30 nm.

Table 2.2: BET surface area analysis for NTC and NTC-TiO_2 after acid treatment.

	BET Surface Area (m^2/g)	Average Pore Diameter (nm)	Total Pore Volume (cm^3/g)	Mesopore Volume (cm^3/g)	Macropore Volume (cm^3/g)	% MES*
NTC	302	17.1	0.49	0.41	0.08	84%
NTC-TiO_2	230	10.5	0.27	0.24	0.03	89%

* Percent Mesoporosity given by Mesopore Volume/Total Pore Volume Values are calculated from BJH adsorption data.

2.3.6 Adsorption Measurements

2.3.6.1 Adsorption Capacities

The adsorption capacity profiles for NTC, NTC-TiO_2 (Dark), NTC-TiO_2 (UV) and activated carbon against methylene blue, ofloxacin, and tetracycline at five different concentrations can be seen in Figure 2.7. Interestingly, NTC-TiO_2 (Dark) had very similar adsorption capacities at most concentrations against methylene blue, ofloxacin and tetracycline as NTC despite having a lower surface area. This can be attributed to hydrogen bonding between these analytes and hydroxyls present in both the carbon material and TiO_2 NPs, as well as possible ionic interactions between the contaminants and these hydroxyls at pH 7. All three contaminants can interact with our carbonized materials through hydrophobic and π-π interactions in much the same manner as they can with activated carbon. Of note is the higher adsorption/photodegradation of these contaminants across most concentrations for NTC-TiO_2 (UV) versus NTC-TiO_2 (Dark). This trend is directly attributed to ROS generation by TiO_2 NPs under UV light for NTC-TiO_2 (UV). Ultraviolet light can excite TiO_2 NPs at or near the surface of our material, thus generating highly reactive oxygen species which can degrade contaminants not only in the surrounding area, but also those trapped in the material as well. This liberates adsorption sites which can then adsorb more contaminant, thus increasing the adsorption capacity over time. It should also be noted that the adsorption capacities of NTC-TiO$_2$ (UV) taken at matching time points against these contaminants is comparatively similar to those of activated carbon at most concentrations.

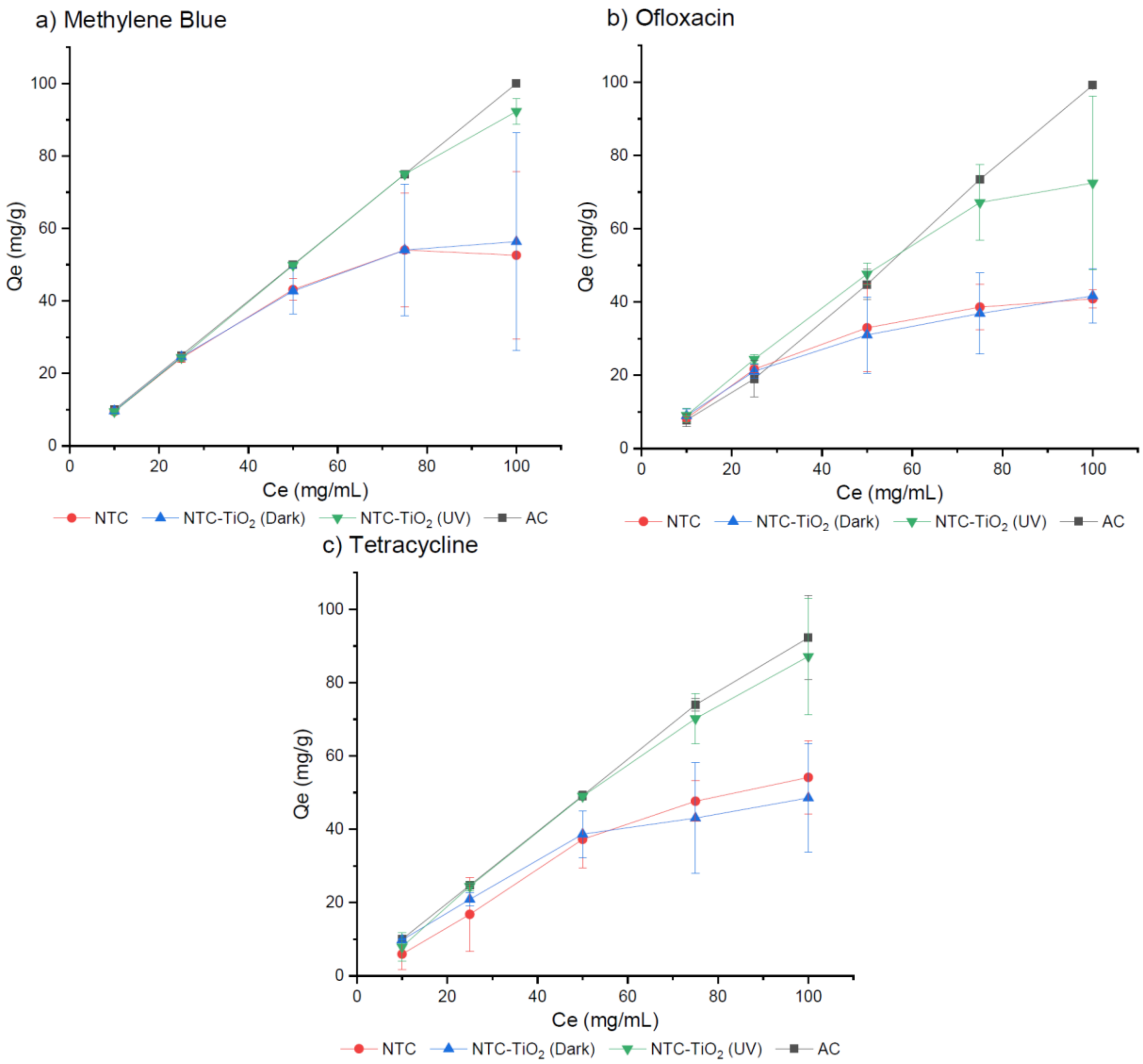

Figure 2.7: Adsorption profiles over 24h against (a) Methylene Blue, (b) Ofloxacin, and (c) Tetracycline. 10 mg of adsorbent (NTC, NTC-TiO$_2$ or activated carbon) were exposed to 10 mL of a pH 7 contaminant solution (10, 25, 50, 75, and 100 ppm) at room temperature. *Q$_e$ values for NTC-TiO2 (UV) are a representation of the total decrease in contaminant resulting from adsorption and degradation.

2.3.6.2 Kinetic Studies

Kinetic adsorption studies were performed for all four contaminants over seven time points (0 min, 7 min, 15 min, 30 min, 1h, 2h, and 4h) and can be seen in Figure 2.8. NTC adsorbed all contaminants at a faster rate than a commercially available activated carbon control, as can be seen from t = 0 min across all contaminants. This is attributed to the higher surface area of NTC as compared to NTC-TiO_2, which results in more surface sites and better permeation of the contaminants into NTC than NTC-TiO_2. NTC was capable of adsorbing 91% of a 50 ppm methylene blue solution within immediate contact, 64% of Ofloxacin and 43% Tetracycline within the same time period. This is in stark comparison to activated carbon which only adsorbed 70% methylene blue, 17% ofloxacin and 40% tetracycline within the same time period. Within the first 7 minutes of contact NTC adsorption increased to 97% methylene blue, 79% ofloxacin and 75% tetracycline. Adsorption of the contaminants onto NTC-TiO_2 at 7 min is nearly equal under both dark and UV light conditions, indicating that the decrease in contaminant concentration is initially due mostly to adsorption of the material, not degradation by ROS. However, as time progresses, the percentage of each contaminant present in the solution decreases at a higher rate for NTC-TiO_2 under UV light due to a combination of both adsorption by the material and photodegradation by reactive oxygen species. This can be seen by the rapid increase in Q_e for NTC-TiO_2 against all contaminants, with adsorption values nearing or reaching those of our activated carbon control.

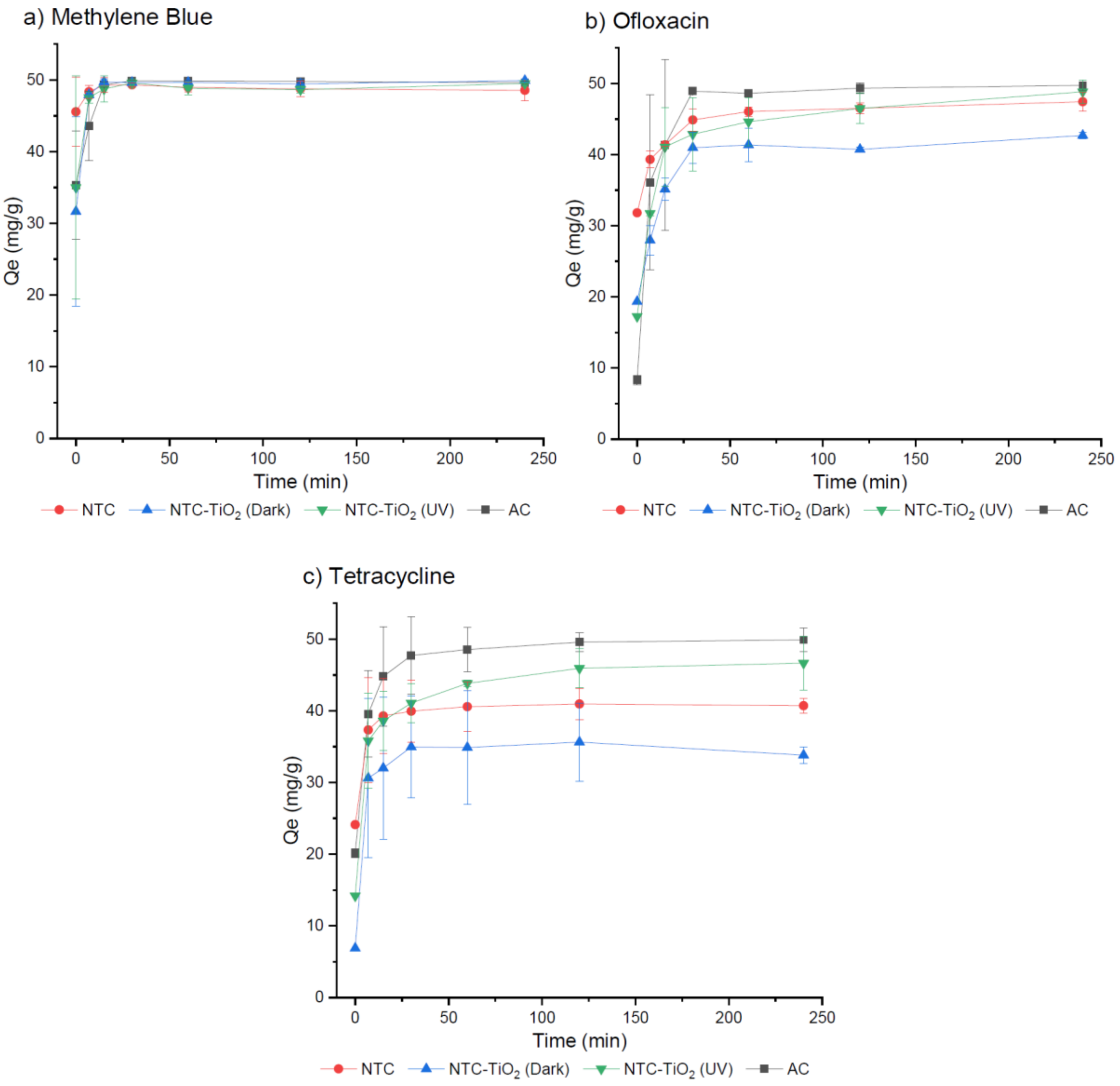

Figure 2.8: Kinetic study profiles against (a) Methylene Blue, (b) Ofloxacin, and (c) Tetracycline. 10 mg of adsorbent (NTC, NTC-TiO$_2$ or activated carbon) were exposed to 10 mL of a 50 ppm pH 7 contaminant solution at room temperature. Aliquots were taken at 0 min, 7 min, 15 min, 30 min, 1h, 2h, and 4h. *Q$_e$ values for NTC-TiO2 (UV) are a representation of the total decrease in contaminant resulting from adsorption and degradation.

2.4 CONCLUSION

An adsorbent material containing TiO_2 nanoparticles embedded onto a carbon matrix was successfully synthesized via the carbonization of glucose containing ZnO/TiO_2 nanoparticles followed by acid removal of ZnO, leaving behind a porous material capable of both adsorption and photodegradation of organic contaminants. The successful removal of ZnO nanoparticles after carbonization of glucose was proven by XRD, EDX and SAXS, which showed only trace amounts of ZnO NPs left after acid treatment. TiO_2 NPs are shown to be unaffected by the acid treatment. BET surface area analysis and SAXS experiments both show the appearance of porosities, with average pore diameters ranging from 2.8 and 11.5 nm in SAXS to 17.1 nm (NTC) and 10.5 nm (NTC-TiO_2) by BJH analysis. Both NTC and NTC-TiO_2 show fast adsorption profiles against methylene blue, ofloxacin, and tetracycline (pH 7, 50 ppm). Exposure of NTC-TiO_2 to UV light results in a lower contaminant concentration in solution over 24h than NTC, despite NTC-TiO_2 having lower porosity and surface area. We believe this is the result of a combination of adsorption by NTC-TiO_2 and photogeneration of ROS which can degrade contaminants contained both in solution and adsorbed onto the material.

Chapter 3: Zinc Oxide Nanoparticle-templated Conversion of Glucose to a High Surface Area Biocarbon for the Removal of Organic Pollutants in Water

3.1 INTRODUCTION

The presence of organic contaminants in water is of pressing concern due to the harmful effects which can occur from prolonged exposure to these chemicals. Amongst these contaminants are dyes and dye precursors, such as methylene blue (MB) and 2-naphthol, respectively. As many as 7 x 10^5 tons of dye are produced annually, with up to 15% of the dyes being lost in the effluent during the dyeing process.[126] Ingestion of methylene blue can result in nausea, vomiting, mental confusion and even methemoglobinemia.[127,128] Organic dyes have also been shown to be detrimental to aquatic life.[129] Since many dyes are resistant to light, oxidizing agents, and biodegradation, one of the best approaches for the removal of these contaminants from water is adsorption.[10,130]

Phenolic compounds such as 2-naphthol are another group of organic water contaminants which can be highly detrimental to our health, as can be evidenced by their inclusion on the priority pollutant list by the US Environmental Protection Agency.[131] 2-Naphthol is used in many industrial products, predominantly pesticides, oil and their residues, and Sudan dyes.[132,133] Studies have shown that ingestion of water contaminated with 2-naphthol can result in kidney malfunction and problems with blood circulation in humans.[134] To complicate matters, these pollutants have also shown high resistance to light, heat, biodegradation and moderate oxidizing conditions, making their remediation complicated.[135,136]

Bisphenol-A (BPA), a plasticizer used for the widespread synthesis of polycarbonate plastics and epoxy resins, is another common organic contaminant in water. BPA falls in a class of organic molecules called synthetic estrogens, many of which are believed to contribute to breast, prostate and testicular cancers.[137,138] Three million tons of BPA were estimated to have been produced worldwide in 2003,[139] and despite bans to prevent BPA from being used in items such as children's food and drink containers, BPA production remains high.[140] BPA has been shown to induce mutations in ovarian cells and increase cell proliferation in breast and prostate cells.[141]

Remediation of water from organic pollutants such as the ones mentioned here has received much attention, with methods such as physical adsorption,[17,18,142,143] chemical reduction/oxidation,[19,20,144] electrochemical degradation,[21] photocatalytic degradation,[22,23] and even biological methods[24] having been implemented for the removal and/or degradation of these contaminants. From these methods, adsorption is often the preferred method for remediation due to its low cost and ease of use, with activated carbons seeing the most success in real world applications. Common methods of generating activated carbons include physical[73] and/or chemical processes,[74] most of which employ large polymeric carbon sources (such as lignocellulosic materials) and metal salts or acids such as zinc chloride or phosphoric acid for activation.[75] Activation of these polymeric carbons for the production of biochar requires soaking the material in water containing these acids for long periods of time, which may result in a less than ideal homogeneity along its fibrous network. This lack of homogeneity can result in a porous adsorbent with drastically different surface area and pore size from one region to another, or even from batch to batch. To achieve a highly homogeneous carbon mixture before carbonization, we employ zinc oxide nanoparticles as a sacrificial template around which glucose can intercalate. Few studies have been done on the carbonization of monomers such as glucose as the carbon source and nanoparticles such as zinc oxide as templating agents for the generation of porosities.[22,97,98,145]

Herein we propose the carbonization of glucose in the presence of zinc oxide nanoparticles to form an adsorbent material for the remediation of water from methylene blue, 2-naphthol and bisphenol-A. A homogeneous mixture of the two was carbonized under inert atmosphere at 1000 ºC for two hours, resulting in the reduction of Zn(II) and sublimation of zinc(0),[146] yielding a porous carbon material *in-situ* which we refer to as nanotemplated carbon (NTC). This material was then characterized by x-ray diffraction (XRD), Brunauer-Emmett-Teller (BET), Barrett-Joyner-Halenda (BJH) and elemental mapping. Its adsorption properties were analyzed under various concentrations and pH, and the data was modeled using the Langmuir and Freundlich isotherm models. Its kinetic properties were also explored, with the data further analyzed using pseudo-first order, pseudo-second order and intraparticle diffusion kinetic models.

3.2 MATERIALS AND METHODS

3.2.1 Chemicals and Reagents

D-(+)-Glucose (ACS reagent), zinc oxide dispersion (50% weight in water, <35 nm particle size) were both purchased from Sigma-Aldrich. Sand (particle size 30-40 mesh) and PTFE filters (25 mm diameter, 0.2 μm porosities) were purchased from VWR.

3.2.2 Preparation and Carbonization of Glucose-Nanoparticle Mixtures

For the preparation of glucose-zinc oxide (Glc-ZnO) mixture (1:1 wt:wt), 1.5 g of glucose and 1.5 g of ZnO NPs were dissolved/suspended in 20 mL of reverse osmosis (RO) water. The mixture was sonicated for 30 min and subsequently stirred for another 30 minutes. At this point the water was evaporated under reduced pressure using a rotary evaporator until mostly dry. The Glc-ZnO mixture was further allowed to dry under reduced pressure via vacuum pump overnight.

When fully dry, the Glc-ZnO mixture was weighed, transferred to a quartz crucible and placed in the furnace. In order to maintain an inert atmosphere, the furnace was argon-flushed for 30 min prior to carbonization, then carbonized under constant argon flow for two hours at 1000 °C with a ramp speed of 10 °C/min, with a recovery of 0.239 g of carbonized material.

3.2.3 Preparation of Solutions for Adsorption Studies

For all solutions, RO water was adjusted with 0.1 M HCl or 0.1 M NaOH solutions to a pH of 3, 7 or 10, respectively.

For the preparation of 1000 ppm methylene blue stock solution, 250 mg were placed in a 250 mL volumetric flask and filled slowly until close to the mark with the corresponding acidic, neutral or basic water (pH 3, 7 or 10), taking care to sonicate to ensure all the MB was dissolved. When near the mark, the pH was once again measured and adjusted if necessary, then filled to the mark.

For the preparation of 1000 ppm 2-naphthol stock solution, 250 mg were placed in a 250 mL volumetric flask. For pH 7 stock solution, 2-Naphthol was first dissolved in 25 mL of 2-propanol before filling it near the mark with pH 7 RO water. For pH 3 stock solution, 2-Naphthol was first dissolved in 25 mL DMSO, then filled near the mark. For pH 10 solution, 2-Naphthol was first dissolved in 25 mL DMF before filling near the mark. The pH of each solution was again measured and adjusted if necessary, then filled to the mark with their corresponding RO water.

For the 1000 ppm bisphenol-A stock solution, 250 mg were placed in a 250 mL volumetric flask. For pH 7 stock solution, BPA was first dissolved in 25 mL of methanol, then filled with pH 7 RO water near the mark. For pH 3, BPA was first dissolved with 25 mL reagent alcohol and then filled near the mark. For pH 10, BPA was first dissolved in 25 mL of methanol, then slowly filled to the mark with pH 10 RO water, adding reagent alcohol if it began to precipitate out of solution. The pH of each solution was taken again and adjusted if necessary, then filled to the mark with RO water of their corresponding pH.

Solutions of 250, 500, and 750 ppm for MB, 2-naphthol and BPA were all made from the corresponding stock solutions using a 100 mL volumetric flask.

3.2.4 Adsorption Capacity and Kinetic Studies

All adsorption capacity studies were performed using 10 mg of NTC or activated carbon (AC) and 10 mL of the target contaminant solution. Adsorption capacity solutions were done at three separate pH (pH 3, pH 7 and pH 10) and at four separate concentrations (250, 500, 750 and 1000 ppm). Adsorption capacity studies were done under stirring over 24 h at STP, at which point they were centrifuged and the supernatant diluted for analysis by UV-Vis spectroscopy. All dilutions were made using water adjusted to the corresponding pH for the study. UV-Vis aliquots for methylene blue were diluted to 1% for Ci-1000 ppm, 1.3% for C_i-750 ppm, 2% for C_i-500 ppm and 4% for C_i-250 ppm. Aliquots for 2-naphthol and bisphenol-A were diluted to 10% for C_i-1000 ppm, 13% for C_i-750 ppm, 20% for C_i-500 ppm and 40% for C_i-250 ppm.

Kinetic studies were performed using 15 mg of NTC or AC and 15 mL of the target contaminant. All contaminant solutions were done at a concentration of 100 ppm at a pH of 7 ($^+/-$ 0.2). One mL aliquots were taken at 0 s, 15 s, 30 s, 1 min, 2 min, 5 min, 15 min, 30 min, 1 h, 2 h and 4 h, and subsequently filtered through a 0.2 μm PTFE syringe filter. Aliquots for UV-Vis spectroscopy analysis for methylene blue were diluted to 10%. 2-naphthol and bisphenol-A aliquots were measured directly after filtration.

3.2.5 Experimental Data Modeling

Langmuir and Freundlich adsorption isotherm models were applied to the pH dependent adsorption capacity data, while pseudo-first order, pseudo-second order and intra-particle diffusion models were applied to the kinetic experiments data. A summary of each model can be found below:

a) Langmuir isotherm model: This model quantitatively describes the monolayer adsorption of the adsorbate onto the surface of the adsorbent with no further interaction between the molecules, after which point no further adsorption takes place. Of the four linear forms of the Langmuir equation, type I was chosen for this study due to the minimal deviations from the fitted equation.[147,148] Langmuir type I isotherm can be seen in Equation 1, where C_e (mg/L) is the adsorbate concentration at equilibrium, Q_e (mg/g) is the adsorption capacity of the adsorbent at equilibrium, Q_{max} (mg/g) is the maximum adsorption capacity, and K_L is the Langmuir constant related to the net enthalpy of adsorption.[149]

$$\frac{C_e}{Q_e} = \frac{1}{Q_{max}K_L} + \frac{C_e}{Q_{max}} \qquad \text{Equation 1}$$

b) Freundlich isotherm model: This isotherm is an empirical formula describing the non-ideal and reversible adsorption of the adsorbate onto the adsorbent, often applied to multilayer adsorption.[150] The Freundlich isotherm can be expressed by Equation 2, where Q_e (mg/g) is the adsorption capacity at equilibrium, C_e (mg/L) is the adsorbate concentration at equilibrium, K_F is the Freundlich constant and 1/n is the intensity of adsorption. K_F and 1/n are obtained from the intercept and slope of the LnC_e vs LnQ_e plot, respectively.

$$\ln(Q_e) = \ln(K_F) + \frac{1}{n}\ln(C_e) \qquad \text{Equation 2}$$

c) Pseudo-first order model: The pseudo-first order equation, also known as the Lagergren equation, is used to describe the rate of sorption in the liquid-phase system.[151] It is defined by Equation 3, where Q_e (mg/g) is the adsorption capacity, Q_t (mg/g) is the adsorption at time t (in minutes) and k_1 is the pseudo-first order rate constant (min^{-1}).

$$\log(Q_e - Q_t) = \log(Q_e) - \frac{k_1}{2.303}t \qquad \text{Equation 3}$$

d) Pseudo-second order model: The pseudo-second order equation is used when the overall sorption kinetics are attributed to the rate of direct adsorption/desorption process, often seen as a type of chemical reaction.[152,153] It assumes that the rate of ion exchange occurring on the surface is responsible for the removal kinetics. It can be described by Equation 4, where t is the time in minutes, Q_t (mg/g) is the adsorption at time t, Q_e (mg/g) is the adsorption capacity at equilibrium and k_2 is the pseudo-second order rate constant (g $mg^{-1}min^{-1}$).

$$\frac{t}{Q_t} = \frac{1}{k_2 {Q_e}^2} + \frac{t}{Q_e} \qquad \text{Equation 4}$$

e) Intraparticle diffusion model: Intraparticle diffusion is one of the governing rate-limiting steps in a typical liquid-solid adsorption, along with film diffusion and mass action.[154] Weber-Morris found that in many cases, adsorption varies almost proportionally with the square root of t.[155] This relationship can be seen in Equation 5, where Q_t (mg/g) is the adsorption at time t, k_i (mg $g^{-1}min^{0.5}$) is the intra-particle diffusion rate constant, and C (mg/g) is a constant related to the boundary layer thickness.

$$Q_t = k_i t^{0.5} + C \qquad \text{Equation 5}$$

3.2.6 Flow Adsorption Study

For the preparation of the adsorbent, 1 g of NTC was finely ground and mixed with 100 g of sand. A 250 mL glass chromatographic column was first fitted with a cotton support, followed by the dry addition of the NTC/sand mixture, and finally with 20 g of sand to prevent the leaching of our adsorbent by the added water. The column was first washed with 0.5 L of tap water, at which point filtration of a 20 ppm MB solution made in tap water was started. The continuous flow of this 20 ppm MB solution, with a controlled rate of 4.5 mL/min, was continued for 15 L with UV-Vis measurements taken at regular intervals.

3.2.7 Characterization

Carbonization was performed using a GSL-1100X from MTI Corporation. The crystal structure analysis of the carbon material and the embedded nanoparticles was performed on a Panalytical Empyrean 2 diffractometer (Cu anode, Kα radiation, λ = 1.54 nm) with a scan rate of 1.7 deg/min. A Hitachi S-4800 instrument was used for SEM as well as EDS imaging. Samples for EDS were placed as powders in 12 mm diameter carbon adhesive tabs. UV-Vis adsorption measurements were taken through a 10.00 mm quarts cuvette using a NU-T6PC instrument purchased from Zhengzhou Nanbei Instrument Equipment corporation. The specific surface area and BJH adsorption measurements were taken using a Micrometrics surface area analyzer TriStar II 3020 instrument. Samples were heated at 85 °C and degassed overnight prior to analysis. Nitrogen adsorption-desorption isotherms were measured at 78 K in flowing nitrogen.

3.3. RESULTS AND DISCUSSION

3.3.1 X-ray Diffraction

X-ray diffractograms for NTC as well as control ZnO nanoparticles can be seen in Figure 3.1. After carbonization at 1000 ºC for two hours under argon, we observe none of the characteristic ZnO diffractogram peaks left in our material. This is expected, as Zn(II) can be reduced by carbon at temperatures exceeding 900 ºC, at which point they become volatile and sublime from the reaction mixture.[146] For the range of 20 to 80 degrees we observe no sharp signals in our material, indicating a highly amorphous composition. However, the appearance of a small, broad signal at 29.5 degrees is attributed to the carbon material itself, as graphenic carbons have been observed to show this broad (0 0 2) reflection between 20 and 30 degrees.[156,157] In addition, the broad peak centered around 43° indicates the presence of honeycomb structures formed by sp^2 hybridized carbons.[158]

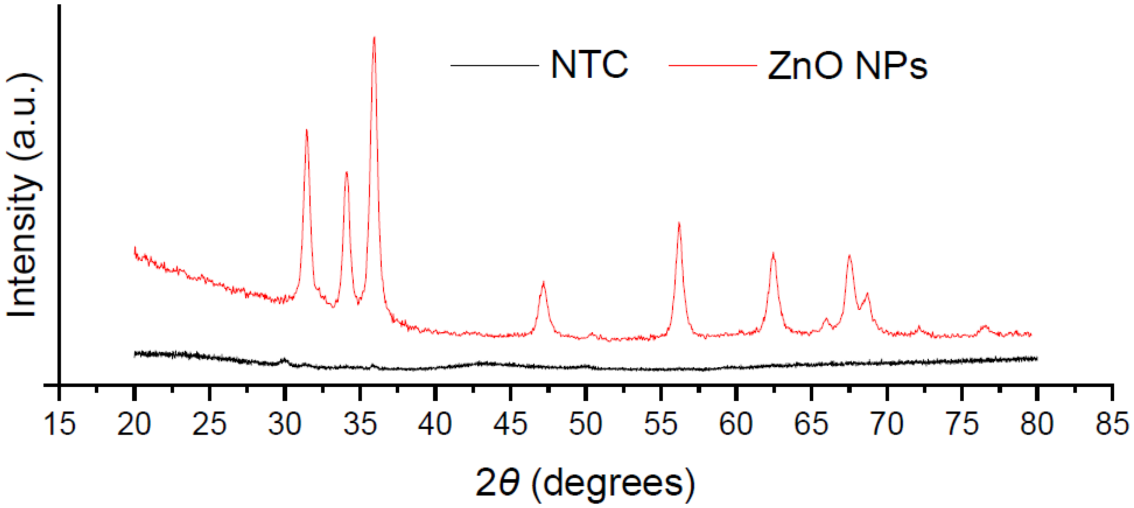

Figure 3.1: X-ray diffractogram of NTC (black) and ZnO nanoparticles (red).

3.3.2 Energy Dispersive X-ray Spectroscopy

Elemental mapping of NTC shows the bulk of the material is composed of carbon and oxygen, as expected (Figure 3.2). Table 3.1 summarizes the atomic percentages present in the material. We observe a carbon atomic composition of 90.2%, with oxygen making up another 8.2%. The other 1.6% atomic composition is due to impurities such as sodium, magnesium, aluminum, silicon, phosphorus, as well as some tin and molybdenum. These impurities can be attributed to contaminated crucible, quartz tube, desiccator, and general laboratory ambience. The high carbon content is expected, as glucose undergoes large amounts of dehydration at these high temperatures under inert atmosphere. The majority of the lost mass is attributed to the loss of ZnO, as well as water and small CO_x species.[159-161]

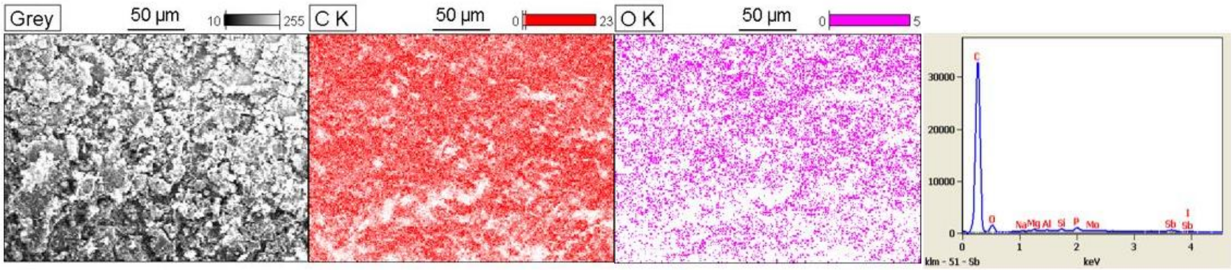

Figure 3.2: Elemental Mapping of NTC showcasing carbon and oxygen content.

3.3.3 BET and BJH Analysis

The parameters employed during pyrolysis have a large impact upon the physical characteristics of the carbonized material, affecting total surface area and pore size.[86,162-165] Surface area in particular is largely affected by pyrolysis temperature. The general trend follows that, as pyrolysis temperature is increased, surface area also increases up to a certain threshold. This trend is also observed in our material. Keeping the ramp rate and pyrolysis time the same, when pyrolysis temperature is set at 500 ^{o}C, the resulting NTC has a surface area of 302 m^2/g. When pyrolysis temperature is increased to 1000 ^{o}C, the surface area drastically increases to 1228.19 m^2/g, as evidenced by the Brunauer-Emmett-Teller (BET) displayed in Figure 3.3A. We can see a calculated total surface area of 1228.19 m^2/g, with most of this area taking place at higher relative pressures. The adsorption/desorption curve fits a Type IV isotherm model, indicating a porous material with low energy for adsorbent-adsorbate interaction. From the BJH adsorption isotherm (Figure 3.3B) we can see that a large portion of the pore volume is allocated to cavities with pore width between 10 and 100 nm, with a calculated BJH adsorption average pore width of 14.74 nm. However, a large amount of area is shown for cavities under 5 nm in width, as can be seen in Figure 3.3C. From this we can gather that our material has pores in the range of micro-(<2 nm), meso- (2 - 50 nm) and macroporosities (>50 nm).

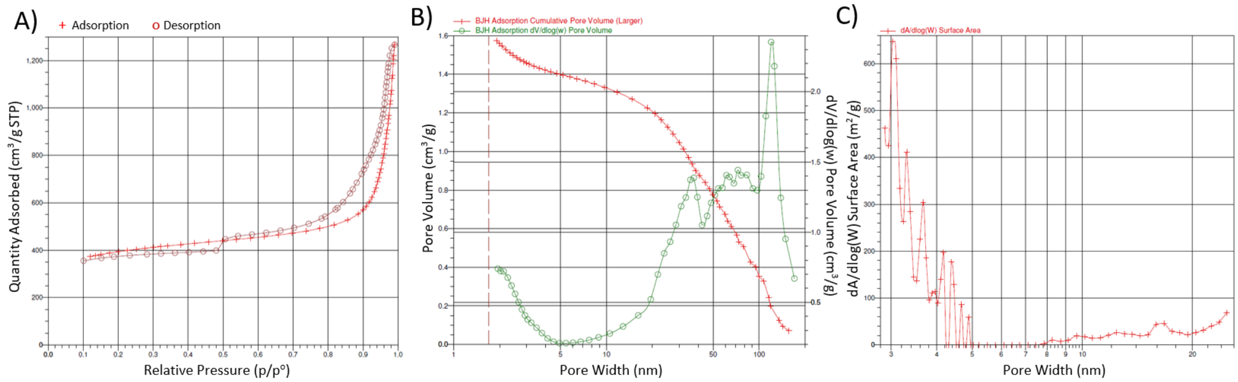

Figure 3.3: A) BET surface area, B) BJH desorption cumulative pore volume, and C) surface area vs. pore width plots for NTC.

3.3.4 Transmission Electron Microscopy

Transmission electron microscopy images of NTC (Figure 3.4) shows a highly irregular, porous material. The average diameter of these porosities was calculated to be 20.79 nm by ImageJ software. Smaller porosities were observed, and these porosities were calculated to have an average diameter of 3.14 nm by ImageJ software. Averaging both the larger and smaller porosities together, we calculate an overall average pore diameter size of 16.37 nm, which is in agreement with the 14.74 nm pore width calculated from BJH.

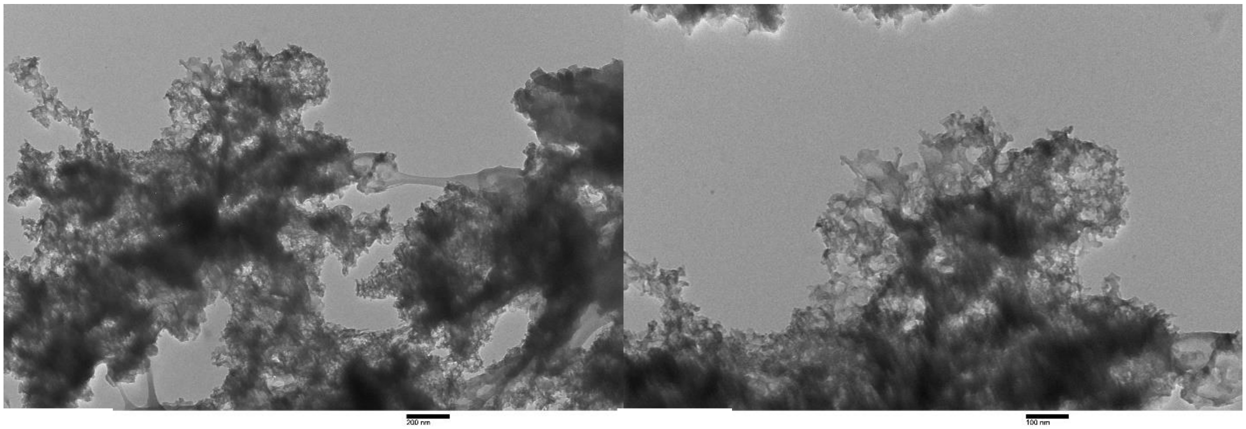

Figure 3.4: TEM images of NTC. Average porosities calculated to be 14.74 nm in diameter.

3.3.5 Adsorption Studies

3.3.5.1 Adsorption Capacity and pH-dependent Studies

Adsorption capacity and pH dependent studies for NTC against methylene blue, 2-naphthol and bisphenol-A were performed. Molecular structures of the contaminants can be seen in Figure 3.5, and the adsorption curves can be seen in Figure 3.6.

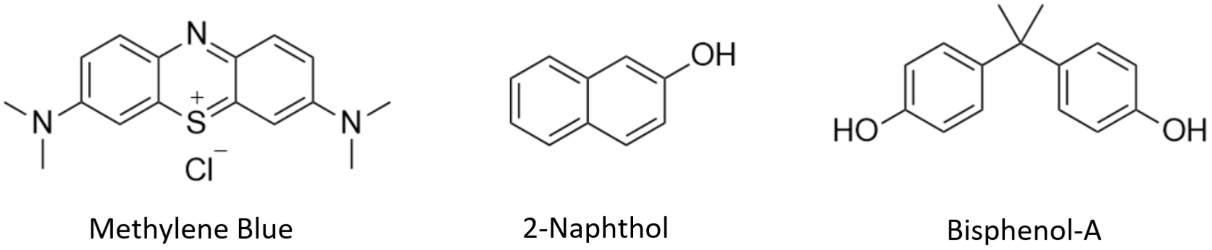

Methylene Blue 2-Naphthol Bisphenol-A

Figure 3.5: Molecular structures of methylene blue, 2-naphthol and bisphenol-A shown as their neutral species.

For methylene blue (Figure 3.6A) we can see the general trend of higher adsorption capacity as pH increases. At acidic pH, adsorption capacity seems to reach a limit at 313 mg/g. As the pH is increased to neutral, adsorption capacity also increases to 539 mg/g, while adsorption capacity at basic pH it reaches 877 mg/g, nearly a 1:1 adsorbent/adsorbate ratio. This trend can be attributed to the overall charge of methylene blue at these different pH levels. Under acidic conditions, the amine in methylene blue can become protonated, resulting in a net-positive charge in the molecule. This interferes with its adsorption onto our material, which consists mostly of C-C sigma and pi bonds and thus adsorbs mostly molecules which are net-neutral in nature via hydrophobic and π-π interactions. These positive charges in methylene blue result in repulsion between adjacent MB molecules adsorbed onto our material, decreasing the overall adsorption capacity. At neutral pH methylene blue is deprotonated once again, resulting in a net-neutral molecule which can more easily interact with our hydrophobic adsorbent without repulsion from adjacent molecules. In fact, this trend is prevalent even at pH 10 up to 750 ppm concentration, where the adsorption of methylene blue onto our material is nearly equivalent at both pH 7 and pH 10. At a concentration of 1000 ppm and pH 10 we can see a large increase in adsorption onto our material, possibly due to a shift towards a Freundlich adsorption model where adsorption is multilayered, not single-layered as in a Langmuir model. This large decrease in methylene blue concentration could also be the result of precipitation of methylene blue from solution, although no precipitate was observed on the reaction vessels or the stock solutions.

Adsorption of 2-naphthol onto NTC (Figure 3.6B) is also highly pH-dependent. At acidic pH we observe the lowest adsorption onto our material, reaching an experimental maximum of 303 mg/g. Under these conditions the hydroxyl in 2-naphthol can become protonated, resulting in a net-positive charge which not only interferes with adsorption onto a hydrophobic layer, but also results in repulsion between neighboring adsorbates on the surface, resulting in sub-optimal adsorption. Under basic conditions we see a rise in the adsorption maximum to 421 mg/g due to deprotonation of the hydroxyl, resulting in a net negative charge. However, this charge is resonance stabilized and distributed throughout the molecule. This distribution of charge is perhaps responsible for the higher adsorption of 2-naphthol onto our material at pH 10 over pH 3, where the positive charge is localized at a single point. At neutral pH we observe the highest experimental adsorption capacity at 737 mg/g due to the hydroxyl remaining protonated, resulting in a net-neutral molecule which can better interact with our hydrophobic material without repulsion from nearby molecules.

Adsorption of BPA (Figure 3.6C) follows a similar trend to the adsorption of 2-naphthol onto our material. At basic pH, BPA becomes deprotonated, thus affecting its adsorption onto the hydrophobic adsorbent and resulting in an adsorption maximum of 392 mg/g. At pH 3 there is the possibility of protonation of one of the hydroxyls, which results in a slightly higher adsorption maximum of 459 mg/g. As with 2-naphthol, we see the highest experimental adsorption capacity (563 mg/g) under neutral conditions, attributed to the absence of a net charge on BPA and higher interaction with the adsorbent.

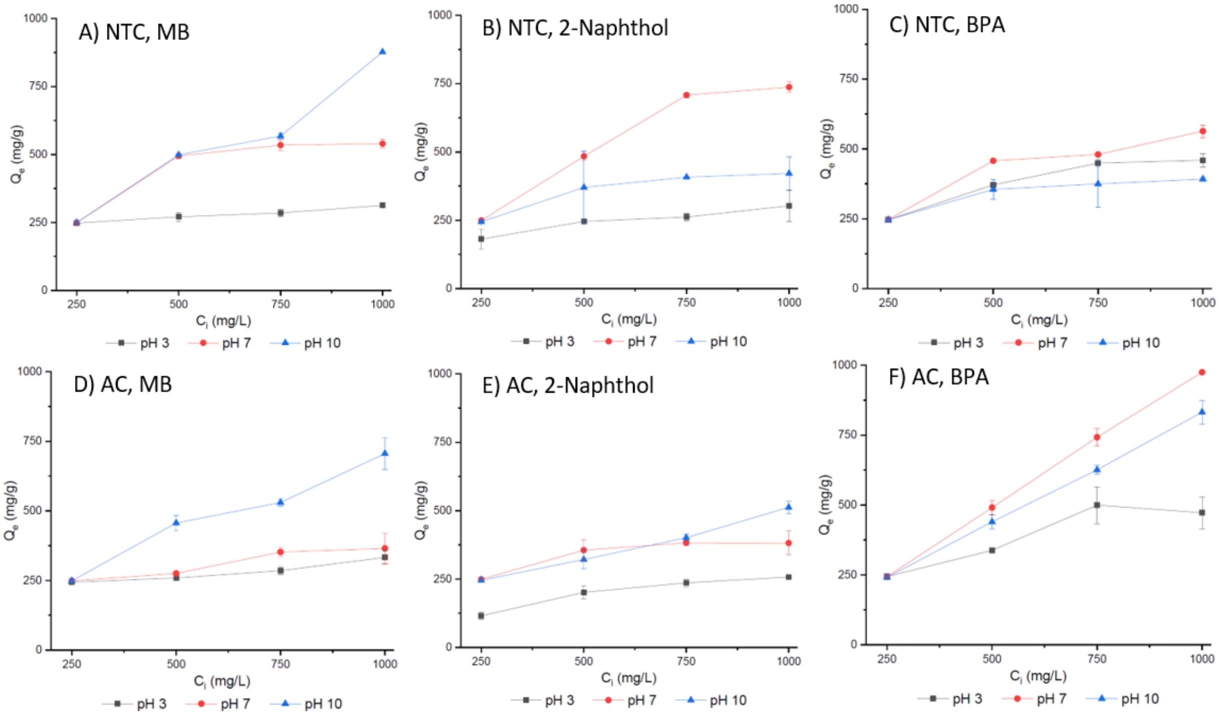

Figure 3.6: Adsorption capacity studies for NTC and AC against MB, 2-naphtol and BPA at varying concentrations (250, 500, 750 and 1000 ppm) and pH (pH of 3, 7 and 10).

Adsorption capacities for a commercially available AC were also studied under these conditions and can be seen in Figure 3.6D-F. Adsorption of MB by AC follows a similar trend as with NTC, with the lowest adsorption happening at acidic pH (332 mg/g). Under neutral conditions, adsorption is slightly increased (365 mg/g), while at basic pH we observe the highest adsorption capacity of MB onto AC (705 mg/g). Adsorption of 2-naphthol also has the lowest Q_e under acidic conditions (257 mg/g), with a higher adsorption capacity at neutral pH (382 mg/g) and the highest Q_e present under basic conditions (512 mg/g). The highest adsorption capacity for BPA happens under neutral pH (974 mg/g), much like with NTC. Basic conditions show a slight decrease in the adsorption capacity of BPA (831 mg/g) while acidic conditions have a drastic effect in the adsorption capacity (499 mg/g).

It should be noted that under acidic conditions, adsorption of all three contaminants by both NTC and AC is the lowest, indicating that electrostatic repulsion between the adsorbates is too large to be overcome by adsorbate/adsorbent interactions. At pH 10, however, BPA adsorption by AC is quite higher than by NTC, indicating the presence of possible groups in AC which can interact electrostatically with the negatively charged BPA molecules; this group appears to be absent in NTC. Adsorption of MB and 2-naphthol by both NTC and AC is relatively similar, indicating a larger pH effect on BPA than either of the other two contaminants, which in turn increased its adsorption onto AC. Of greater interest to us are the adsorption capacities under neutral conditions, for which NTC had significantly higher adsorption towards MB and 2-naphthol than AC. This indicates that our material has a large adsorption potential towards neutral and aromatic organic molecules due to its large surface area and sp^2-hybridized carbon composition.

3.3.5.2 Adsorption Isotherms

The Langmuir and Freundlich isotherms of NTC based on the previous adsorption capacity experiments can be seen in Figure 3.7, with Table 3.1 summarizing the adjusted R^2 value for each. We can see good correlation by the Langmuir isotherm for methylene blue and bisphenol-A at all pH levels, with R^2 values ranging from 0.91384 to 0.99998. Freundlich values for methylene blue were much lower (0.65518 at pH 3, 0.49276 at pH 7 and 0.33843 at pH 10), indicating that the adsorption of methylene blue by our adsorbent more closely resembles a single layer, Langmuir-type adsorption pattern at all three pH ranges. Interestingly, adsorption of 2-naphthol onto our adsorbent more closely resembles a Freundlich adsorption pattern ($R^2 = 0.96328$) than a Langmuir pattern ($R^2 = 0.62587$) at pH 3, while at pH 7 and pH 10 the R^2 values for Langmuir (0.99895 and 0.9983, respectively) are closer to 1 than those for Freundlich (0.89125 and 0.9991, respectively). Adsorption of BPA shows higher coefficient of determination for the Langmuir isotherm over the Freundlich isotherm at pH 3 and pH 7. At a pH of 10, both the Langmuir and Freundlich isotherms show a good fit for the adsorption of BPA, with the Freundlich isotherm fit being slightly higher than Langmuir.

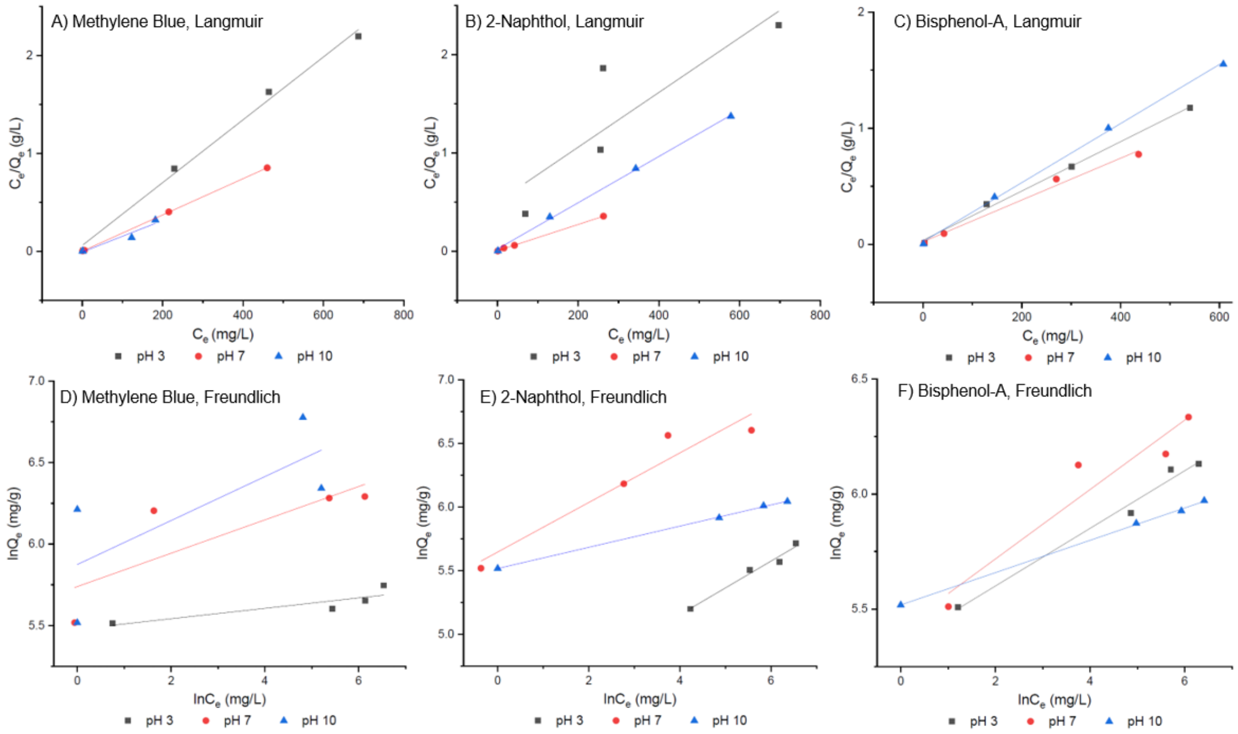

Figure 3.7: Langmuir and Freundlich adsorption isotherms for NTC against methylene blue, 2-Naphthol and bisphenol-A.

Table 3.1: Summary of Langmuir and Freundlich R^2 values for methylene blue, 2-naphthol and bisphenol-A adsorptions by NTC at pH 3, pH 7 and pH 10.

	Methylene Blue		2-Naphthol		Bisphenol-A	
	Langmuir	Freundlich	Langmuir	Freundlich	Langmuir	Freundlich
pH 3	0.99068	0.65518	0.62587	0.96328	0.99521	0.97787
pH 7	0.99998	0.49276	0.99895	0.89125	0.98402	0.87973
pH 10	0.91384	0.33843	0.9983	0.9991	0.99822	0.99889

Experimental and calculated adsorption maxima (Q_{max}) values can be seen in Table 3.2. With the exception of methylene blue at pH 10, we observe good correlation between experimental and calculated Q_{max} values. The intensity of adsorption (1/n) values for all adsorbates were calculated from the slope of each Freundlich isotherm. Intensity of adsorption values of 1/n under 0 (negative) are considered irreversible adsorptions. Values of 1/n between 0 and 1 are considered desirable, and values of 1/n greater than 1 are considered undesirable. From Table 3 we can see that all intensity of adsorption values are between 0 and 1, indicating desirable adsorption conditions of the adsorbates onto NTC at all three pH. The Langmuir (K_L) and Freundlich (K_F) constants, as well as the dimensionless equilibrium parameter R_L, were calculated and their values summarized in Table 3. Calculations for K_L and R_L can be found in Equations 6 and 7, respectively.

$$K_L = \frac{1}{Q_{max}\, y_{intercept}} \qquad \text{Equation 6}$$

$$R_L = \frac{1}{1+K_L C_i} \qquad \text{Equation 7}$$

Where Q_{max} is the maximum calculated adsorption, $y_{intercept}$ is the y-intercept of the C_e/Q_e vs C_e Langmuir plot for the given adsorbent and pH, K_L is the Langmuir constant, and C_i is the initial concentration of the adsorbate solution. R_L values are used to describe a favorable ($0 < R_L < 1$), unfavorable ($R_L > 1$), irreversible ($R_L = 0$) or linear ($R_L = 1$) adsorption. From Table 3.2 we can see that most R_L values fall between 0 and 1, indicating a favorable adsorption onto our adsorbent. Interestingly, there are several R_L values which are very close to 0 which would describe an irreversible adsorption; this could be attributed to very strong adsorbate/adsorbent interactions under these conditions.

Table 3.2: NTC Q_{max} values calculated (calc.) from Langmuir isotherm and found experimentally (exp.), as well as the intensity of adsorption (1/n), Langmuir constant (K_L), the equilibrium parameter R_L and the Freundlich constant K_F for methylene blue, 2-naphthol and bisphenol-A at pH 3, 7 and 10.

		Q_{max} (mg/g)					
	pH	exp.	calc.	1/n	K_L	R_L	K_F
Methylene Blue	3	313.1	311.5	0.03194	0.05298	0.01852	5.478
	7	539.9	540.5	0.1023	0.8894	0.001123	5.739
	10	877.2	621.1	0.1348	-0.2326	0.004320	5.875
2-Naphthol	3	303.1	359.7	0.2104	0.005536	0.1529	4.312
	7	737.2	746.3	0.1947	0.2388	0.004169	5.646
	10	421.6	425.5	0.08324	0.1010	0.009801	5.517
Bisphenol-A	3	459.5	469.5	0.1252	0.06190	0.01589	5.350
	7	563.4	555.6	0.1508	0.08185	0.01207	5.416
	10	392.0	393.7	0.07022	0.1101	0.008993	5.518

3.3.5.3 Kinetic Studies

The adsorption kinetics of NTC and AC towards all three contaminants were compared and can be seen in Figure 3.8. While the control demonstrated a higher Q_t within immediate contact for both methylene blue and 2-naphthol, NTC surpassed this Q_t within one minute (MB) and thirty seconds (2-naphthol), respectively. NTC also retained higher adsorption properties than AC up to thirty minutes after initial contact for both MB and 2-naphthol. Our material demonstrates a higher Q_t for BPA within immediate contact and retains it throughout the four-hour test time.

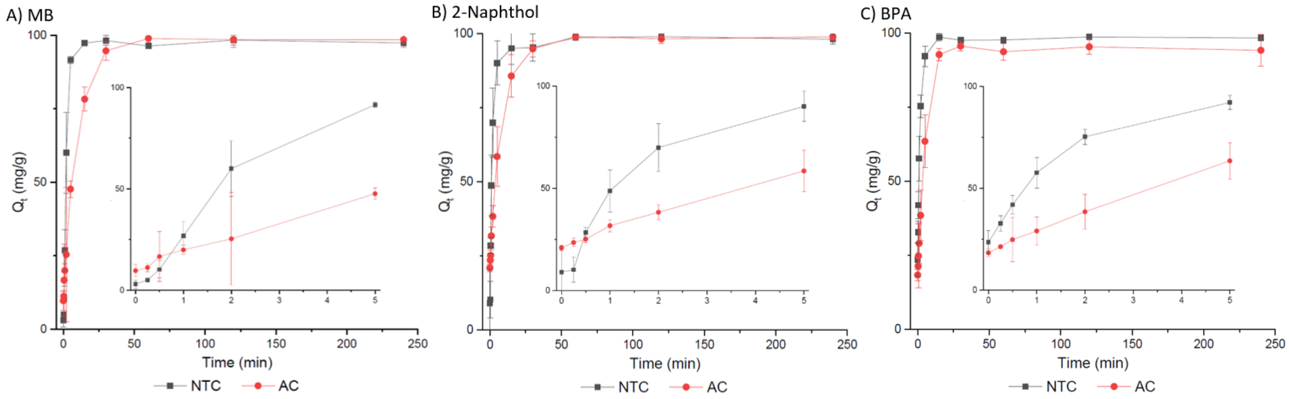

Figure 3.8: Kinetic studies of NTC (black squares) and AC (red dots) against A) methylene blue, B) 2-Naphthol and C) Bisphenol-A up to four hours of contact time. Insets are adsorptions up to five minutes contact time.

3.3.5.4 Kinetic Models

Data acquired through the kinetic adsorption experiments was plotted against the pseudo-first order, pseudo-second order and intra-particle diffusion models summarized in Figure 3.9, with the adjusted R^2 values summarized in Table 3.3. The data is better represented by the pseudo-second order kinetic model for all three contaminants, with R^2 values nearing 1. Intraparticle diffusion kinetic model shows R^2 values ranging from 0.42 – 0.44, and pseudo-first order kinetic model demonstrates the lowest R^2 values, ranging from 0.27 to 0.41. Intraparticle diffusion models for all three contaminants appear to show two adsorption phases, with the first phase ($t^{0.5}$ between 0 and 2.236) demonstrating a steep positive slope, followed by a near-plateau at $t^{0.5}$ between 2.236 and 15.49. This is indicative of more than one process governing the adsorption process of the contaminants onto our adsorbent.

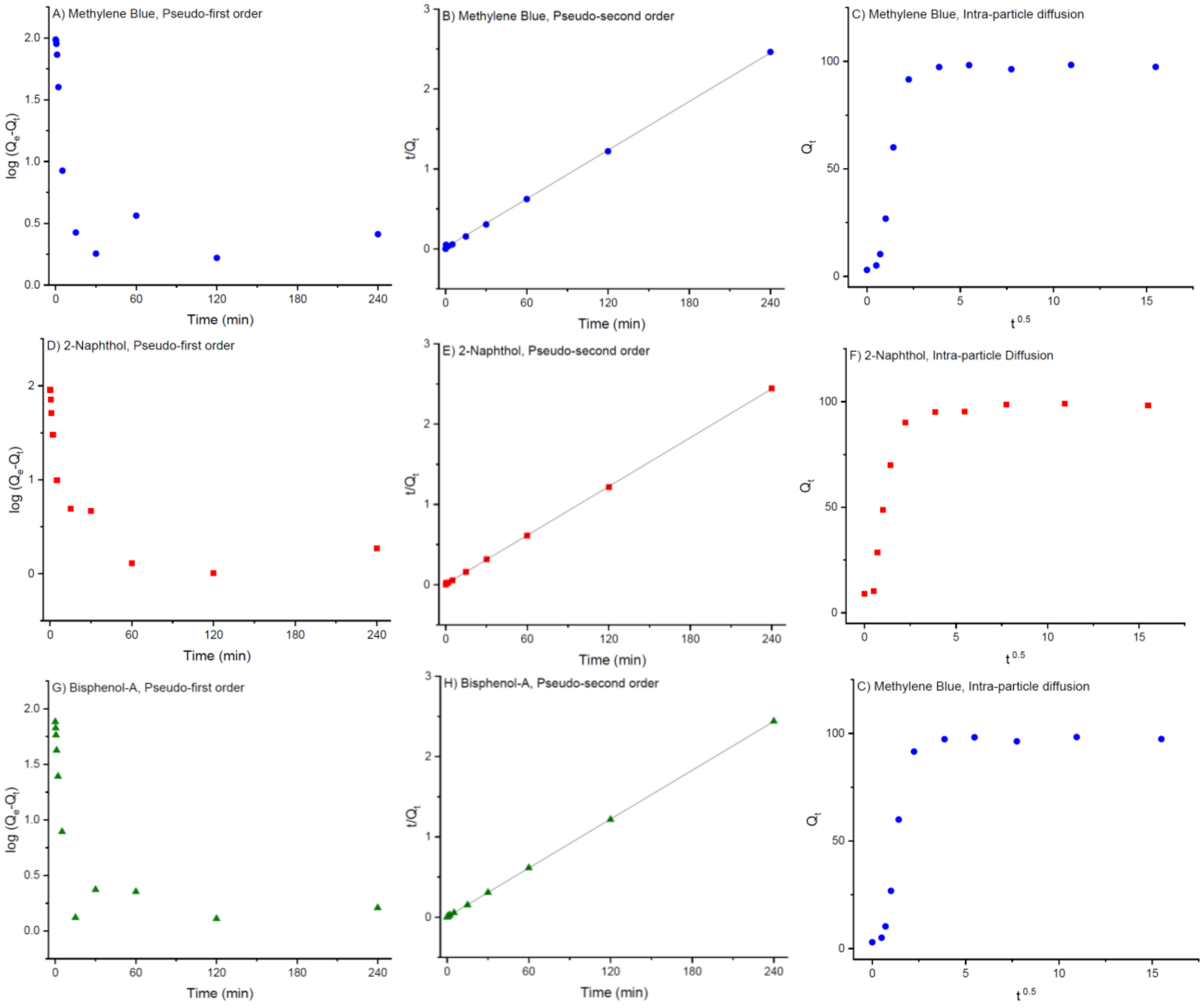

Figure 3.9: Pseudo-first order, pseudo-second order and intra-particle diffusion models for NTC against methylene blue (A-C), 2-Naphthol (D-F), and bisphenol-A (G-I).

Table 3.3: Pseudo-first order, pseudo-second order and intraparticle diffusion R^2 values for methylene blue, 2-naphthol and bisphenol-A.

	Pseudo-first order	Pseudo-second order	Intraparticle diffusion
Methylene Blue	0.27926	0.99943	0.44591
2-Naphthol	0.41101	0.9999	0.43844
Bisphenol-A	0.31301	0.99998	0.42816

3.3.5.5 Continuous Flow Adsorption Study

To simulate water purification in real-world filtration systems, a continuous-flow purification system was tested (Figure 3.10). Briefly, 1 g of NTC was mixed with 100 g of sand and packed into a 250 mL glass column. A 20 ppm MB solution made in tap water was passed through this packed column via gravity filtration with a constant flow rate of 4.5 mL/min. The column was kept under constant flow until traces of MB were observed in the filtrate. Flow adsorption proved 100% efficient up to 11.5 L, with the breakthrough point at 12 L. The flow experiment was continued up to 15 L, at which point the adsorption efficiency had decreased to 72%. Under these experimental conditions, this material has the potential to purify 230 L of 1 ppm MB-contaminated water with 100% removal efficiency.

A paper published by Bukallah et al. studied the adsorption of methylene blue onto sand collected from local sand dunes in the southeastern region of United Arab Emirates.[166] Based on their optimized results, they found that optimal adsorption of methylene blue happened with 0.1 g of sand, which was able to remove 92% of methylene blue from 5 mL of a 1.8×10^{-5} M solution. This molar concentration equates to a 5.7 ppb MB solution. If we were to scale their results to use 100 g of sand, as in our experiment, we could expect similar adsorption from 5 mL of a 5.7 ppm solution. Given that we observed complete MB adsorption of a 20 ppm solution up to 11.5 L, we believe sand played a very minor roll in the results of this flow adsorption study.

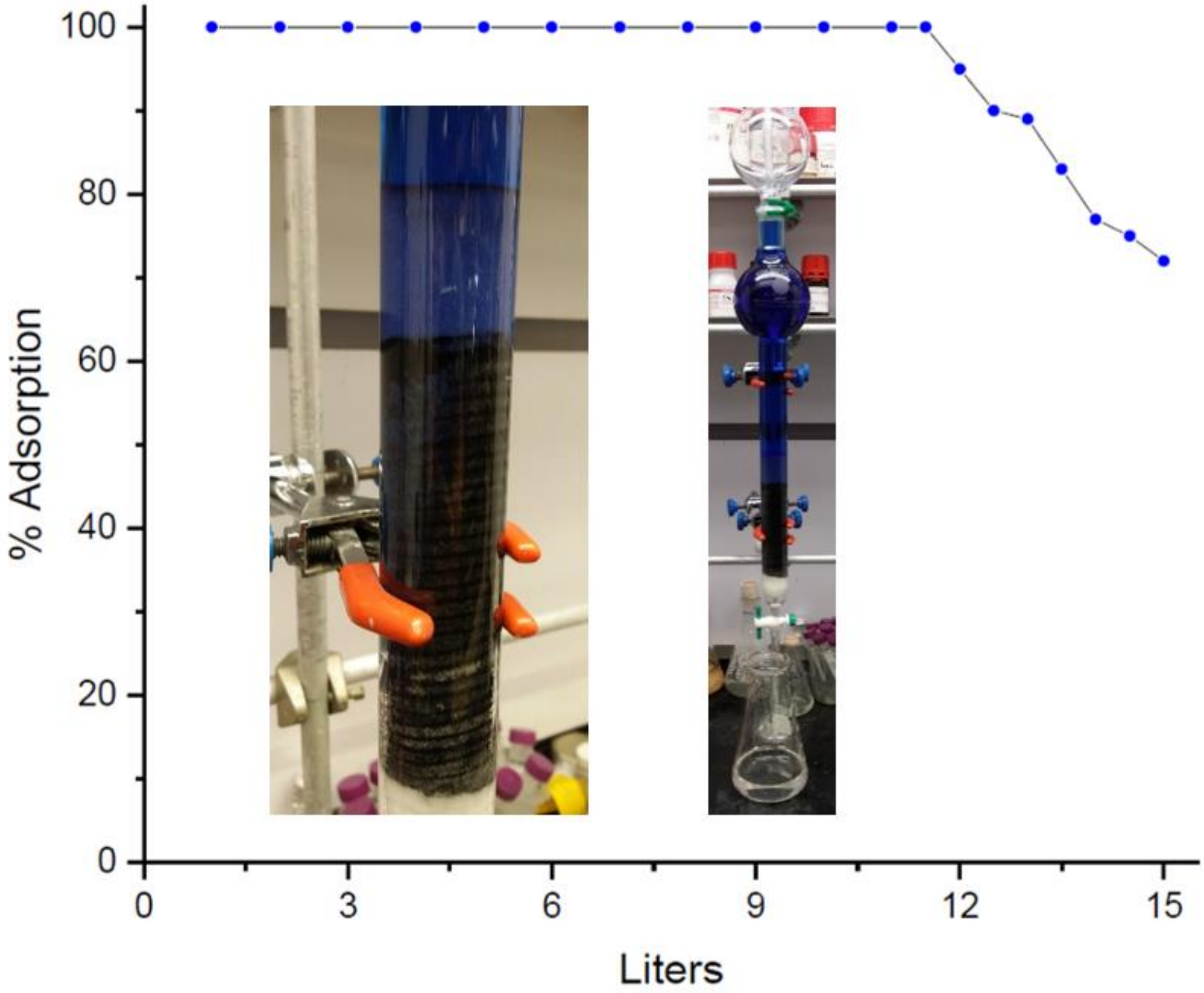

Figure 3.10: Percent adsorption vs number of liters filtered during flow adsorption of MB (20 ppm, tap water) by NTC. Insets show column packing, as well as contaminated water (input) and purified water (output).

3.4 COMPARISON WITH SIMILAR ADSORBENTS

Adsorption capacities and surface area of our material has been compared to similar adsorbents[167-179] and can be seen in Table 3.5. The surface area of NTC, while not the highest, is at the higher end of the spectrum, nearly matching those of carbonized metal-organic frameworks (MOFs) which are known to have large surface areas, and more than doubling that of sulfonated graphene nanosheets. Adsorption capacities for our material at near-neutral pH either surpasses or is on-par with other materials. For methylene blue, adsorption capacity of NTC is higher than other biomass-derived adsorbents. Adsorption of 2-naphthol is much higher than that of many organoclays, and more than doubles the Q_e reported for bamboo hydrochars and even sulfonated graphene sheets. Bisphenol-A adsorption, while not the highest, is still on-par with materials such as carbonized MOFs and activated tire adsorbents.

Table 3.5: Comparison of surface area and adsorption capacities of various adsorbents for the removal of MB, 2-Naphthol and BPA at near-neutral pH.

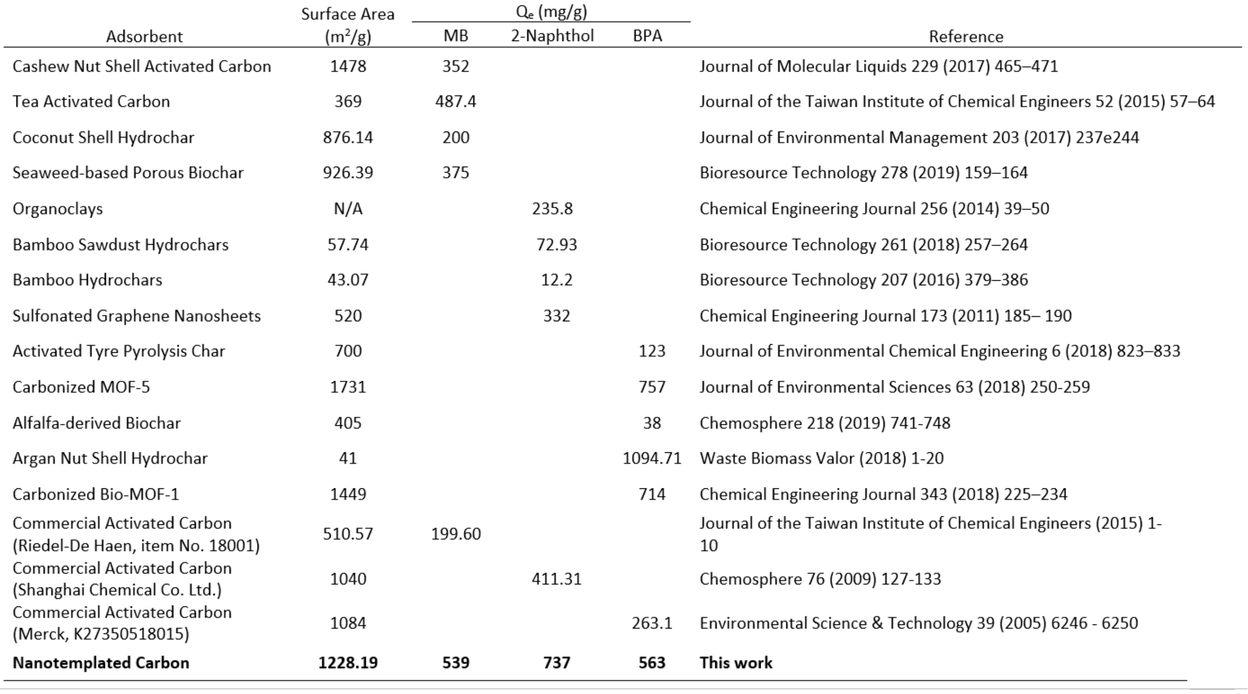

Adsorbent	Surface Area (m^2/g)	Q_e (mg/g) MB	Q_e (mg/g) 2-Naphthol	Q_e (mg/g) BPA	Reference
Cashew Nut Shell Activated Carbon	1478	352			Journal of Molecular Liquids 229 (2017) 465–471
Tea Activated Carbon	369	487.4			Journal of the Taiwan Institute of Chemical Engineers 52 (2015) 57–64
Coconut Shell Hydrochar	876.14	200			Journal of Environmental Management 203 (2017) 237e244
Seaweed-based Porous Biochar	926.39	375			Bioresource Technology 278 (2019) 159–164
Organoclays	N/A		235.8		Chemical Engineering Journal 256 (2014) 39–50
Bamboo Sawdust Hydrochars	57.74		72.93		Bioresource Technology 261 (2018) 257–264
Bamboo Hydrochars	43.07		12.2		Bioresource Technology 207 (2016) 379–386
Sulfonated Graphene Nanosheets	520		332		Chemical Engineering Journal 173 (2011) 185– 190
Activated Tyre Pyrolysis Char	700			123	Journal of Environmental Chemical Engineering 6 (2018) 823–833
Carbonized MOF-5	1731			757	Journal of Environmental Sciences 63 (2018) 250-259
Alfalfa-derived Biochar	405			38	Chemosphere 218 (2019) 741-748
Argan Nut Shell Hydrochar	41			1094.71	Waste Biomass Valor (2018) 1-20
Carbonized Bio-MOF-1	1449			714	Chemical Engineering Journal 343 (2018) 225–234
Commercial Activated Carbon (Riedel-De Haen, item No. 18001)	510.57	199.60			Journal of the Taiwan Institute of Chemical Engineers (2015) 1-10
Commercial Activated Carbon (Shanghai Chemical Co. Ltd.)	1040		411.31		Chemosphere 76 (2009) 127-133
Commercial Activated Carbon (Merck, K27350518015)	1084			263.1	Environmental Science & Technology 39 (2005) 6246 - 6250
Nanotemplated Carbon	**1228.19**	**539**	**737**	**563**	**This work**

3.5 CONCLUSION

In summary, we have developed a carbon adsorbent from the carbonization of glucose at 1000 °C under Argon conditions in the presence of ZnO nanoparticles. Under these conditions Zn(II) is reduced to Zn(0) and sublimed, yielding a nanotemplated porous adsorbent material with surface area of 1228.19 m^2/g and average pore diameter of 14.77 nm. From EDX-S we observe an elemental composition of 90.2% carbon and 8.2% oxygen, indicating an adsorbent with high carbon-content composed of sp^2 hybridized carbons and honeycomb structures, as evidenced by XRD analysis. Its adsorption capacity against methylene blue, 2-naphthol and bisphenol-A were found both experimentally and calculated by the Langmuir isotherm model at pH 3, pH 7 and pH 10. Experimental Q_{max} values for methylene blue, 2-naphthol and bisphenol-A at pH 7 are 539 mg/g, 737 mg/g and 563 mg/g, respectively. Adsorption kinetic experiments were performed against the three contaminants at pH 7 and the data modeled using the pseudo-first order, pseudo-second order and intraparticle diffusion kinetic models. In conclusion, carbonization of glucose under inert atmosphere in the presence of ZnO NPs has yielded a high-surface area bioderived adsorbent with excellent adsorption capacities and fast kinetics towards methylene blue, 2-naphthol and bisphenol-A. We believe this method of generating biochars from inexpensive starting materials can have a huge impact on the synthesis of adsorbents for water remediation of organic pollutants in the future.

Chapter 4: Iron Oxide Functionalized Adsorbent for the Removal of Inorganic Contaminants from Water

4.1 INTRODUCTION

Arsenic is an inorganic contaminant which can be found in water, soil, food and even air for those exposed to it through their occupation.[180] Constant exposure to arsenic can lead to a variety of deleterious effects, including vascular diseases, reproductive toxicity and neurological effects.[181] Arsenic exposure has been linked to cancers of the skin, lung, bladder, liver, and prostate [182-186]. Due to its deleterious effects in humans, the World Health Organization (WHO) has set the safe levels of arsenic exposure to 10 parts per billion.[187] However, it is estimated that over 100 million people worldwide are exposed to As levels which are considered carcinogenic, mostly via drinking contaminated groundwater.[181]

Many methods have been proposed for the remediation of arsenic-contaminated water. The most common technologies include coagulation/filtration, membrane separation, ion exchange, and adsorption.[188-193] From the aforementioned methods, adsorption has a select few benefits over the rest, including ease of operation, relatively lower operation cost, and no need for added reagents.[194] We have chosen to use our method for developing a high surface area adsorbent as a base for further functionalization with iron oxide nanoparticles. There are four main reasons why we chose to use this approach for the remediation of arsenic from water. The first is our proven method to generate a high surface area adsorbent; in theory, higher surface area directly correlates to higher sites for the adsorption of arsenic. Second is the proven efficacy of iron oxide nanoparticles towards the removal of arsenic from water; both Fe_2O_3 and Fe_3O_4 have proven to be potent adsorbents towards arsenic.[195-200] Third, it has been shown that iron oxide can be formed in-situ via thermal means.[201,202] Therefore, our adsorbent material containing iron oxide can be made in a single synthetic step, allowing for easier replication of our methodology. And lastly, the presence of magnetic iron oxide in the material imbues it with magnetic properties which can be exploited in a filtration system, helping to prevent of minimize leaching of the nanoparticles onto the clean water.

This material was also tested for its adsorption capabilities against barium and lead, with surprisingly good results. Due to the carbon composition of this material, its adsorption against methylene blue as a proxy of other organic pollutants was also explored. More interestingly, due to the availability of iron in our material, its capacity to perform as a Fenton catalyst was briefly explored, with the results outlined in section 4.3.4.1.

4.2 MATERIALS AND METHODS

4.2.1 Preparation of Material

In a typical experiment, D(+)-glucose (4g, 22.2 mmol), $FeCl_3•6H_2O$ (1.08 g, 4 mmol) and $FeSO_4•7H_2O$ (0.56g, 2 mmol) were dissolved in 50 mL RO water. To this solution, 2g of ZnO NPs (<35 nm particle size) were added and the suspension ultrasonicated for 30 minutes, followed by stirring for a further 30 minutes to promote homogeneity. This suspension was then concentrated under reduced pressure using a rotary evaporator, mixed further using mortar and pestle, and left to dry under reduced pressure via vacuum pump overnight.

The mixture was then weighed and transferred to a quartz crucible and placed in a sealed furnace. The furnace was argon-flushed for 30 minutes, followed by carbonization for two hours at 1000 ^{o}C with a ramp speed of 10 ^{o}C/min under constant argon flow. Carbonized 6.97 g, recovered 0.403 g.

4.2.2 Adsorption Capacity Studies

For the adsorption of heavy metals, 100 ppm stock solutions were made for $Pb(NO_3)_2$ (16.13 mg), $BaCl_2•2H_2O$ (17.85 mg), $NaAsO_2$ (17.54 mg) and $Na_2HAsO_4•7H_2O$ (41.66 mg) in 100 mL RO water, respectively. The mixtures were ultrasonicated to ensure full dissolution. These 100 ppm stock solutions were used to make 10 ppm, 1 ppm and 0.1 ppm contaminant solutions used for the study. Adsorption capacity studies were done in triplicate in 20 mL vials using 10 mg adsorbent and 10 mL of contaminant solution under constant stirring for three days to allow for adsorption equilibrium. At this point the experiments were centrifuged, 7.5 mL of each sample transferred to a clean centrifuge tube, and 2.5 mL of a 12% nitric acid solution was added to acidify each solution for ICP-OES analysis.

Methylene blue adsorption and Fenton reduction studies were performed using 50 mg of adsorbent and 50 mL of a 50 ppm methylene blue solution in RO water. To each, varying amounts of a 30% hydrogen peroxide solution (0 mL, 0.5 mL, 1 mL, and 2.5 mL respectively) was added. The reactions were stirred continuously at 3500 rpm and 1 mL aliquots were taken at 1h, 2h, 3h, 4h and 24h. Sample aliquots were diluted by a factor of 1/5 and analyzed by UV-VIS spectrophotometry.

4.2.3 Characterization

Carbonization was performed using a GSL-1100X from MTI Corporation. The X-ray diffraction analysis of the carbon material and the embedded nanoparticles was performed on a Panalytical Empyrean 2 diffractometer (Cu anode, Kα radiation, $\lambda = 1.54$ nm) with a scan rate of 1.7 deg/min. A Hitachi S-4800 instrument was used for SEM as well as EDS images. Samples for EDS were placed as powders in 12 mm diameter carbon adhesive tabs. UV-Vis adsorption measurements were taken through a 10.00 mm quarts cuvette using a NU-T6PC instrument purchased from Zhengzhou Nanbei Instrument Equipment corporation. Infrared spectroscopy analysis was done on a Nicolet iS5 FTIR with ATR module using a scanning range of 650-4000 cm^{-1}. ICP-OES measurements were performed on a Perkin Elmer OPTIMA 4300 DV ICP-OES.

4.3 RESULTS AND DISCUSSION

4.3.1 Electron Microscopy

Scanning electron microscopy images for this material can be seen in Figure 4.1. Magnification to 1.00 mm shows a rugged, highly porous material of amorphous distribution. Further magnification to 50 um shows small areas with higher electron conductivity than its surroundings, as indicated by brighter shading than its darker, less conductive carbon bulk material. These areas of higher electron conductivity are speculated to be iron oxide nanoparticles formed during the carbonization process.

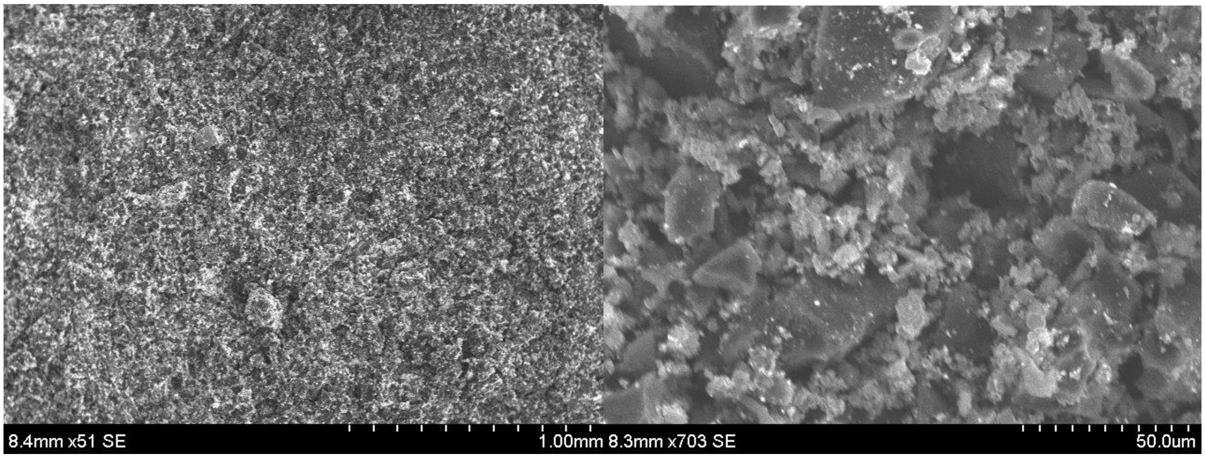

Figure 4.1: Scanning electron microscopy images of iron oxide-functionalized adsorbent.

Elemental analysis of this iron oxide-containing adsorbent can be seen in Figure 4.2. As expected, the material is mainly composed of carbon, oxygen, and iron. Carbon content is predominant after carbonization, making up 49.75% (by weight) of the material. This falls in line with what we observed during the synthesis of NTC (Chapter 3), where carbon remained as the predominant atom present in the material after carbonization at 1000 ^{o}C. In the same manner, oxygen content decreased significantly, making up only 7.11% of the material by weight. This once again follows both our previous work and literature reports, as carbonization of carbohydrates at elevated temperatures results in a drastic decrease of oxygen content due to the evolution of small organic molecules containing oxygen. Iron content is also relatively high (38.24% weight), showing the incorporation of iron onto the material. Interestingly, sulfur content is also observed in our material in a significant quantity, despite continuous washing of the material after carbonization. This seems to suggest that the sulfur content comes not from physical adsorption of sulfur salts onto the adsorbent, but as chemical incorporation of sulfur into the material, possibly as thioethers, thioesters, or sulfuric/sulfonic acids. Atomic percentages can be seen in Table 4.1.

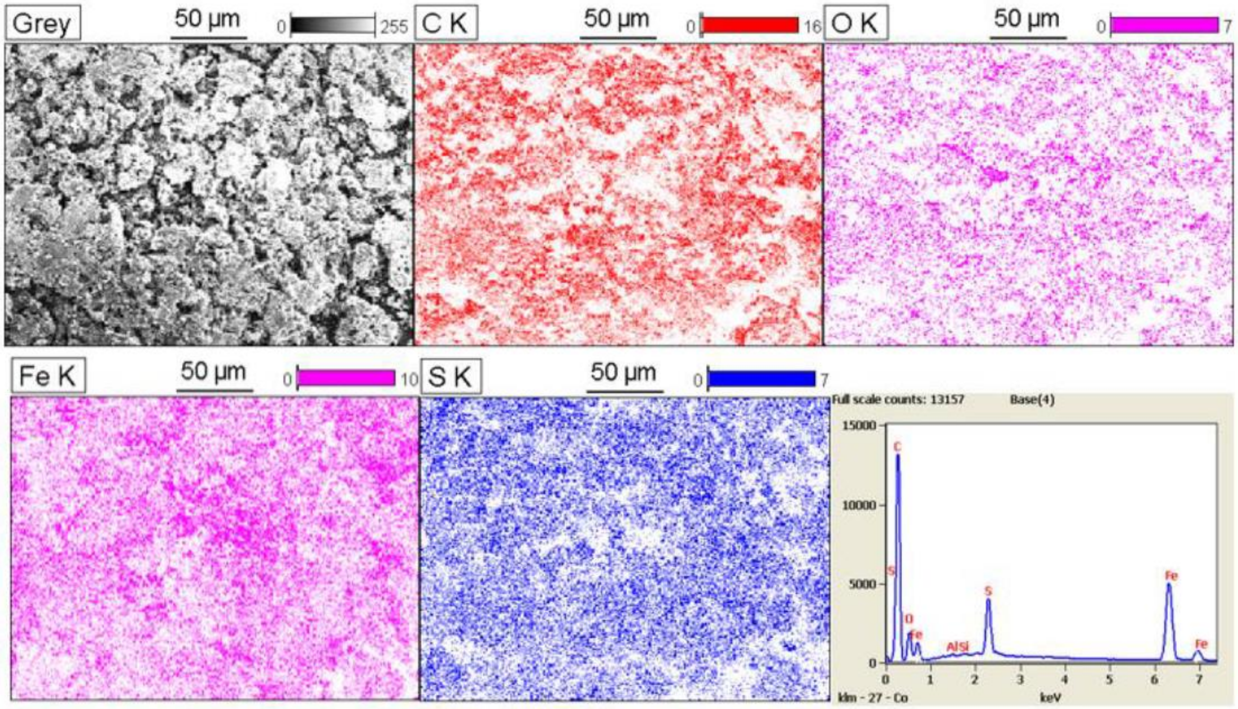

Figure 4.2: Elemental mapping of iron oxide-functionalized adsorbent.

Table 4.1: Summary of elemental composition of iron oxide-containing adsorbent by elemental weight and atomic percentage.

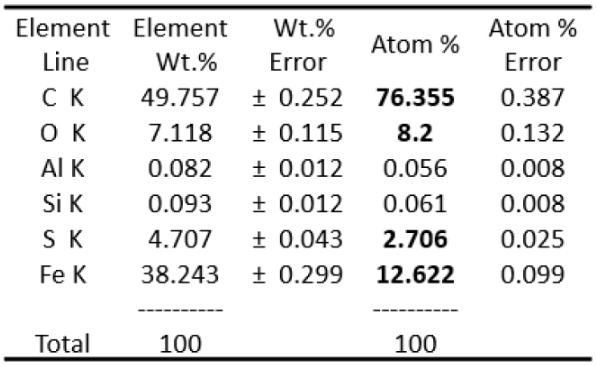

Element Line	Element Wt.%	Wt.% Error	Atom %	Atom % Error
C K	49.757	± 0.252	**76.355**	0.387
O K	7.118	± 0.115	**8.2**	0.132
Al K	0.082	± 0.012	0.056	0.008
Si K	0.093	± 0.012	0.061	0.008
S K	4.707	± 0.043	**2.706**	0.025
Fe K	38.243	± 0.299	**12.622**	0.099
	----------		----------	
Total	100		100	

4.3.2 Infrared Spectroscopy

Fourier transform infrared spectroscopy analysis of our material can be seen in Figure 4.3 below. Analysis of the material (Before Correction, black) was unsatisfactory, yielding mostly a flatline with small fluctuations centered around 2366, 2336 and 1017 cm^{-1}. A second FTIR reading was done after first baselining the instrument with the NTC synthesized in Chapter 3 of this dissertation. As the two materials share a similar carbon backbone (glucose carbonized at 1000 ^{o}C for two hours), performing a baseline with NTC should in theory remove the C-H, C-C and C-O stretching and bending frequencies from the IR analysis, allowing for frequencies belonging to iron complexes to be highlighted. Analysis after this baseline correction (After Correction, red) shows a distinct broad absorption peak from 1017 cm^{-1} to 1308 cm^{-1}, with the lowest peak centered at 1071 cm^{-1}. Some irregularities are also observed in the ranges of 1377 – 1971 cm^{-1} and 3558 – 3944 cm^{-1}. Literature reports are conflicting, although most seem to agree that absorption frequencies from Fe-O fall in the range of 450 – 650 cm^{-1}.[203-206] While we do observe small fluctuations at 665 cm^{-1} and 693 cm^{-1}, these are inconclusive. Due to instrument limitations, absorption range was limited above 550 cm^{-1}. The broad signal observed from 1017 cm^{-1} to 1308 cm^{-1} is likely due to C-O stretching, although sulfoxide S=O stretching signals do fall in the range of 1030 cm^{-1} – 1070 cm^{-1}. This would corroborate our theory that sulfur has been incorporated into our material, possibly as a sulfoxide moiety.

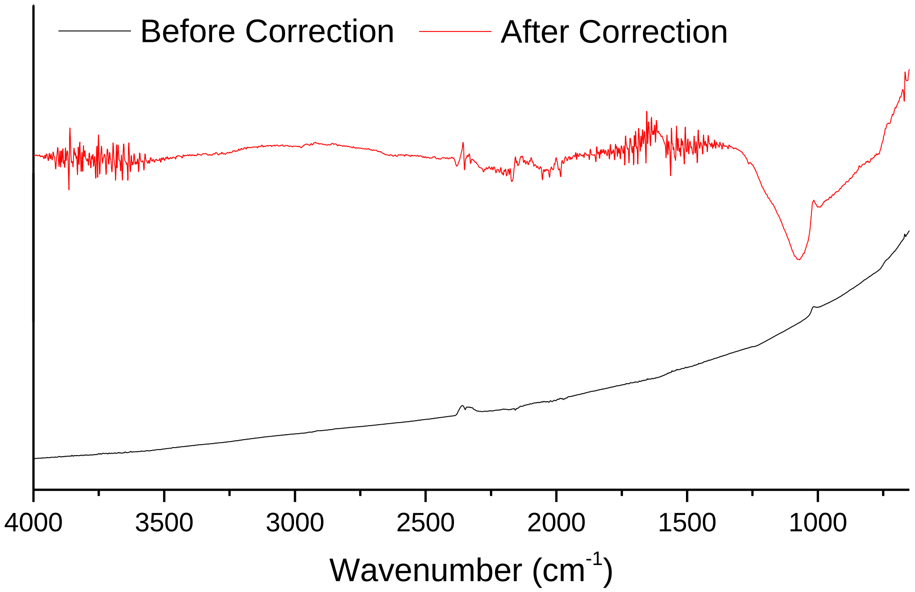

Figure 4.3: Infrared Spectrum of iron oxide-containing adsorbent before (black) and after (red) baseline correction.

4.3.3 X-ray Diffraction

X-ray diffraction analysis of our material can be seen in Figure 4.4. Our iron oxide-functionalized adsorbent shows distinct peaks at 2θ angles 30.00, 33.42, 35.35, 42.99, 52.89, 56.92 and 62.45, with a few smaller peaks appearing at 70.73, 74.11 and 86.79. In the literature, reports for magnetite (Fe_3O_4) show diffraction patterns at or near 2θ angles of 30, 35.7, 43.4, 53.7, 57.5, and 63.00 for phases (220), (311), (400), (422), (511) and (440), respectively, which are in accordance with JCPDS No. 07-0322.[207] Hematite (Fe_2O_3) on the other hand shows diffraction peaks at or around 2θ angles of 24, 33, 36, 41, 49, 54, 58, 62, 64, and 72 degrees, as per JCPDS No. 33-0664.[203] Goethite (FeO-OH) demonstrates characteristic diffraction peaks at 2θ angles 17.8, 21.3, 33.3, 34.7, 36.1, 36.7, 41.2, 47.3, 53.3, 55.3, 59.04, 63.9 and 69.0.[208] Based on this search the iron content of our material seems to be mostly composed of Fe_3O_4 nanoparticles, with nearly all of the characteristics phases of magnetite being at- or near what is reported for these nanoparticles. There also appear to be some overlap with hematite nanoparticles, mainly at 2θ angles 33.42, 35.35 and 62.45 of our material with those reported on the literature for our material. Not much overlap appears to be present between our material and goethite. Based on this, we believe the iron content of our material to be predominantly magnetite based, with some of the nanoparticles corresponding to hematite.

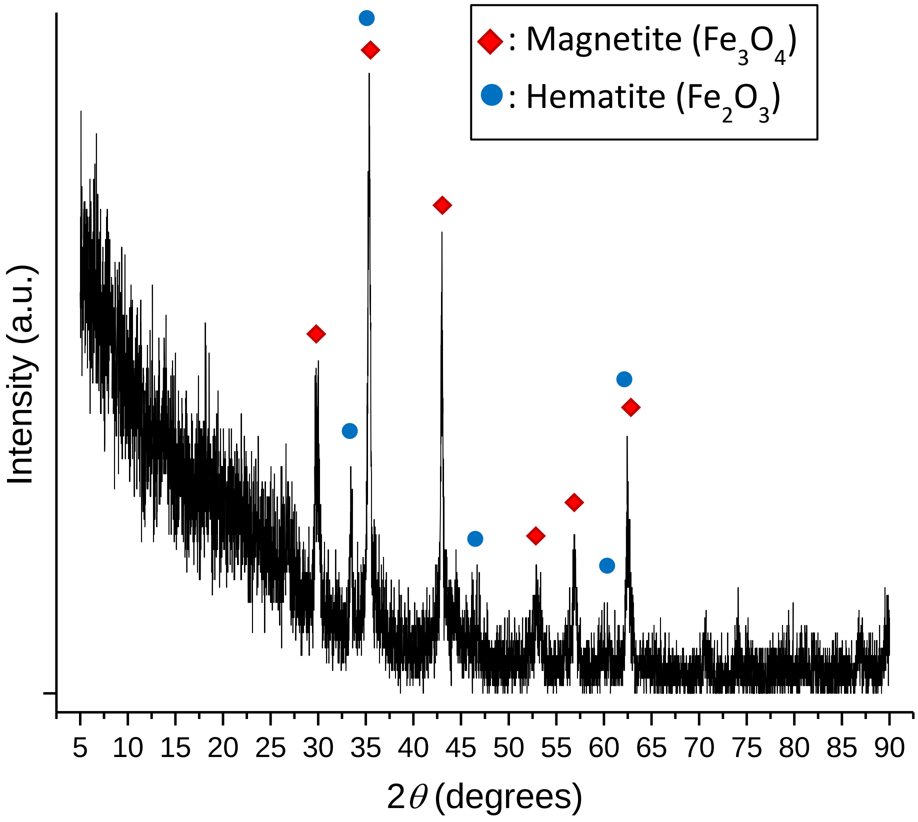

Figure 4.4: X-ray diffractogram of iron oxide-containing adsorbent.

4.3.4 Adsorption Studies

4.3.4.1 Adsorption Capacity Studies for Inorganic Contaminants

The adsorption capacity of this material against some major inorganic contaminants was explored, namely lead(IV), barium(II), arsenic(III) and arsenic(V). While the study was not exhaustive, three concentrations for each contaminant were still explored: 0.1, 1.0 and 10.0 ppm. A summary of the adsorption capacity and standard deviation of this material at each concentration can also be seen in Table 4.2. While maximum adsorption was achieved at concentrations 0.1 and 1 ppm against most contaminants, sub-maximum adsorption can be seen for all contaminants at a concentration of 10 ppm. This is in stark contrast to the adsorption capacities of adsorbent materials previously explored in this dissertation against organic contaminants, where we saw adsorption equilibriums as high as 737 mg/g. This could be the result of several factors, mainly, the porosity of this material is in question. Adsorption of this material against methylene blue was much lower when compared to NTC, as will be discussed further in this chapter. While electrochemical interactions between the carbon matrix, the iron oxide nanoparticles and the contaminant are possible, we believe a lack of porosity would better explain the substantial disparity in adsorption capacity. However, as mentioned in the introduction, the World Health Organization has set arsenic safe levels to 10 ppb, considerably lower than the adsorption capacity of our material against arsenic(III) and arsenic(V) (7.86 and 4.48 mg/g, respectively). While we did not test our material at 10 ppb, we did test it at 100 ppb (0.1 ppm in our data) and our material performed splendidly against both contaminants. The US Environmental Protection Agency similarly has set an action level for lead at 15 ppb, where sites producing higher lead levels must take action to remedy these concentrations from their drinking water.[209] Once again, our material performed well at a concentration of 100 ppb (0.1 ppm) against lead, with a maximum adsorption capacity of 5.58

mg/g. Adsorption of barium was much less exciting, achieving a maximum adsorption capacity of 2.34 mg/g at an initial concentration of 10 ppm barium. Barium toxicity levels are set to 0.5 mg/L for soluble barium compounds,[210] making our material still relevant as a possible remedy for the reduction of barium in contaminated water. It should be noted that while the adsorption capacity of this material against these heavy metals may seem low, it is on par to similar adsorbents currently being explored in the literature.

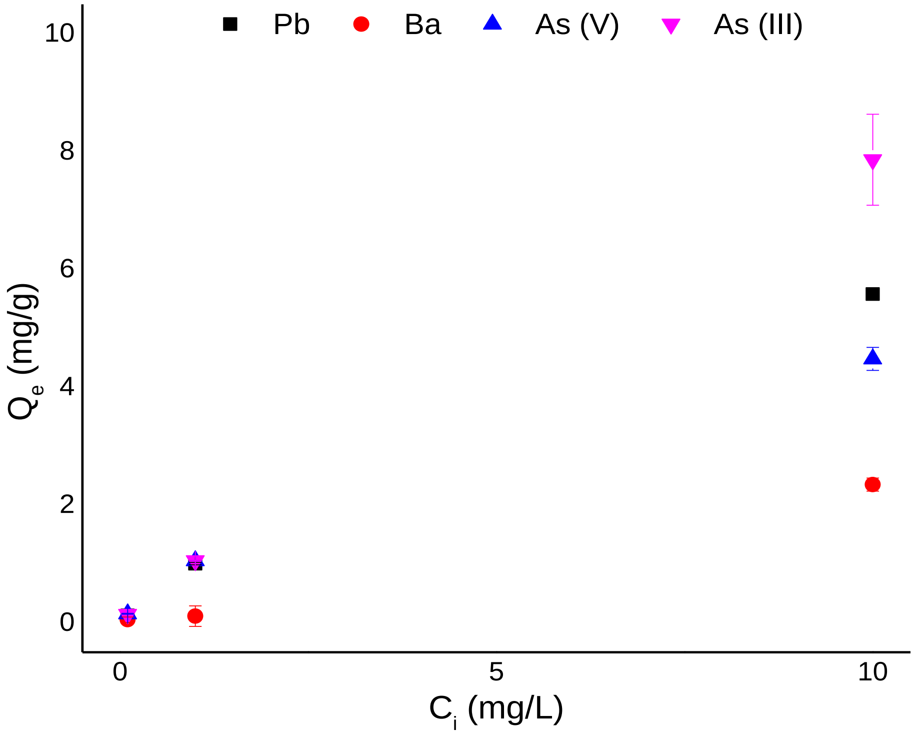

Figure 4.5: Adsorption capacity study against lead, barium, arsenic (III) and arsenic (V).

Table 4.2: Summary of adsorption capacities against lead, barium, arsenic (III) and arsenic (V).

C_i (ppm)	0.1		1		10	
	Q_e (mg/g)	St. Dev.	Q_e (mg/g)	St. Dev.	Q_e (mg/g)	St. Dev.
Lead	0.123751	0.000753	1.0035	0.019941	5.579612	0.00153
Barium	0.051666	0.047141	0.112938	0.173781	2.347239	0.111322
Arsenic (III)	0.142206	0.000385	1.054211	0.001545	7.861099	0.771299
Arsenic (V)	0.153341	0.007292	1.053994	0.001747	4.480343	0.194216

4.3.4.1 Fenton Reaction for the Degradation of Methylene Blue

The Fenton reaction was first introduced by Henry John Horstman Fenton in 1894 as a method of detection for tartaric acid by using iron sulfate and hydrogen peroxide as reactants, where he noticed a distinct violet coloration after the reaction.[211] While unbeknownst to him at the time, he speculated that this formation of color was possibly due to reducing properties of the solution.[212] It wasn't until much later that a mechanism for the formation of dihydroxymaleic acid from tartaric acid was proposed which involved the oxidation of iron(II) to iron(III), followed by the reduction of iron(III) to iron(II) by hydroxyl radicals which regenerates the iron catalyst (see Scheme 4.1).

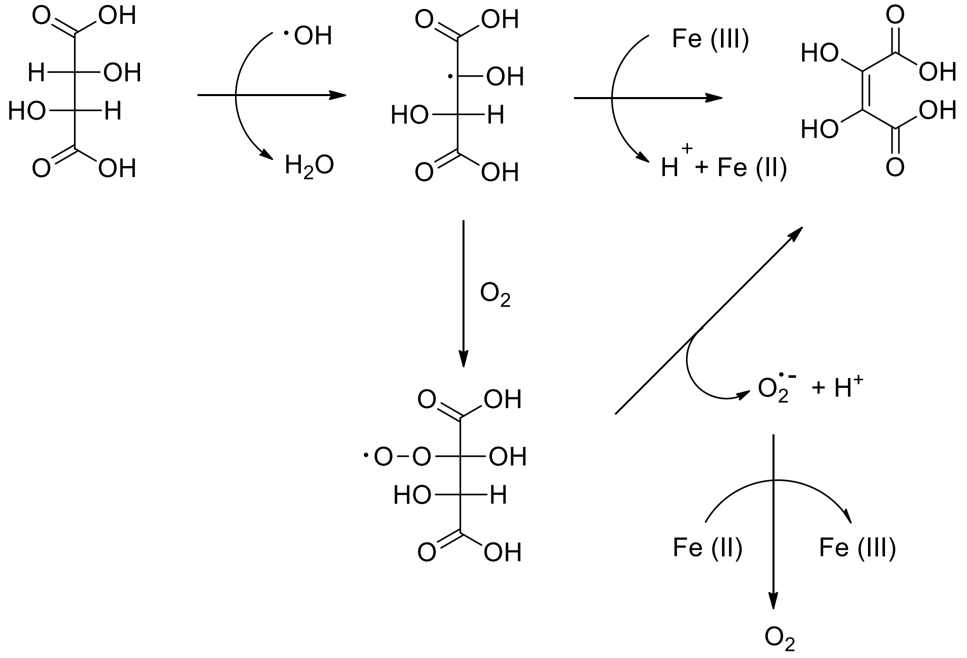

Scheme 4.1: Proposed mechanism for the formation of dihydroxymaleic acid from tartaric acid and the catalytic properties of iron (II) under hydrogen peroxide conditions.

Since then, the Fenton reaction has been further explored for areas beyond the detection of tartaric acid, such as the oxidative degradation of organic compounds and common pollutants.

While most Fenton reactions are focused on homogeneous conditions which utilize iron sulfate salts, there have been several studies which explore the use of iron nanoparticles and nanocomposites for the degradation of organic pollutants under heterogeneous conditions. For example, Lejin Xu and Jianlong Wang utilized magnetic Fe_3O_4 nanoparticles for the degradation of 2,4-dichlorophenol, achieving complete decomposition and 51% removal of total organic compounds (TOC) in just 180 minutes.[213] Similarly, Ruixiong Huang et al. studied the degradation of bisphenol-A utilizing magnetic Fe_3O_4 nanoparticles by a sono-Fenton process and found overall removal efficiencies over 95%, with about half TOC in solution eliminated.[214] Of higher interest to us, however, is the use of iron oxide nanoparticles embedded on a carbon backbone, as it more closely resembles our adsorbent material. Surprisingly, there have been many studies on iron composite materials used as Fenton reagents for the degradation of organic pollutants in water. Carbon nanotubes have been popularly utilized as anchor sites for iron oxide nanoparticles for Fenton-like processes, and have shown promising results in the degradation of organic pollutants such as 17a-methyltestosterone,[215] bisphenol-A,[216] and various phenolic compounds.[217] Other solid supports have been also been used, such as graphene[218] (used for the adsorption and degradation of methylene blue) and mesoporous silicon oxide, which is noteworthy due to being a carbon-free adsorbent/catalyst used for the degradation of methyl orange.[219]

We have performed preliminary studies of our material utilizing the Fenton reaction for the adsorption and degradation of methylene blue. Reaction conditions can be seen in section 4.2.2, with Table 4.3 summarizing the percent adsorption/degradation of a 50 ppm methylene blue solution over a 24 hour range with varying volumes of initial 30% hydrogen peroxide solution. As a negative control we utilized our adsorbent material without introducing hydrogen peroxide, which prevents the Fenton reaction and illustrates the adsorptive capabilities of our material against methylene blue.

Table 4.3: Summary of adsorption/degradation of methylene blue at varying time intervals and hydrogen peroxide concentrations.

		H_2O_2 (mL)		
Time (Hours)	Control	0.5	1	2
1	37%	44%	42%	50%
2	52%	52%	49%	53%
3	52%	52%	50%	59%
4	56%	53%	54%	62%
24	75%	87%	99%	100%

We can see in Figure 4.6 that the adsorption of methylene blue onto our material is mostly linear in nature. Our control achieved 75% adsorption of a 50 ppm methylene blue solution without the addition of hydrogen peroxide. While these results are positive, they fall short of previous materials synthesized in our lab, such as NTC shown in chapter 3 which was capable of complete adsorption at concentrations up to 500 ppm. This leads us to believe that the surface area of our iron oxide-containing adsorbent is much lower than that of NTC previously mentioned, leading to adsorption or organic contaminants being restricted to surface adsorption, without the capability of the contaminant to travel further into the adsorbent via porosities in the material. Surface area analysis such as BET would be needed in order to corroborate this theory.

Addition of hydrogen peroxide results in lower methylene blue concentration in as little time as one hour when compared to our control. Interestingly, at time 2-4 hours the difference between our control, 0.5 mL H_2O_2 and 1 mL H_2O_2 is near equivalent, with our control demonstrating slightly higher methylene blue reduction when compared to the other two conditions for some of these time frame. At 24 h we can see a larger discrepancy in the reduction of methylene blue between our control and the other three reaction conditions, with our control achieving 75% methylene blue reduction as opposed to 100% methylene blue reduction when using 2.5 mL of 30% hydrogen peroxide. A general trend can also be found, where the higher the amount of hydrogen peroxide used, the higher the methylene blue reduction that is observed after 24 h. Interestingly, the difference in reduction seems to be insignificant when using 1 mL versus 2.5 mL of hydrogen peroxide after 24 hours, indicating that 1 mL is enough over this time range to completely degrade the methylene blue in the solution.

Overall, the capabilities of this iron oxide-containing adsorbent as a Fenton reactant shows promise but needs to be further explored before determining its capabilities as a Fenton reactant. The addition of outside factors such as heat and ultrasound could be explored as factors to expedite the formation of hydroxyl radicals and contaminant degradation. A range of pH should also be explored to determine what conditions optimally allow for the formation of these radicals.

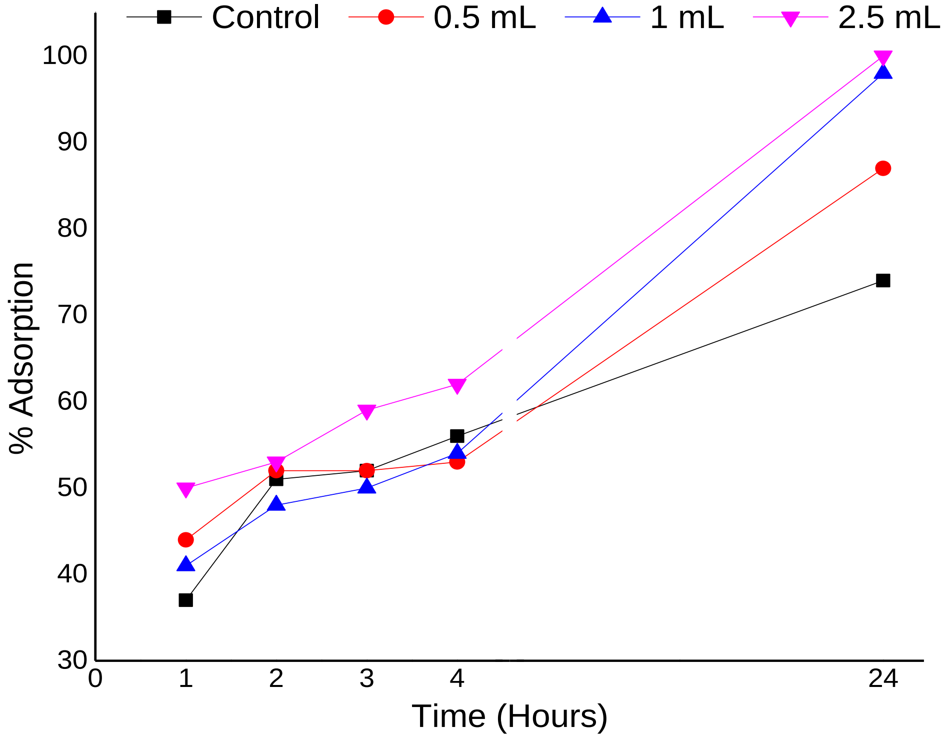

Figure 4.6: Methylene blue adsorption/degradation by Fenton reaction.

4.4 CONCLUSION AND FUTURE WORK

In conclusion, we have successfully developed an adsorbent carbon material containing iron oxide for the adsorption of heavy metals from water. Carbonization of glucose at 1000 ^{o}C over a period of two hours under anaerobic conditions yielded a material containing mostly carbon, oxygen, iron and surprisingly sulfur, as evidenced by SEM-EDS analysis. We have postulated that the sulfur content present in the material comes from carbonization in the presence of sulfate ions introduced by iron(II) sulfate. Infrared spectroscopy further corroborates this theory, as the broad absorption peak found from 1017 cm^{-1} to 1308 cm^{-1} fits the expected S=O stretching peak. X-ray diffraction analysis suggests the iron present in this material is composed of a mixture of Fe_3O_4 and Fe_2O_3, with magnetite contributing the bulk of the iron content. Adsorption capacity studies also look promising, with Q_e for lead, barium, arsenic(III) and arsenic(V) reaching 5.57 mg/g, 2.34 mg/g, 7.86 mg/g and 4.48 mg/g, respectively. These are promising results, as action levels for these contaminants set by the EPA are in much lower concentrations. Moreover, the presence of iron in our material allowed us the potential to use this for catalytic degradation of organic contaminants. We employed our material under Fenton reaction conditions by the addition of hydrogen peroxide for the degradation of methylene blue, an often-employed organic dye for adsorption and degradation studies. While our material was successful in the degradation of a 50 ppm solution of methylene blue, it required 24 hours to do so, which is not ideal for real world application.

While this iron oxide-containing adsorbent shows promise for the remediation of both organic and inorganic contaminants in water, further work still needs to be done. The surface area of the material needs to be studied, and BJH analysis is essential to elucidate the average diameter of the porosities found within the material. Should the material show low porosity, a new carbonization method would have to be developed. One possible alternative is to use zinc chloride in place of zinc oxide nanoparticles as templating agents. X-ray photoelectron spectroscopy should also be employed to help elucidate the state of the atoms present in the material, including iron (iron(II) and iron(III)) and sulfur content and composition. A more extensive XRD analysis using an online library would also prove beneficial for iron characterization.

Preliminary adsorption studies show much promise, but further adsorption tests still need to be done to fully understand the potential of this material for water remediation. Heavy metal adsorption tests were done in RO water, but their adsorption in tap water needs to be tested as well in order to more closely resemble adsorption in real world applications. Adsorption kinetics for the material still need to be performed in order to study how quickly our material can remove these heavy metals from water, and to create a suitable adsorption isotherm for the material. Adsorption under acidic and basic conditions should also be explored to show the effects of pH on the adsorption capacities and kinetics. Adsorption and degradation of organic contaminants via the Fenton reaction still needs much more testing; the effects of temperature and pH can greatly affect the degradation kinetics of the reaction and must therefore be explored. Moreover, other methods for activating the formation of hydroxyl radicals should be explored, for example by the use of ultrasound.

In all, the material shows great promise, but further testing and characterization are still required.

Chapter 5: Thiol-Functionalized Porous Carbon for the Adsorption of Soft Metals from Water

5.1 INTRODUCTION

While porous organic adsorbents such as activated carbon are efficient at removing organic contaminants from water, the removal of inorganic contaminants can prove to be challenging. Organic contaminants can interact with porous carbon materials through van der Waals, hydrophobic, pi-pi and even ionic interactions. However, inorganic contaminants generally lack these interactions, and as such their adsorption by carbon adsorbents is limited. The addition of functional groups to these adsorbents is one way to remediate this problem. In order to effectively adsorb metal ions in solution, an optimal carbon-based adsorbent needs to be capable of undergoing ion exchange, surface-complex formation, and/or chelation with the metal contaminant in order to adsorb and retain the metal contaminant.[220,221] Lewis bases such as thiols and amines can be employed in order to produce a coordinate covalent bond with heavy metal ions, increasing the material's adsorption towards the metal and reducing the risk of releasing these adsorbed contaminants back into the purified water.[207,222,223] Utilizing this Lewis acid-Lewis base interaction, thiol-functionalized materials have been explored for the removal of Hg(II), Pb(II), Ag(I), Cu(II), and even As(III) and As(V). [222,224,225]

In order to make our high-surface area adsorbent material detailed in Chapter 3 an effective adsorbent towards heavy metals, we have functionalized its surface with thiols. We have done so by following a method which involves carbonization in the presence of thiourea, a thiol-containing organic molecule. From the literature we found that thiourea is a relatively common thiol-containing molecule utilized during carbonization to add sulfur functionality to organic adsorbents. [226-229] We have employed this method by carbonizing glucose at 1000 °C over two hours under constant argon flow in the presence of zinc oxide nanoparticles and thiourea. Characterization of this material is found further in this chapter. We have also performed preliminary adsorption studies for this material against barium and arsenic(III) with promising results.

5.2 MATERIALS AND METHODS

5.2.1 Preparation of Material

Initially, D(+)-glucose (4g, 22.2 mmol) and thiourea (4g, 23.2 mmol) were dissolved in 100 mL RO water. To this solution, 4g of ZnO NPs (<35 nm particle size) were added and the suspension ultrasonicated for 30 minutes, followed by stirring for a further 30 minutes to promote homogeneity. This suspension was then concentrated under reduced pressure using a rotary evaporator, mixed further using mortar and pestle, and left to dry under reduced pressure via vacuum pump overnight.

The mixture was then weighed and transferred to a quartz crucible and placed in a sealed furnace. The furnace was argon-flushed for 30 minutes, followed by carbonization for two hours at 1000 ^{o}C with a ramp speed of 10 ^{o}C/min under constant argon flow for a final recovery of 1.17 g.

On a follow-up experiment, the above steps were repeated with 4g D(+)-glucose, 2g thiourea and 4g ZnO NPs (<35 nm particle size) for a post-carbonization recovery of 2.18g.

Washing of these materials to remove ZnO NPs after carbonization was done by exposing material to 4N HCl (5 mL HCl soln. per 100 mg material). In a 250 mL round bottom, the carbonized material was suspended in 4N HCl and left stirring overnight. The material was then filtered, washed with RO water until acid was no longer detected, and dried under vacuum. Initial weight – 1.77g, recovered 0.46g.

5.2.3 Adsorption Capacity Studies

For the adsorption of heavy metals, 100 ppm stock solutions were made for $BaCl_2•2H_2O$ (17.85 mg) and $NaAsO_2$ (17.54 mg) in 100 mL RO water, respectively. The mixtures were ultrasonicated to ensure full dissolution. These 100 ppm stock solutions were used to make 10 ppm, 1 ppm and 0.1 ppm contaminant solutions used for the study. Adsorption capacity studies were done in triplicate in 20 mL vials using 10 mg of adsorbent and 10 mL of contaminant solution under constant stirring for three days to allow for adsorption equilibrium. At this point the experiments were centrifuged, 7.5 mL of each sample transferred to a clean centrifuge tube, and 2.5 mL of a 12% nitric acid solution was added to acidify each solution for ICP-OES analysis.

5.2.4 Characterization

Carbonization was performed using a GSL-1100X from MTI Corporation. The X-ray diffraction analysis of the carbon material and the embedded nanoparticles was performed on a Panalytical Empyrean 2 diffractometer (Cu anode, Kα radiation, λ = 1.54 nm) with a scan rate of 1.7 deg/min. A Hitachi S-4800 instrument was used for high resolution SEM imaging and elemental analysis. Lower resolution SEM-EDS measurements were performed on a Hitachi SU 3500 SEM equipped with a STEM detector. Samples for electron microscopy were placed as powders in 12 mm diameter carbon adhesive tabs. Infrared spectroscopy analysis was done on a Nicolet iS5 FTIR with ATR module using a scanning range of 650-4000 cm^{-1}. ICP-OES measurements were performed on a Perkin Elmer OPTIMA 4300 DV ICP-OES.

5.3 RESULTS AND DISCUSSION

5.3.1 Electron Microscopy

Scanning electron microscopy image of our thiol-containing adsorbent can be seen in Figure 5.1. At a magnification of 300 μm we can see a highly irregular material with larger sections of the adsorbent being surrounded by smaller spherical sections. Some porosities can be observed in the material, however at this magnification we cannot determine whether these are true porosities or simply crevices inherent to the amorphous material.

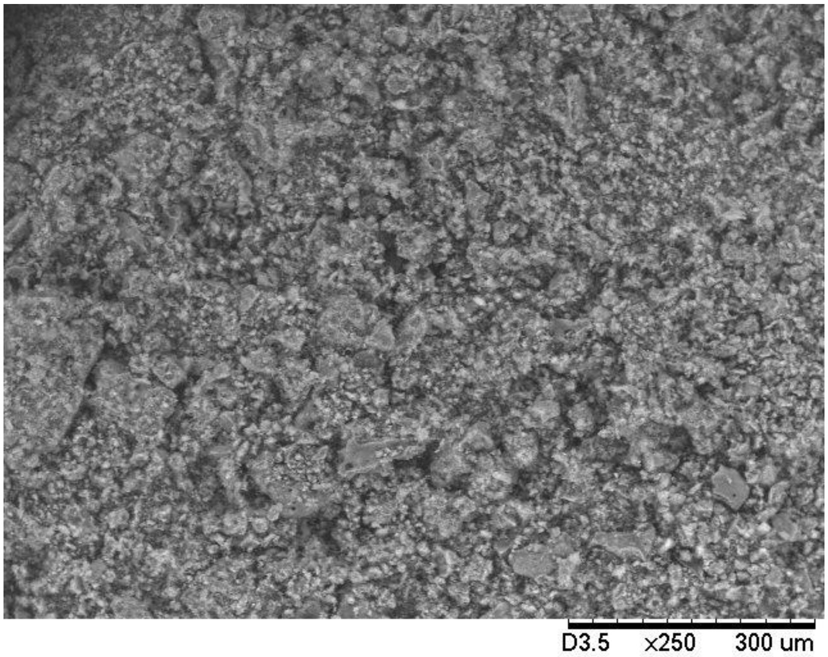

Figure 5.1: Scanning electron microscope image of thiol-containing adsorbent.

Elemental mapping of our thiol-containing adsorbent after carbonization can be seen in Figure 5.2. From the elemental analysis we can see the adsorbent is largely composed of carbon and sulfur, distributed nearly homogeneously throughout the material. The weight percent composition for carbon, sulfur and zinc was 55.71%, 23.26% and 21.01%, respectively. Interestingly, oxygen content was not detected in the analysis, suggesting the removal of oxygen during carbonization as either water or small organic molecules, as is common when carbonizing carbohydrates at higher temperatures. While carbonization at 1000 ºC for two hours was enough to eliminate zinc from NTC (see Chapter 3), it appears that under these conditions a large portion of zinc still remained in our thiol-containing adsorbent, despite washing the material several times with RO water after carbonization to remove unreacted material. In order to remove the zinc we reacted the material in a 4N HCl solution overnight.

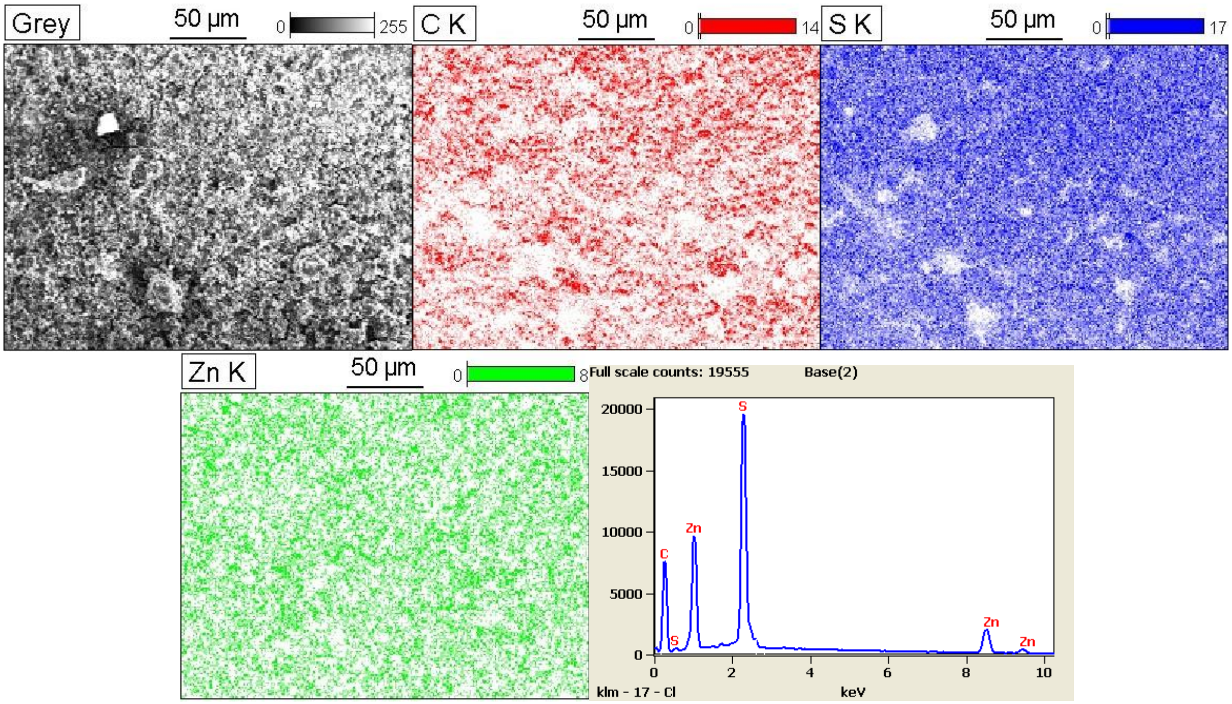

Figure 5.2: Elemental mapping and composition of thiol-containing adsorbent.

Figure 5.3 shows the SEM of our thiol-containing adsorbent before (top) and after (bottom) reacting with 4N HCl. It should be noted that this analysis was conducted on a benchtop SEM equipped with a module for elemental analysis; elements under aluminum are undetectable, therefore carbon and oxygen content could unfortunately not be analyzed. Hydrochloric acid is able to dissolve zinc nanoparticles, turning the O-Zn-O network into water and $ZnCl_2$, which is water soluble. We can see the effectiveness of this method for removing remaining ZnO nanoparticles in the SEMs shown below, as the zinc content decreases from 51.2% to non-observable weight percent after the reaction (Table 5.1). With the loss of zinc, sulfur content of the material increases from 51.2% to 94.4% by weight; it should be noted that this weight percent excludes carbon content, as the instrument is incapable of analyzing it. There is also small residual aluminum content present, likely resulting from the aluminum stage used during analysis.

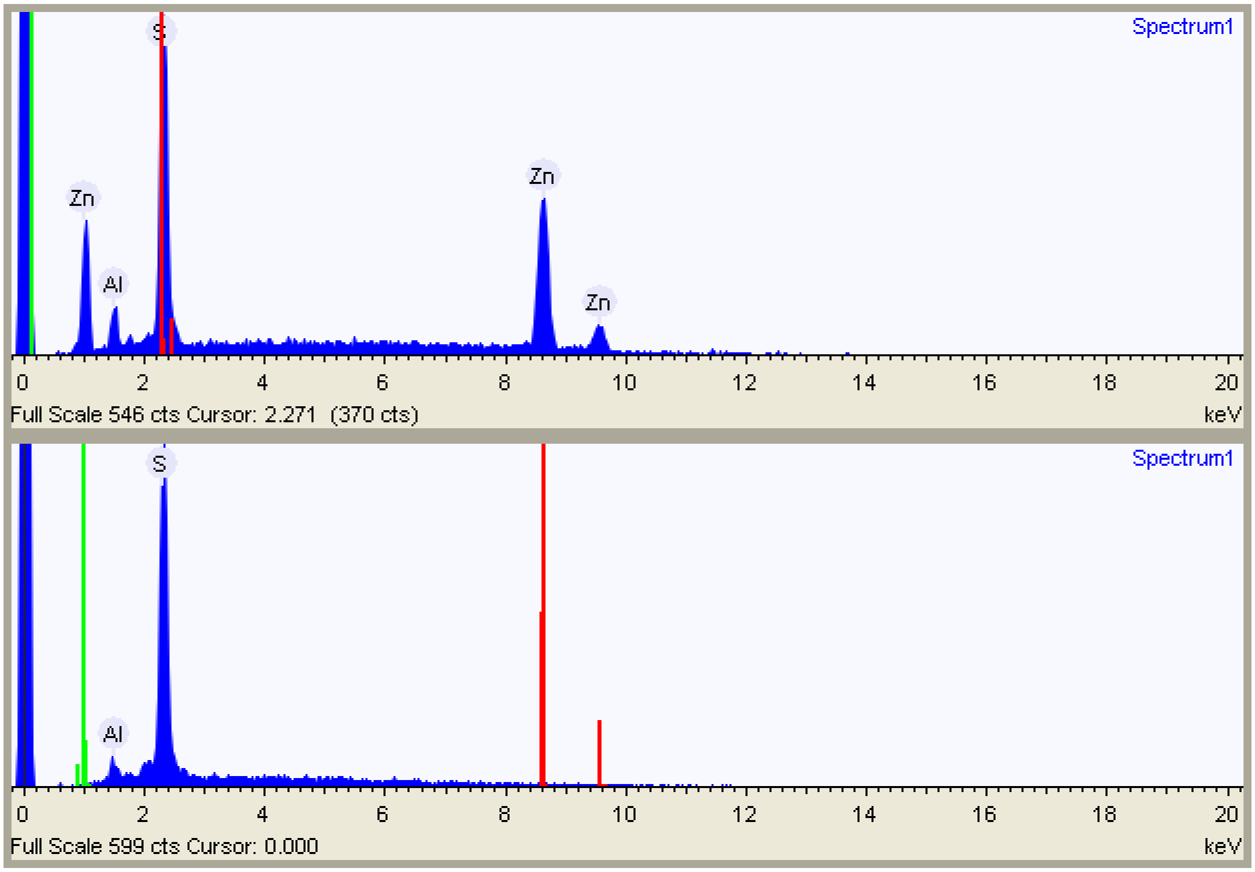

Figure 5.3: SEM-EDS Images of material before acid wash (top) and after acid wash (bottom).

Table 5.1: Atomic composition by weight percent before and after 4N HCl wash.

	Weight %	
	Before Wash	After Wash
Aluminum	9.0	5.6
Sulfur	39.8	94.4
Zinc	51.2	N/A

5.3.2 X-ray Diffraction Spectroscopy

X-ray powder diffraction analysis of our thiol-containing adsorbent can be seen in Figure 5.4 below. The material shows a mostly amorphous structure, with the appearance of two broad signals in the ranges of 17° – 32° and 38° – 48°, with the highest intensities centered around 22.9° and 43.25°. These two peaks centered around 22.9° and 43.25° can be attributed to the (002) and (100) planes, respectively, which are often found in disordered carbon layers.[230,231] Much like with our NTC material synthesized in the past, this material demonstrates a highly amorphous structure with no clearly defined crystallinity.

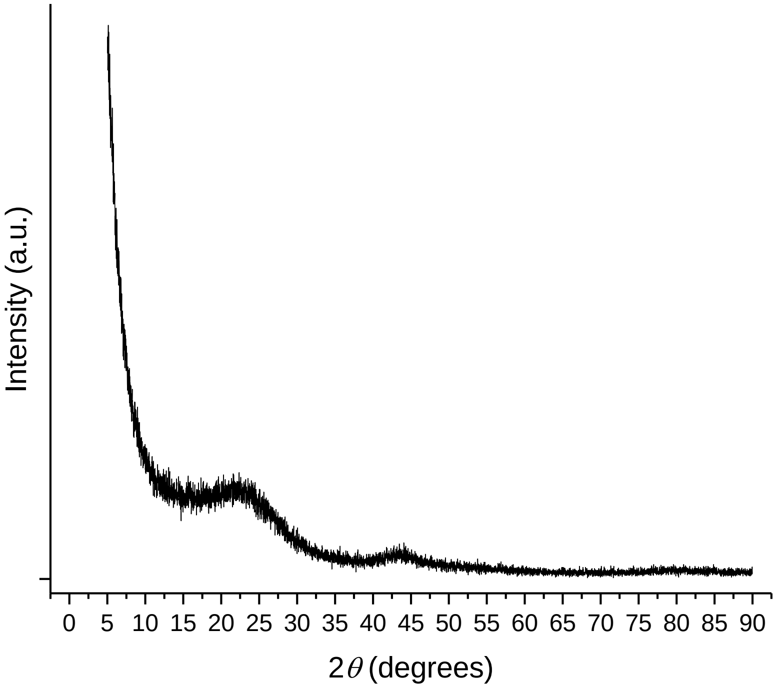

Figure 5.4: X-ray diffractogram of thiol-containing adsorbent.

5.3.3 Infrared Spectroscopy

Fourier transform infrared spectroscopy analysis for our thiol-containing adsorbent can be seen in Figure 5.5 below. Direct analysis of our material resulted in what can be best described as a flatline with few visible dips in the reading, mainly at 1630 cm^{-1} and 2220 cm^{-1}

(Figure 5.5, Before Correction, black). Due to the similarities in the preparation of this material and NTC (Chapter 3), we performed an instrument baseline with NTC in an effort to highlight the difference between our thiol-containing adsorbent and NTC, namely the presence of sulfur (Figure 5.5, After Correction, red). After performing this baseline correction the appearance of broad, better defined absorption peaks were detected, with the main signals centered around 1385 cm^{-1}, 1632 cm^{-1} and 1693 cm^{-1}. Interestingly, there were also places where our material seems to be showing signs of transmittance in place of absorption, namely at 1059 cm^{-1}, 2158 cm^{-1}, 2337 cm^{-1} and 2365 cm^{-1}, with minor transmittance signals at 2850 cm^{-1} and 2919 cm^{-1}. Sulfur C-S stretching signals are often reported in the ranges of 710 – 570 cm^{-1}, C=S stretching from 1030 – 1275 cm^{-1}, S-S stretching from 700 – 550 cm^{-1}, S=O from 1225 – 980 cm^{-1}, S-N stretching near 700 cm^{-1}, and S-H as a weak signal in the range of 2550 – 2620 cm^{-1}. Our material, unfortunately, doesn't show a match between any of our signals and the ranges previously reported for common sulfur compounds, either before or after baseline correction with NTC. The more prominent signals found at 1632 cm^{-1} and 1693 cm^{-1} could be attributed to C=C stretching from alkenes formed during carbonization, as alkenes tend to show signals between 1600 cm^{-1} and 1700 cm^{-1}.

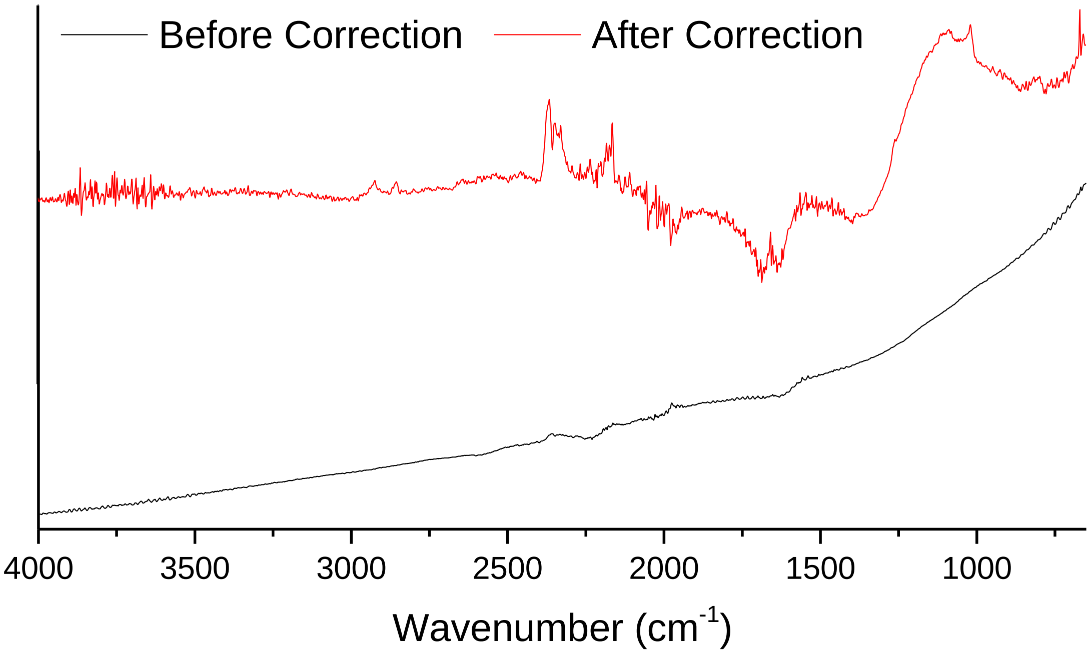

Figure 5.5: Infrared Spectrum of thiol-containing adsorbent before (black) and after (red) baseline correction.

5.3.4 Adsorption Studies

The adsorption capabilities of our thiol-containing adsorbent against barium and arsenic(III) were explored and can be seen in Figure 5.6 below. Reaction conditions can be seen under section 5.2.3, with a summary of the adsorption capacities for this material against under varying initial contaminant concentrations outlined in Table 5.2.

Adsorption against barium at initial concentrations of 0.1 and 1 ppm were satisfactory, with our material achieving an adsorption capacity of 0.032 and 0.441 mg/g, respectively. Excitingly, at a barium concentration of 10 ppm our material achieved an adsorption capacity of 8.65 mg/g, indicating a potential use of our thiol-containing adsorbent for larger scale decontamination of barium. As mentioned previously, toxicity levels for barium are set to 0.5 mg/L for soluble barium compounds.[210] However, many wastewater products can be riddled with heavy metal contamination, such as fracking water which contains alarmingly high concentrations of barium and strontium.[232,233] Our material demonstrates promising results as a possible remedy for the removal of barium for these contaminated fracking wastewaters.

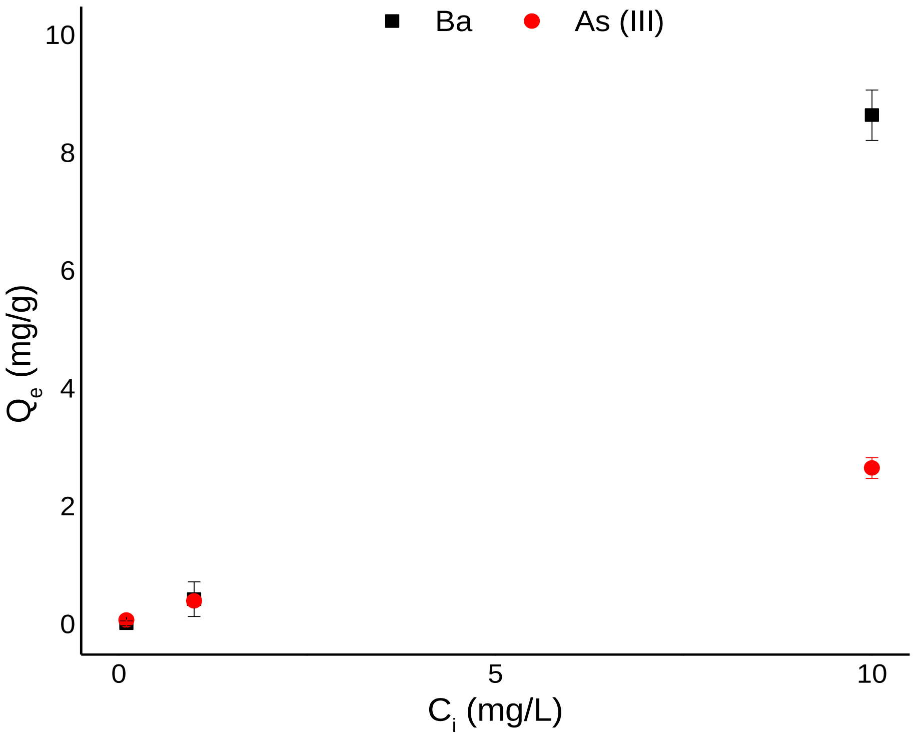

Figure 5.6: Adsorption capacity against barium and arsenic (III).

Adsorption for arsenic(III) at concentrations of 0.1 and 1 ppm were similar to those against barium, with adsorption capacities of 0.086 and 0.411 mg/g, respectively. Unlike barium, adsorption capacity at initial concentration of 10 ppm achieved an adsorption capacity of 2.66 mg/g, less than three times what was achieved against barium. As previously mentioned, the world health organization has set arsenic safe levels to 10 ppb, considerably lower than the adsorption capacity of our material against arsenic(III), making our material a viable option for the removal of arsenic(III) from contaminated water. Interestingly, this thiol-containing adsorbent achieved an adsorption capacity above 8 mg/g for barium(II), while the iron oxide-containing adsorbent achieved an adsorption capacity above 7.8 mg/g against arsenic(III). In the future, perhaps a carefully designed adsorbent featuring both thiols and iron oxide nanoparticles could provide an adsorbent which could function to remove both contaminants from water simultaneously, while maintaining a porous carbon structure to achieve higher surface area and thus higher adsorption capacities.

Table 5.2: Summary of adsorption capacity study against barium and arsenic (III).

C_i (ppm)	0.1		1		10	
	Q_e (mg/g)	St. Dev.	Q_e (mg/g)	St. Dev.	Q_e (mg/g)	St. Dev.
Barium	0.032203	0.042443	0.441258	0.294896	8.656172	0.429686
Arsenic(III)	0.086194	0.001355	0.411294	0.009467	2.667108	0.176021

5.4 CONCLUSION AND FUTURE WORK

In conclusion, we have created a carbon adsorbent which has been functionalized with sulfur for the adsorption of metals in contaminated water. While zinc was still present after carbonization at 1000 °C over a period of two hours, it was successfully removed after overnight exposure to 4N HCl while maintaining sulfur content of the material, as shown by SEM-EDS. Infrared spectroscopy and X-ray diffraction proved inconclusive, with IR showing the presence of alkene C=C and XRD showing the presence of disordered carbon layers of probable graphenic nature, but neither could prove the presence or state of sulfur in our adsorbent. Preliminary adsorption studies against barium and arsenic (III) show promise, with adsorption capacities at 8.65 and 2.66 mg/g, respectively.

In the future, further analysis and more rigorous adsorption tests need to be conducted on this material in order to fully understand its potential for water remediation. Further FTIR experiments on a more potent machine could help elucidate the state of sulfur on the material. More to the point, XPS analysis would be a more conclusive instrument to reveal both the presence and the state of sulfur in this compound. Surface area analysis is also needed in order to find the surface area, with BJH analysis required to analyze the average pore size. Adsorption capacity studies should also be done not only in RO water, but in tap water to more closely resemble adsorption in real world applications. Adsorption capacities towards other heavy metals, such as mercury and arsenic(V), should also be explored. Adsorption kinetics and the effect of pH also need to be studied; this can help elucidate the speed at which our adsorbent can trap contaminants, which adsorption isotherm best describes this adsorption, and under what conditions adsorption for these contaminants is optimal.

References

(1) Lapworth, D. J.; Baran, N.; Stuart, M. E.; Ward, R. S. *Environmental Pollution* **2012**, *163*, 287.

(2) Verstraeten, I. M.; Fetterman, G. S.; Meyer, M. T.; Bullen, T.; Sebree, S. K. *Groundwater Monitoring & Remediation* **2005**, *25*, 107.

(3) Heberer, T.; Mechlinski, A.; Fanck, B.; Knappe, A.; Massmann, G.; Pekdeger, A.; Fritz, B. *Groundwater Monitoring & Remediation* **2004**, *24*, 70.

(4) Kümmerer, K. *Chemosphere* **2001**, *45*, 957.

(5) Eckel, W. P.; Ross, B.; Isensee, R. K. *Groundwater* **1993**, *31*, 801.

(6) Buerge, I. J.; Buser, H.-R.; Kahle, M.; Müller, M. D.; Poiger, T. *Environmental Science & Technology* **2009**, *43*, 4381.

(7) Heathwaite, A. L.; Quinn, P. F.; Hewett, C. J. M. *Journal of Hydrology* **2005**, *304*, 446.

(8) Chiew, F. H. S.; McMahon, T. A. *Water Science and Technology* **1999**, *39*, 241.

(9) Kim, G.; Yur, J.; Kim, J. *Journal of Environmental Management* **2007**, *85*, 9.

(10) Mohan, D.; Sarswat, A.; Ok, Y. S.; Pittman, C. U. *Bioresource Technology* **2014**, *160*, 191.

(11) Srivastav, A. L.; Ranjan, M. In *Inorganic Pollutants in Water*; Devi, P., Singh, P., Kansal, S. K., Eds.; Elsevier: 2020, p 1.

(12) Reneau Jr, R. B.; Hagedorn, C.; Degen, M. J. *Journal of Environmental Quality* **1989**, *18*, 135.

(13) World Health Organization, G. *Guidelines for Drinking-Water Quality*; third ed ed., 2008; Vol. 1.

(14) Ahluwalia, S. S.; Goyal, D. *Bioresource Technology* **2007**, *98*, 2243.

(15) Fu, F.; Wang, Q. *Journal of Environmental Management* **2011**, *92*, 407.

(16) Ali, I.; Basheer, A. A.; Mbianda, X. Y.; Burakov, A.; Galunin, E.; Burakova, I.; Mkrtchyan, E.; Tkachev, A.; Grachev, V. *Environment International* **2019**, *127*, 160.

(17) Purkait, M. K.; DasGupta, S.; De, S. *Separation and Purification Technology* **2004**, *37*, 81.

(18) Yusuf, M.; Elfghi, F. M.; Zaidi, S. A.; Abdullah, E. C.; Khan, M. A. *RSC Advances* **2015**, *5*, 50392.

(19) Islam, M. T.; Dominguez, N.; Ahsan, M. A.; Dominguez-Cisneros, H.; Zuniga, P.; Alvarez, P. J. J.; Noveron, J. C. *Journal of Environmental Chemical Engineering* **2017**, *5*, 4185.

(20) Islam, M. T.; Padilla, J. E.; Dominguez, N.; Alvarado, D. C.; Alam, M. S.; Cooke, P.; Tecklenburg, M. M. J.; Noveron, J. C. *RSC Advances* **2016**, *6*, 91185.

(21) Padilla, J. E.; Melendez, J.; Barrera, L. A.; Wu, Y.; Ventura, K.; Veleta, J. M.; Islam, M. T.; Chavez, C. A.; Katla, S. K.; Villagrán, D.; Noveron, J. C. *Journal of Environmental Chemical Engineering* **2018**, *6*, 1027.

(22) Barrera, L. A.; Escobosa, A. C.; Nevarez, A.; Dominguez, N.; Bañuelos, J. L.; Westerhoff, P.; Noveron, J. C. *Journal of Water Process Engineering* **2019**, *28*, 331.

(23) Islam, M. T.; Jing, H.; Yang, T.; Zubia, E.; Goos, A. G.; Bernal, R. A.; Botez, C. E.; Narayan, M.; Chan, C. K.; Noveron, J. C. *Journal of Environmental Chemical Engineering* **2018**, *6*, 3827.

(24) Homem, V.; Santos, L. *Journal of Environmental Management* **2011**, *92*, 2304.

(25) Kim, S.; Chu, K. H.; Al-Hamadani, Y. A. J.; Park, C. M.; Jang, M.; Kim, D.-H.; Yu, M.; Heo, J.; Yoon, Y. *Chemical Engineering Journal* **2018**, *335*, 896.
(26) Al-Qodah, Z.; Al-Shannag, M. *Separation Science and Technology* **2017**, *52*, 2649.
(27) Bazrafshan, E.; Mohammadi, L.; Ansari-Moghaddam, A.; Mahvi, A. H. *Journal of Environmental Health Science and Engineering* **2015**, *13*, 74.
(28) Li, P.-S.; Tao, H.-C. *Critical Reviews in Microbiology* **2015**, *41*, 140.
(29) Ahsan, M. A.; Katla, S. K.; Islam, M. T.; Hernandez-Viezcas, J. A.; Martinez, L. M.; Díaz-Moreno, C. A.; Lopez, J.; Singamaneni, S. R.; Banuelos, J.; Gardea-Torresdey, J.; Noveron, J. C. *Environmental Technology & Innovation* **2018**, *11*, 23.
(30) Jiang, Y.; Liu, Z.; Zeng, G.; Liu, Y.; Shao, B.; Li, Z.; Liu, Y.; Zhang, W.; He, Q. *Environmental Science and Pollution Research* **2018**, *25*, 6158.
(31) Li, J.; Zheng, B.; He, Y.; Zhou, Y.; Chen, X.; Ruan, S.; Yang, Y.; Dai, C.; Tang, L. *Ecotoxicology and Environmental Safety* **2018**, *156*, 125.
(32) Renu; Agarwal, M.; Singh, K. *Journal of Water Reuse and Desalination* **2016**, *7*, 387.
(33) Alhashimi, H. A.; Aktas, C. B. *Resources, Conservation and Recycling* **2017**, *118*, 13.
(34) Rytwo, G.; Gonen, Y. *Desalination and Water Treatment* **2009**, *11*, 318.
(35) Da'na, E. *Microporous and Mesoporous Materials* **2017**, *247*, 145.
(36) Zhang, L.; Yu, C.; Zhao, W.; Hua, Z.; Chen, H.; Li, L.; Shi, J. *Journal of Non-Crystalline Solids* **2007**, *353*, 4055.
(37) Lee, J. Y.; Chen, C. H.; Cheng, S.; Li, H. Y. *International Journal of Environmental Science and Technology* **2016**, *13*, 65.
(38) Aguado, J.; Arsuaga, J. M.; Arencibia, A.; Lindo, M.; Gascón, V. *Journal of Hazardous Materials* **2009**, *163*, 213.
(39) Lam, K. F.; Yeung, K. L.; McKay, G. *Langmuir* **2006**, *22*, 9632.
(40) Yang, H.; Xu, R.; Xue, X.; Li, F.; Li, G. *Journal of Hazardous Materials* **2008**, *152*, 690.
(41) Chubar, N.; Gilmour, R.; Gerda, V.; Mičušík, M.; Omastova, M.; Heister, K.; Man, P.; Fraissard, J.; Zaitsev, V. *Advances in Colloid and Interface Science* **2017**, *245*, 62.
(42) Chubar, N.; Gerda, V.; Megantari, O.; Mičušík, M.; Omastova, M.; Heister, K.; Man, P.; Fraissard, J. *Chemical Engineering Journal* **2013**, *234*, 284.
(43) Li, Z.; Yang, B.; Zhang, S.; Wang, B.; Xue, B. *Journal of Materials Chemistry A* **2014**, *2*, 10202.
(44) Goh, K.-H.; Lim, T.-T.; Dong, Z. *Environmental Science & Technology* **2009**, *43*, 2537.
(45) Hertel, T.; Novais, R. M.; Murillo Alarcón, R.; Labrincha, J. A.; Pontikes, Y. *Journal of Cleaner Production* **2019**, *227*, 877.
(46) Khan, M. I.; Min, T. K.; Azizli, K.; Sufian, S.; Ullah, H.; Man, Z. *RSC Advances* **2015**, *5*, 61410.
(47) Falah, M.; MacKenzie, K. J. D.; Knibbe, R.; Page, S. J.; Hanna, J. V. *Journal of Hazardous Materials* **2016**, *318*, 772.
(48) Simeonidis, K.; Mourdikoudis, S.; Kaprara, E.; Mitrakas, M.; Polavarapu, L. *Environmental Science: Water Research & Technology* **2016**, *2*, 43.
(49) Li, Z.; Xu, S.; Xiao, G.; Qian, L.; Song, Y. *Journal of Environmental Management* **2019**, *244*, 33.
(50) Vilardi, G.; Mpouras, T.; Dermatas, D.; Verdone, N.; Polydera, A.; Di Palma, L. *Chemosphere* **2018**, *201*, 716.

(51) Saslow, S. A.; Um, W.; Pearce, C. I.; Engelhard, M. H.; Bowden, M. E.; Lukens, W.; Leavy, I. I.; Riley, B. J.; Kim, D.-S.; Schweiger, M. J.; Kruger, A. A. *Environmental Science & Technology* **2017**, *51*, 8635.

(52) Kanel, S. R.; Choi, H. *Journal of Hazardous, Toxic, and Radioactive Waste* **2017**, *21*, 04016028.

(53) Sadegh, H.; Shahryari Ghoshekandi, R.; Masjedi, A. L. I.; Mahmoodi, Z.; Kazemi, M. *INTERNATIONAL JOURNAL OF NANO DIMENSION (IJND)* **2016**, *7*, 109.

(54) Latrous El Atrache, L.; Hachani, M.; Kefi, B. B. *International Journal of Environmental Science and Technology* **2016**, *13*, 201.

(55) Nyairo, W. N.; Eker, Y. R.; Kowenje, C.; Akin, I.; Bingol, H.; Tor, A.; Ongeri, D. M. *Separation Science and Technology* **2018**, *53*, 1498.

(56) Balog, R.; Manilo, M.; Vanyorek, L.; Csoma, Z.; Barany, S. *RSC Advances* **2020**, *10*, 3184.

(57) Li, C.; Yan, Y.; Zhang, Q.; Zhang, Z.; Huang, L.; Zhang, J.; Xiong, Y.; Tan, S. *Langmuir* **2019**, *35*, 4481.

(58) Zhang, X.; Gao, B.; Creamer, A. E.; Cao, C.; Li, Y. *Journal of Hazardous Materials* **2017**, *338*, 102.

(59) Dąbrowski, A.; Podkościelny, P.; Hubicki, Z.; Barczak, M. *Chemosphere* **2005**, *58*, 1049.

(60) Babel, S.; Kurniawan, T. A. *Journal of Hazardous Materials* **2003**, *97*, 219.

(61) Robinson, T.; McMullan, G.; Marchant, R.; Nigam, P. *Bioresource Technology* **2001**, *77*, 247.

(62) Delgado, L. F.; Charles, P.; Glucina, K.; Morlay, C. *Science of The Total Environment* **2012**, *435-436*, 509.

(63) Foo, K. Y.; Hameed, B. H. *Journal of Hazardous Materials* **2009**, *171*, 54.

(64) Aktaş, Ö.; Çeçen, F. *International Biodeterioration & Biodegradation* **2007**, *59*, 257.

(65) Li Puma, G.; Bono, A.; Krishnaiah, D.; Collin, J. G. *Journal of Hazardous Materials* **2008**, *157*, 209.

(66) Chen, L.; Han, Q.; Li, W.; Zhou, Z.; Fang, Z.; Xu, Z.; Wang, Z.; Qian, X. *Environmental Science and Pollution Research* **2018**, *25*, 25840.

(67) Luo, S.; Xu, X.; Zhou, G.; Liu, C.; Tang, Y.; Liu, Y. *Journal of Hazardous Materials* **2014**, *274*, 145.

(68) Zhang, Z.; Dong, Y.; Xiao, F.; Wang, S. *RSC Advances* **2015**, *5*, 83480.

(69) Hu, X.-j.; Liu, Y.-g.; Wang, H.; Chen, A.-w.; Zeng, G.-m.; Liu, S.-m.; Guo, Y.-m.; Hu, X.; Li, T.-t.; Wang, Y.-q.; Zhou, L.; Liu, S.-h. *Separation and Purification Technology* **2013**, *108*, 189.

(70) Tiwari, J. N.; Mahesh, K.; Le, N. H.; Kemp, K. C.; Timilsina, R.; Tiwari, R. N.; Kim, K. S. *Carbon* **2013**, *56*, 173.

(71) Jiao, T.; Liu, Y.; Wu, Y.; Zhang, Q.; Yan, X.; Gao, F.; Bauer, A. J. P.; Liu, J.; Zeng, T.; Li, B. *Scientific Reports* **2015**, *5*, 12451.

(72) Afroze, S.; Sen, T. K. *Water, Air, & Soil Pollution* **2018**, *229*, 225.

(73) Ahmadpour, A.; Do, D. D. *Carbon* **1996**, *34*, 471.

(74) Caturla, F.; Molina-Sabio, M.; Rodríguez-Reinoso, F. *Carbon* **1991**, *29*, 999.

(75) Rodríguez-Reinoso, F.; Molina-Sabio, M. *Carbon* **1992**, *30*, 1111.

(76) Mohan, D.; Pittman, C. U.; Bricka, M.; Smith, F.; Yancey, B.; Mohammad, J.; Steele, P. H.; Alexandre-Franco, M. F.; Gómez-Serrano, V.; Gong, H. *Journal of Colloid and Interface Science* **2007**, *310*, 57.

(77) Wang, S.; Gao, B.; Zimmerman, A. R.; Li, Y.; Ma, L.; Harris, W. G.; Migliaccio, K. W. *Bioresource Technology* **2015**, *175*, 391.
(78) Samsuri, A. W.; Sadegh-Zadeh, F.; Seh-Bardan, B. J. *Journal of Environmental Chemical Engineering* **2013**, *1*, 981.
(79) Pan, J.; Jiang, J.; Xu, R. *Journal of Environmental Sciences* **2013**, *25*, 1957.
(80) Keiluweit, M.; Nico, P. S.; Johnson, M. G.; Kleber, M. *Environmental Science & Technology* **2010**, *44*, 1247.
(81) Lima, I. M.; Boateng, A. A.; Klasson, K. T. *Journal of Chemical Technology & Biotechnology* **2010**, *85*, 1515.
(82) Yang, Z.-h.; Xiong, S.; Wang, B.; Li, Q.; Yang, W.-c. *Journal of Central South University* **2013**, *20*, 1319.
(83) Zhang, H.; Chen, C.; Gray, E. M.; Boyd, S. E. *Biomass and Bioenergy* **2017**, *105*, 136.
(84) Gao, F.; Xue, Y.; Deng, P.; Cheng, X.; Yang, K. *Chemical Speciation & Bioavailability* **2015**, *27*, 92.
(85) Xue, Y.; Gao, B.; Yao, Y.; Inyang, M.; Zhang, M.; Zimmerman, A. R.; Ro, K. S. *Chemical Engineering Journal* **2012**, *200-202*, 673.
(86) Ahmad, M.; Lee, S. S.; Dou, X.; Mohan, D.; Sung, J.-K.; Yang, J. E.; Ok, Y. S. *Bioresource Technology* **2012**, *118*, 536.
(87) Chen, X.; Chen, G.; Chen, L.; Chen, Y.; Lehmann, J.; McBride, M. B.; Hay, A. G. *Bioresource Technology* **2011**, *102*, 8877.
(88) Mullen, C. A.; Boateng, A. A.; Goldberg, N. M.; Lima, I. M.; Laird, D. A.; Hicks, K. B. *Biomass and Bioenergy* **2010**, *34*, 67.
(89) Lee, J. W.; Kidder, M.; Evans, B. R.; Paik, S.; Buchanan Iii, A. C.; Garten, C. T.; Brown, R. C. *Environmental Science & Technology* **2010**, *44*, 7970.
(90) Wang, X. S.; Chen, L. F.; Li, F. Y.; Chen, K. L.; Wan, W. Y.; Tang, Y. J. *Journal of Hazardous Materials* **2010**, *175*, 816.
(91) Kloss, S.; Zehetner, F.; Dellantonio, A.; Hamid, R.; Ottner, F.; Liedtke, V.; Schwanninger, M.; Gerzabek, M. H.; Soja, G. *Journal of Environmental Quality* **2012**, *41*, 990.
(92) Kong, H.; He, J.; Gao, Y.; Wu, H.; Zhu, X. *Journal of Agricultural and Food Chemistry* **2011**, *59*, 12116.
(93) Yuan, J.-H.; Xu, R.-K.; Zhang, H. *Bioresource Technology* **2011**, *102*, 3488.
(94) Bagreev, A.; Bandosz, T. J.; Locke, D. C. *Carbon* **2001**, *39*, 1971.
(95) Chen, T.; Zhang, Y.; Wang, H.; Lu, W.; Zhou, Z.; Zhang, Y.; Ren, L. *Bioresource Technology* **2014**, *164*, 47.
(96) Inyang, M.; Gao, B.; Yao, Y.; Xue, Y.; Zimmerman, A. R.; Pullammanappallil, P.; Cao, X. *Bioresource Technology* **2012**, *110*, 50.
(97) Guo, Y.; Yadav, A.; Karanfil, T. *Environmental Science & Technology* **2007**, *41*, 7888.
(98) Ding, L.; Snoeyink, V. L.; Mariñas, B. J.; Yue, Z.; Economy, J. *Environmental Science & Technology* **2008**, *42*, 1227.
(99) Moyer, P.; Kim, K.; Abdoulmoumine, N.; Chmely, S. C.; Long, B. K.; Carrier, D. J.; Labbé, N. *Biotechnology for Biofuels* **2018**, *11*, 265.
(100) Mohamad Nor, N.; Lau, L. C.; Lee, K. T.; Mohamed, A. R. *Journal of Environmental Chemical Engineering* **2013**, *1*, 658.
(101) Namazi, A. B.; Jia, C. Q.; Allen, D. G. *Water science and technology : a journal of the International Association on Water Pollution Research* **2010**, *62*, 2637.

(102) Madhu, R.; Veeramani, V.; Chen, S.-M.; Veerakumar, P.; Liu, S.-B.; Miyamoto, N. *Physical Chemistry Chemical Physics* **2016**, *18*, 16466.

(103) Sevilla, M.; Mokaya, R. *Energy & Environmental Science* **2014**, *7*, 1250.

(104) Li, J.; Lu, R.; Dou, B.; Ma, C.; Hu, Q.; Liang, Y.; Wu, F.; Qiao, S.; Hao, Z. *Environmental Science & Technology* **2012**, *46*, 12648.

(105) Carter, E. M.; Katz, L. E.; Speitel, G. E.; Ramirez, D. *Environmental Science & Technology* **2011**, *45*, 6498.

(106) Feng, W.; Kwon, S.; Borguet, E.; Vidic, R. *Environmental Science & Technology* **2005**, *39*, 9744.

(107) Shin, H.-C.; Park, J.-W.; Park, K.; Song, H.-C. *Environmental Pollution* **2002**, *119*, 227.

(108) Ji, L.; Shao, Y.; Xu, Z.; Zheng, S.; Zhu, D. *Environmental Science & Technology* **2010**, *44*, 6429.

(109) Li, L.; Quinlivan, P. A.; Knappe, D. R. U. *Carbon* **2002**, *40*, 2085.

(110) Anjum, H.; Murugesan, T. *Procedia Engineering* **2016**, *148*, 1346.

(111) Houas, A.; Lachheb, H.; Ksibi, M.; Elaloui, E.; Guillard, C.; Herrmann, J.-M. *Applied Catalysis B: Environmental* **2001**, *31*, 145.

(112) Michael, I.; Hapeshi, E.; Aceña, J.; Perez, S.; Petrović, M.; Zapata, A.; Barceló, D.; Malato, S.; Fatta-Kassinos, D. *Science of The Total Environment* **2013**, *461-462*, 39.

(113) Maroga Mboula, V.; Héquet, V.; Gru, Y.; Colin, R.; Andrès, Y. *Journal of Hazardous Materials* **2012**, *209-210*, 355.

(114) Vattikuti, S. V. P.; Police, A. K. R.; Shim, J.; Byon, C. *Scientific Reports* **2018**, *8*, 4194.

(115) Prabhakar Vattikuti, S. V.; Shome, S.; Koyyada, G.; Shim, J.; Jung, J. H. *Materials Research Bulletin* **2018**, *107*, 446.

(116) Police, A. K. R.; Chennaiahgari, M.; Boddula, R.; Vattikuti, S. V. P.; Mandari, K. K.; Chan, B. *Materials Research Bulletin* **2018**, *98*, 314.

(117) Vattikuti, S. V. P.; Reddy, P. A. K.; Shim, J.; Byon, C. *ACS Omega* **2018**, *3*, 7587.

(118) Pelaez, M.; Nolan, N. T.; Pillai, S. C.; Seery, M. K.; Falaras, P.; Kontos, A. G.; Dunlop, P. S. M.; Hamilton, J. W. J.; Byrne, J. A.; O'Shea, K.; Entezari, M. H.; Dionysiou, D. D. *Applied Catalysis B: Environmental* **2012**, *125*, 331.

(119) Kubo, M.; Fukuda, H.; Chua, X. J.; Yonemoto, T. *Industrial & Engineering Chemistry Research* **2007**, *46*, 699.

(120) Tryba, B.; Morawski, A. W.; Inagaki, M. *Applied Catalysis B: Environmental* **2003**, *41*, 427.

(121) Qu, L.-L.; Wang, N.; Li, Y.-Y.; Bao, D.-D.; Yang, G.-H.; Li, H.-T. *Journal of Materials Science* **2017**, *52*, 8311.

(122) Li, Y.; Li, X.; Li, J.; Yin, J. *Water Research* **2006**, *40*, 1119.

(123) Orha, C.; Pode, R.; Manea, F.; Lazau, C.; Bandas, C. *Process Safety and Environmental Protection* **2017**, *108*, 26.

(124) Becheri, A.; Dürr, M.; Lo Nostro, P.; Baglioni, P. *Journal of Nanoparticle Research* **2008**, *10*, 679.

(125) Thamaphat, K.; Limsuwan, P.; Ngotawornchai, B. *Phase characterization of TiO2 powder by XRD and TEM\n*, 2008; Vol. 42.

(126) Pardo, A.; Garcia, H.; Ramirez, P.; Carrillo-Alvarado, M. A.; Krishna, K. S.; Dominguez, N.; Islam, M. T.; Wang, H.; Noveron, J. C. *Environmental Technology & Innovation* **2018**, *11*, 321.

(127) Tan, I. A. W.; Ahmad, A. L.; Hameed, B. H. *Journal of Hazardous Materials* **2008**, *154*, 337.
(128) Ghosh, D.; Bhattacharyya, K. G. *Applied Clay Science* **2002**, *20*, 295.
(129) Rizzo, L.; Manaia, C.; Merlin, C.; Schwartz, T.; Dagot, C.; Ploy, M. C.; Michael, I.; Fatta-Kassinos, D. *Science of The Total Environment* **2013**, *447*, 345.
(130) Pitter, P.; Chudoba, J. *Biodegrability of Organic Substances in the Aquatic Environment*; CRC Press, Inc.: Boca Raton, FL, 1990.
(131) Mahugo Santana, C.; Sosa Ferrera, Z.; Esther Torres Padrón, M.; Juan Santana Rodríguez, J. *Molecules* **2009**, *14*, 298.
(132) Krugly, E.; Martuzevicius, D.; Tichonovas, M.; Jankunaite, D.; Rumskaite, I.; Sedlina, J.; Racys, V.; Baltrusaitis, J. *Chemical Engineering Journal* **2015**, *260*, 188.
(133) Piątkowska, M.; Jedziniak, P.; Olejnik, M.; Żmudzki, J.; Posyniak, A. *Food Chemistry* **2018**, *239*, 598.
(134) He, C.; Huang, J.; Yan, C.; Liu, J.; Deng, L.; Huang, K. *Journal of Hazardous Materials* **2010**, *180*, 634.
(135) Cheng, Z.; Zhang, L.; Guo, X.; Jiang, X.; Li, T. *Spectrochimica Acta Part A: Molecular and Biomolecular Spectroscopy* **2015**, *137*, 1126.
(136) Zhang, Z.; Moghaddam, L.; O'Hara, I. M.; Doherty, W. O. S. *Chemical Engineering Journal* **2011**, *178*, 122.
(137) Maffini, M. V.; Rubin, B. S.; Sonnenschein, C.; Soto, A. M. *Molecular and Cellular Endocrinology* **2006**, *254-255*, 179.
(138) Brody Julia, G.; Rudel Ruthann, A. *Environmental Health Perspectives* **2003**, *111*, 1007.
(139) Mileva, G.; Baker, L. S.; Konkle, T. A.; Bielajew, C. *International Journal of Environmental Research and Public Health* **2014**, *11*.
(140) Seachrist, D. D.; Bonk, K. W.; Ho, S.-M.; Prins, G. S.; Soto, A. M.; Keri, R. A. *Reproductive Toxicology* **2016**, *59*, 167.
(141) Nomiri, S.; Hoshyar, R.; Ambrosino, C.; Tyler, C. R.; Mansouri, B. *Environmental Science and Pollution Research* **2019**, *26*, 8459.
(142) Kaneti, Y. V.; Dutta, S.; Hossain, M. S. A.; Shiddiky, M. J. A.; Tung, K.-L.; Shieh, F.-K.; Tsung, C.-K.; Wu, K. C. W.; Yamauchi, Y. *Advanced Materials* **2017**, *29*, 1700213.
(143) Khan, J. H.; Lin, J.; Young, C.; Matsagar, B. M.; Wu, K. C. W.; Dhepe, P. L.; Islam, M. T.; Rahman, M. M.; Shrestha, L. K.; Alshehri, S. M.; Ahamad, T.; Salunkhe, R. R.; Kumar, N. A.; Martin, D. J.; Yamauchi, Y.; Hossain, M. S. A. *Materials Chemistry and Physics* **2018**, *216*, 491.
(144) Van Nguyen, C.; Lee, S.; Chung, Y. G.; Chiang, W.-H.; Wu, K. C. W. *Applied Catalysis B: Environmental* **2019**, *257*, 117888.
(145) Wang, J.; Luo, X.; Young, C.; Kim, J.; Kaneti, Y. V.; You, J.; Kang, Y.-M.; Yamauchi, Y.; Wu, K. C. W. *Chemistry of Materials* **2018**, *30*, 4401.
(146) Wang, C.; O'Connell, M. J.; Chan, C. K. *ACS Applied Materials & Interfaces* **2015**, *7*, 8952.
(147) Ho, Y.-S. *Polish Journal of Environmental Studies* **2006**, *15*, 81.
(148) Kinniburgh, D. G. *Environmental Science & Technology* **1986**, *20*, 895.
(149) Chen, X. *Modeling of Experimental Adsorption Isotherm Data*, 2015; Vol. 6.
(150) Freundlich, H. M. F. *J. Phys. Chem.* **1906**, *57*, 385.
(151) Lagergren, S. *Kungliga Svenska Vetenskapsakademiens Handlingar* **1898**, *24*, 1.
(152) Blanchard, G.; Maunaye, M.; Martin, G. *Water Research* **1984**, *18*, 1501.

(153) Plazinski, W.; Rudzinski, W.; Plazinska, A. *Advances in Colloid and Interface Science* **2009**, *152*, 2.
(154) Qiu, H.; Lv, L.; Pan, B.-c.; Zhang, Q.-j.; Zhang, W.-m.; Zhang, Q.-x. *Journal of Zhejiang University-SCIENCE A* **2009**, *10*, 716.
(155) Weber, W. J.; Morris, J. C. *American Water Works Association* **1964**, *56*, 447.
(156) Bindumadhavan, K.; Srivastava, S.; Srivastava, I. *Green Synthesis of Graphene*, 2013; Vol. 13.
(157) Chen, X. Y.; Chen, C.; Zhang, Z. J.; Xie, D. H. *Journal of Materials Chemistry A* **2013**, *1*, 10903.
(158) Fey, G. T.-K.; Lee, D. C.; Lin, Y. Y.; Kumar, T. P. *Synthetic Metals* **2003**, *139*, 71.
(159) Paine, J. B.; Pithawalla, Y. B.; Naworal, J. D. *Journal of Analytical and Applied Pyrolysis* **2008**, *83*, 37.
(160) Carlson, T. R.; Jae, J.; Huber, G. W. *ChemCatChem* **2009**, *1*, 107.
(161) Patwardhan, P. R.; Satrio, J. A.; Brown, R. C.; Shanks, B. H. *Journal of Analytical and Applied Pyrolysis* **2009**, *86*, 323.
(162) Angın, D. *Bioresource Technology* **2013**, *128*, 593.
(163) Lua, A. C.; Yang, T.; Guo, J. *Journal of Analytical and Applied Pyrolysis* **2004**, *72*, 279.
(164) Fu, P.; Hu, S.; Xiang, J.; Sun, L.; Su, S.; Wang, J. *Journal of Analytical and Applied Pyrolysis* **2012**, *98*, 177.
(165) Han, S.-W.; Jung, D.-W.; Jeong, J.-H.; Oh, E.-S. *Chemical Engineering Journal* **2014**, *254*, 597.
(166) Bukallah, S. B.; Rauf, M. A.; AlAli, S. S. *Dyes and Pigments* **2007**, *74*, 85.
(167) Spagnoli, A. A.; Giannakoudakis, D. A.; Bashkova, S. *Journal of Molecular Liquids* **2017**, *229*, 465.
(168) Islam, M. A.; Benhouria, A.; Asif, M.; Hameed, B. H. *Journal of the Taiwan Institute of Chemical Engineers* **2015**, *52*, 57.
(169) Islam, M. A.; Ahmed, M. J.; Khanday, W. A.; Asif, M.; Hameed, B. H. *Journal of Environmental Management* **2017**, *203*, 237.
(170) Ahmed, M. J.; Okoye, P. U.; Hummadi, E. H.; Hameed, B. H. *Bioresource Technology* **2019**, *278*, 159.
(171) Yang, S.; Gao, M.; Luo, Z. *Chemical Engineering Journal* **2014**, *256*, 39.
(172) Li, Y.; Meas, A.; Shan, S.; Yang, R.; Gai, X.; Wang, H.; Tsend, N. *Bioresource Technology* **2018**, *261*, 257.
(173) Li, Y.; Meas, A.; Shan, S.; Yang, R.; Gai, X. *Bioresource Technology* **2016**, *207*, 379.
(174) Zhao, G.; Li, J.; Wang, X. *Chemical Engineering Journal* **2011**, *173*, 185.
(175) Acosta, R.; Nabarlatz, D.; Sánchez-Sánchez, A.; Jagiello, J.; Gadonneix, P.; Celzard, A.; Fierro, V. *Journal of Environmental Chemical Engineering* **2018**, *6*, 823.
(176) Li, X.; Yuan, H.; Quan, X.; Chen, S.; You, S. *Journal of Environmental Sciences* **2018**, *63*, 250.
(177) Choi, Y.-K.; Kan, E. *Chemosphere* **2019**, *218*, 741.
(178) Zbair, M.; Bottlinger, M.; Ainassaari, K.; Ojala, S.; Stein, O.; Keiski, R. L.; Bensitel, M.; Brahmi, R. *Waste and Biomass Valorization* **2018**.
(179) Bhadra, B. N.; Lee, J. K.; Cho, C.-W.; Jhung, S. H. *Chemical Engineering Journal* **2018**, *343*, 225.
(180) Sankpal, U. T.; Pius, H.; Khan, M.; Shukoor, M. I.; Maliakal, P.; Lee, C. M.; Abdelrahim, M.; Connelly, S. F.; Basha, R. *Tumor Biology* **2012**, *33*, 1265.

(181) Zhou, Q.; Xi, S. *Regulatory Toxicology and Pharmacology* **2018**, *99*, 78.

(182) Hughes, M. F.; Beck, B. D.; Chen, Y.; Lewis, A. S.; Thomas, D. J. *Toxicological Sciences* **2011**, *123*, 305.

(183) Hubaux, R.; Becker-Santos, D. D.; Enfield, K. S.; Rowbotham, D.; Lam, S.; Lam, W. L.; Martinez, V. D. *Molecular Cancer* **2013**, *12*, 20.

(184) Meliker, J. R.; Slotnick, M. J.; AvRuskin, G. A.; Schottenfeld, D.; Jacquez, G. M.; Wilson, M. L.; Goovaerts, P.; Franzblau, A.; Nriagu, J. O. *Cancer Causes & Control* **2010**, *21*, 745.

(185) Liu, J.; Waalkes, M. P. *Toxicological Sciences* **2008**, *105*, 24.

(186) Benbrahim-Tallaa, L.; Waalkes, M. P. *Environmental Health Perspectives* **2008**, *116*, 158.

(187) *World Health Organization, WHO (2011) Guidelines for drinking-water quality*; 4th ed.

(188) Pal, P.; Chakrabortty, S.; Linnanen, L. *Science of The Total Environment* **2014**, *476-477*, 601.

(189) Shih, M.-C. *Desalination* **2005**, *172*, 85.

(190) Tresintsi, S.; Simeonidis, K.; Pliatsikas, N.; Vourlias, G.; Patsalas, P.; Mitrakas, M. *Journal of Solid State Chemistry* **2014**, *213*, 145.

(191) Mólgora, C. C.; Domínguez, A. M.; Avila, E. M.; Drogui, P.; Buelna, G. *Separation and Purification Technology* **2013**, *118*, 645.

(192) Chammui, Y.; Sooksamiti, P.; Naksata, W.; Thiansem, S.; Arqueropanyo, O.-a. *Chemical Engineering Journal* **2014**, *240*, 202.

(193) Habuda-Stanić, M.; Nujić, M. *Environmental Science and Pollution Research* **2015**, *22*, 8094.

(194) Akin, I.; Arslan, G.; Tor, A.; Ersoz, M.; Cengeloglu, Y. *Journal of Hazardous Materials* **2012**, *235-236*, 62.

(195) Luther, S.; Borgfeld, N.; Kim, J.; Parsons, J. G. *Microchemical Journal* **2012**, *101*, 30.

(196) Prasad, B.; Ghosh, C.; Chakraborty, A.; Bandyopadhyay, N.; Ray, R. K. *Desalination* **2011**, *274*, 105.

(197) Lin, S.; Lu, D.; Liu, Z. *Chemical Engineering Journal* **2012**, *211-212*, 46.

(198) Vaclavikova, M.; Gallios, G.; Stefusova, K.; Jakabsky, S.; Hredzak, S.; Springer Netherlands: Dordrecht, 2008, p 291.

(199) Yantasee, W.; Warner, C. L.; Sangvanich, T.; Addleman, R. S.; Carter, T. G.; Wiacek, R. J.; Fryxell, G. E.; Timchalk, C.; Warner, M. G. *Environmental Science & Technology* **2007**, *41*, 5114.

(200) Feng, L.; Cao, M.; Ma, X.; Zhu, Y.; Hu, C. *Journal of Hazardous Materials* **2012**, *217-218*, 439.

(201) Zboril, R.; Mashlan, M.; Petridis, D. *Chemistry of Materials* **2002**, *14*, 969.

(202) Deshpande, K.; Mukasyan, A.; Varma, A. *Chemistry of Materials* **2004**, *16*, 4896.

(203) Juliet, O.; Hassan, K.; Azizollah, N. *Materials Science-Poland* **2016**, *34*, 655.

(204) Vargas, M. A.; Diosa, J. E.; Mosquera, E. *Data in Brief* **2019**, *25*, 104183.

(205) Faraji, M.; Shabanian, M.; Aryanasab, F. *Journal of the Iranian Chemical Society* **2018**, *15*, 733.

(206) Mishra, D.; Arora, R.; Lahiri, S.; Amritphale, S. S.; Chandra, N. *Protection of Metals and Physical Chemistry of Surfaces* **2014**, *50*, 628.

(207) Zhang, C.; Sui, J.; Li, J.; Tang, Y.; Cai, W. *Chemical Engineering Journal* **2012**, *210*, 45.

(208) Alessandro, F. G.; Paolo, V. *American Mineralogist* **1999**, *84*, 895.

(209) (ATSDR), A. f. T. S. a. D. R.; U.S. Department of Health and Human Services, P. H. S., Ed. Atlanta, GA, 2019.
(210) ATSDR; Services, U. S. D. o. H. a. H., Ed. Agency for Toxic Substances and Disease Registry, 2005.
(211) Fenton, H. J. H. *Journal of the Chemical Society, Transactions* **1894**, *65*, 899.
(212) Koppenol, W. H. *Free Radical Biology and Medicine* **1993**, *15*, 645.
(213) Xu, L.; Wang, J. *Applied Catalysis B: Environmental* **2012**, *123-124*, 117.
(214) Huang, R.; Fang, Z.; Yan, X.; Cheng, W. *Chemical Engineering Journal* **2012**, *197*, 242.
(215) Hu, X.; Liu, B.; Deng, Y.; Chen, H.; Luo, S.; Sun, C.; Yang, P.; Yang, S. *Applied Catalysis B: Environmental* **2011**, *107*, 274.
(216) Cleveland, V.; Bingham, J.-P.; Kan, E. *Separation and Purification Technology* **2014**, *133*, 388.
(217) Liao, Q.; Sun, J.; Gao, L. *Colloids and Surfaces A: Physicochemical and Engineering Aspects* **2009**, *345*, 95.
(218) Liu, Y.; Jin, W.; Zhao, Y.; Zhang, G.; Zhang, W. *Applied Catalysis B: Environmental* **2017**, *206*, 642.
(219) Panda, N.; Sahoo, H.; Mohapatra, S. *Journal of Hazardous Materials* **2011**, *185*, 359.
(220) Deng, S.; Bai; Chen, J. P. *Langmuir* **2003**, *19*, 5058.
(221) Jin, L.; Bai, R. *Langmuir* **2002**, *18*, 9765.
(222) He, F.; Wang, W.; Moon, J.-W.; Howe, J.; Pierce, E. M.; Liang, L. *ACS Applied Materials & Interfaces* **2012**, *4*, 4373.
(223) Xia, Z.; Baird, L.; Zimmerman, N.; Yeager, M. *Applied Surface Science* **2017**, *416*, 565.
(224) Li, G.; Zhao, Z.; Liu, J.; Jiang, G. *Journal of Hazardous Materials* **2011**, *192*, 277.
(225) Hao, J.; Han, M.-J.; Meng, X. *Journal of Hazardous Materials* **2009**, *167*, 1215.
(226) Li, Y.; Wang, G.; Wei, T.; Fan, Z.; Yan, P. *Nano Energy* **2016**, *19*, 165.
(227) Qin, H.; Xiao, R.; Guo, L.; Meng, J.; Chen, J. *Water Science and Technology* **2018**, *2017*, 310.
(228) Xia, J.; Jiang, K.; Xie, J.; Guo, S.; Liu, L.; Zhang, Y.; Nie, S.; Yuan, Y.; Yan, H.; Wang, X. *Chemical Engineering Journal* **2019**, *359*, 1244.
(229) Jiang, F.; Ge, Z.; Niu, B.; Yuan, M.; Wei, S.; Li, M. *Journal of Applied Polymer Science* **2019**, *136*, 47816.
(230) Qiu, W.; Zhao, J.; Song, X.; Mao, Q.; Ren, S.; Hao, C.; Xiao, Y. *Industrial & Engineering Chemistry Research* **2020**, *59*, 226.
(231) Chen, M.; Le, T.; Zhou, Y.; Kang, F.; Yang, Y. *ACS Applied Energy Materials* **2020**, *3*, 1653.
(232) Kaveeshwar, A. R.; Kumar, P. S.; Revellame, E. D.; Gang, D. D.; Zappi, M. E.; Subramaniam, R. *Journal of Cleaner Production* **2018**, *193*, 1.
(233) Kravchenko, J.; Darrah, T. H.; Miller, R. K.; Lyerly, H. K.; Vengosh, A. *Environmental Geochemistry and Health* **2014**, *36*, 797.

Vita

Luis Alfonso Barrera earned his B.S. in Chemistry and B.S. in Biology from the University of Texas at El Paso in 2011. While there he was selected as part of the Louis Stokes Alliance for Minority Participation Program, where he spent a summer working under the guidance of Dr. Katja Michael. This experience led to him joining her research team in 2012, which culminated in a M.S. degree in Chemistry with an emphasis in carbohydrate and peptide chemistry. He was awarded the Research Initiative for Scientific Enhancement scholarship from 2012 to 2014.

Wanting to pursue a doctoral degree, Luis joined the laboratory of Dr. Juan Noveron in 2016, where he focused his research in the development of novel adsorbents for water remediation. He mentored three high school teachers as part of the NEWT Research Experience for Teachers program, where he undertook ambitious projects geared towards water remediation. He successfully authored two peer-reviewed papers and collaborated on two other projects which culminated in publications. In 2016 he interned at the United States Department of Agriculture-Agricultural Research Services in Maryland, where he worked under the supervision of Dr. Devanand Luthria on the extraction and analysis of primary and secondary metabolites in cacao and tomato plants. During his time at UTEP, Luis also had the privilege of teaching hundreds of undergraduate students as a teaching assistant for organic chemistry, with many of his students going on to pursue their own research opportunities.

Contact Information: labarrera@miners.utep.edu